Spring 2015

Maneuver analysis for spinning thrusting spacecraft and spinning tethered spacecraft

Kaela Mae Martin
Purdue University

PURDUE UNIVERSITY
GRADUATE SCHOOL
Thesis/Dissertation Acceptance

This is to certify that the thesis/dissertation prepared

By Kaela M. Martin

Entitled
MANEUVER ANALYSIS FOR SPINNING THRUSTING SPACECRAFT AND SPINNING
TETHERED SPACECRAFT

For the degree of   Doctor of Philosophy

Is approved by the final examining committee:

James M. Longuski

Kathleen C. Howell

Mohammad A. Ayoubi

M. Corless

To the best of my knowledge and as understood by the student in the Thesis/Dissertation Agreement, Publication Delay, and Certification/Disclaimer (Graduate School Form 32), this thesis/dissertation adheres to the provisions of Purdue University's "Policy on Integrity in Research" and the use of copyrighted material.

James M. Longuski

Approved by Major Professor(s): _____

Approved by: W. Chen   04/21/2015

Head of the Department Graduate Program   Date

MANEUVER ANALYSIS FOR SPINNING THRUSTING SPACECRAFT

AND SPINNING TETHERED SPACECRAFT

A Dissertation

Submitted to the Faculty

of

Purdue University

by

Kaela M. Martin

In Partial Fulfillment of the

Requirements for the Degree

of

Doctor of Philosophy

May 2015

Purdue University

West Lafayette, Indiana

To Matt, who kept me on track.

To Raeleen, who believed in me.

To Dad, who gave me my first star map.

To Mom, who took me to the library.

ACKNOWLEDGMENTS

I would like to thank my advisor, Professor James Longuski, for his guidance and support during my time at Purdue. I am also grateful to Professors Mohammad Ayoubi, Martin Corless, and Kathleen Howell for being members of my Ph.D. committee.

This research is supported by the National Science Foundation Graduate Research Fellowship under grant number DGE-1333468 and by a Purdue Doctoral Fellowship. I'm very grateful for the freedom and opportunities that these fellowships gave me to finish my degree.

A special thanks to my recommendation letter writers, Professor James Longuski, Professor Kathleen Howell, Professor Dale Chimenti, Professor Heidi Diefus-Dux, and Dr. Jennifer Groh. My many interview opportunities would not be possible without your help.

In addition, I would like to thank Professors Weinong Chen and Tom Shih for giving me the opportunity to teach a summer class which provided me valuable experience for my future career.

I'm grateful for the opportunities to collaborate with Professor Mohammad Ayoubi and Dr. Damon Landau. This thesis would not be possible without you.

Thank you to my fellow research group members, Frank Laipert, Kyle Hughes, Peter Edelman, Nathan Strange, and Sarag Saikia, for your time editing papers and presentations and for your advice.

This work would not be finished (at least in a timely matter) if not for the support of my husband, Matt. Thank you for staying in Indiana with me.

Finally, I would like to thank my family (Marilyn, Pete, Raeleen, Rob, Laura, Dave, and Dan) and friends for their advice and encouragement.

TABLE OF CONTENTS

LIST OF TABLES

LIST OF FIGURES

NOMENCLATURE

$\mathbf{a}$	acceleration vector, m/s^2
c_1, c_2, c_3	constant thrust profile coefficients
d	thrust offset distance from center of mass, m
d_X, d_Y, d_Z	inertial distances, m
F	thruster force profile, N
F_{max}	maximum thrust, N
f_x, f_y, f_z	components of body-fixed forces, N
$\mathbf{H}$	inertial angular momentum, kg·m^2/s
g	standard acceleration due to gravity, m/s^2
h	distance from nozzle throat to center of mass, m
I_{sp}	specific impulse of thruster, s
I_x, I_y, I_x	principal moments of inertia, kg·m^2
L	tether length, m
M	torque, N·m
m	spacecraft mass, kg
$\dot{m}$	propellant flow rate, kg/s
$^I\mathbf{R}^R_{312}$	rotation matrix relating the R-frame to I-frame using 3-1-2 Euler angle sequence
R	reaction force, N
T	thrust, N
$\mathbf{T}$	thrust vector, N
$\mathbf{T}_\alpha$	thrust vector rolled along $\hat{\mathbf{r}}$, N
t_b	burn time, s
t_r	ramp time, s
t_{rlin}	linear ramp-up time, s

$\mathbf{v}$	velocity vector, m/s
V_X, V_Y, V_Z	inertial velocities, m/s
α	thrust misalignment angle, rad
β	initial percent of F_{max}
γ	spacecraft orientation angle around $\hat{\mathbf{z}}$, rad
$\dot{\gamma}$	spin-rate about $\hat{\mathbf{z}}$, rad/s, rpm
ΔV	scalar transfer maneuver change in velocity, m/s
η	spacecraft roll angle about positive $\hat{\mathbf{r}}$, rad
θ	spacecraft orientation angle around $\hat{\boldsymbol{\theta}}$, rad
$\dot{\theta}$	spin-rate about $\hat{\boldsymbol{\theta}}$, rad/s
μ	engine inert-to-propellant mass ratio
ρ	velocity pointing error, rad
ρ_{max}	maximum ending velocity pointing error, rad
ρ_X, ρ_Y	velocity pointing angles, rad
ϕ_x, ϕ_y, ϕ_z	Euler angles, rad
ψ	thrust offset from the tether, rad
$\dot{\phi}$	spin-rate about $\hat{\boldsymbol{\phi}}$, rad/s
ω	angular velocity, rad/s
$\mathfrak{J}$	total impulse, N·s

Subscripts

0	initial condition
1	ramp-up burn
2	controlled burn
3	ramp-down burn
AG	artificial gravity
avg	average
C	coupled thruster
cm	center of mass

h	crew habitat
J	include jet damping
NJ	excludes jet damping
p	propulsion system
$prop$	propellant
S	single thruster
X, Y, Z	coordinate axes used in inertial I-frame
X_R, Y_R, Z_R	intermediate coordinate axes used in inertial R-frame rotated from I-frame
x, y, z	body-fixed coordinate axes used in B-frame and aligned with principal axes
r, θ, ϕ	body-fixed coordinate axes for tethered spacecraft

ABSTRACT

Martin, Kaela M. PhD, Purdue University, May 2015. Maneuver Analysis for Spinning Thrusting Spacecraft and Spinning Tethered Spacecraft.   Major Professor: James M. Longuski.

During axial thrusting of a spin-stabilized spacecraft undergoing orbital injections or control maneuvers, misalignments and center-of-mass offset create undesired body-fixed torques. The effects of the body-fixed torques, which in turn cause velocity pointing errors, can be reduced by ramping up (and then ramping down) the thruster. The first topic discussed in this thesis derives closed-form solutions for the angular velocity, Euler angles, inertial velocity, and inertial displacement solutions with nonzero initial conditions. Using the closed-form solutions, the effect of variations in the spin-axis moment of inertia and spin-rate on the spacecraft velocity pointing error are shown. The analytical solutions closely match numerical simulations. The next topic considers various ramp-up profiles (including parabolic, cosine, logarithmic, exponential, and cubic) to heuristically find a suboptimal solution to reduce the velocity pointing error. Some of the considered cosine, logarithmic, exponential, parabolic, and cubic profiles drive the velocity pointing error to nearly zero and hence qualify as effective solutions. The third topic examines a large tethered spacecraft that produces artificial gravity with the propulsion system on one end of the tether. Instead of thrusting through the center of mass, the offset thrust occurs at an angle to the tether which is held in the desired direction by changing the spin rate to compensate for decreasing propellant mass. The dynamics and control laws of the system are derived for constant, time-varying, planar, and non-planar thrust as well as spin-up maneuvers. The final topic discusses how the Bödewadt solution of a self-excited rigid body is unable to accurately predict the motion compared to a numerical integration of the equations of motion.

1. Introduction

1.1 Motivation

The motion of spacecraft subjected to body-fixed forces and torques was reported by Leimanis in 1965 in his classic treatise, *The General Problem of the Motion of Coupled Rigid Bodies about a Fixed Point* [1]. This seminal work provides a foundation for aerospace engineers concerned with the motion of spacecraft subject to body-fixed forces and torques. In many cases, spacecraft can be treated as spinning symmetric or nearly-symmetric rigid bodies.

1.1.1 Spinning Thrusting Spacecraft Maneuvers

During axial thrusting of a spinning spacecraft, thrust misalignment and center-of-mass offset create transverse body-fixed torques which perturb the angular momentum vector from its desired inertial direction. The bias in the angular momentum vector directly results in velocity pointing errors which cause the spacecraft to deviate from its desired trajectory, requiring more propellant for the spacecraft to achieve its mission.

Since 1965, much work has been done on a spinning rigid body including spinning vehicles with changing mass [2–6], dual-spin spacecraft [7–13], and asymmetric [14,15] and nearly axisymmetric [16–18] spacecraft. In many cases, spacecraft can be treated as spinning symmetric or nearly-symmetric rigid bodies, and during axial thrusting, misalignments and center-of-mass offset result in velocity pointing errors which cause the spacecraft to deviate from its desired trajectory.

Analytical solutions for the spinning spacecraft have been found for the angular velocity, attitude, and inertial velocity using various perturbation methods [15, 16, 19,

20]. For more specific cases, non-perturbation methods are used to find analytical results such as dual-spin spacecraft [10] and near-symmetric spinning rigid bodies with a thruster that has constant torque [21–23] and time-varying torque [24, 25] as well as bodies that are asymmetric [26]. The stability analysis for an asymmetric spinning rigid body with a constant torque has also been analyzed [14] as well as for dual-spin spacecraft [9]. Analytical solutions have also been found for spinning-up maneuvers [27–31]. The inertial velocity and displacement solutions for constant torque [32] and linear torque [33] are also known.

Historically, the velocity pointing error has been reduced by spinning at a high rate [34]. One method to reduce the pointing error is to use a two-burn scheme where the burn is momentarily suspended and then restarted to reduce the pointing error [35, 36]. It has also been shown that if the axial thrust is a linear function of time beginning at zero and ramping up to maximum thrust, the velocity pointing error could be significantly decreased with respect to the usual case where the thrust can be modeled as a step function since the average angular momentum vector for the linear ramp now remains pointing in the desired direction [37]. Extending work by Javorsek and Longuski [37], analytical expressions for the inertial velocity with linear torques and nonzero initial conditions are derived which in turn are used to predict the velocity pointing error.

While a linear thrust profile can reduce velocity pointing errors, it is unclear what is the best scheme to ramp-up the thruster to minimize pointing error. Finding the optimal solution for the thrust history (i.e. the control) to minimize the velocity pointing error is difficult to solve using indirect methods since the solution involves nine nonlinear differential equations and the ending velocity pointing error tends to oscillate at a high frequency typically 1 rev/s with respect to the ramp-up time. Instead, a heuristic approach is taken to find suboptimal ramp-up profiles.

1.1.2 Spinning Tethered Spacecraft Maneuvers

It is well known that artificial gravity may be needed for long-duration interplanetary missions to prevent bone and muscle loss [38–41]. Hours of daily exercise is not enough to counteract these losses [42, 43]. A short-arm centrifuge could be included in the cabin crew instead of rotating the entire vehicle [44–46], but unless very high spin rates are used (causing motion sickness), it is unlikely that this centrifuge would improve bone structural integrity [42,47,48]. Furthermore since the entire crew cabin would not have artificial gravity, the habitat design is unable to exploit gravity benefits, and the centrifuge would require additional spacecraft mass. Other design approaches to produce gravity include a small tether attached to the spacecraft, but these short tethers can only produce small levels of gravity (on the order of 10^{-2} g) [49–51].

A large toroidal spacecraft such as the one in Stanley Kubrick's *2001: A Space Odyssey* could produce enough artificial gravity, but the required radius of the toroidal to produce artificial gravity at a reasonable spin rate is very large resulting in an unreasonable launch mass. To reduce mass, a tethered spacecraft can be used where the human habitation module is connected by a tether to the propellant tanks or alternatively the habitation module and the thrusters are connected by a tether to a counterweight (empty third stage, nuclear power plant, fouod supplies, etc.). The relatively low-mass tether is the only additional required mass for artificial gravity. Compared to other current technologies, these tether-based missions are "attractive" for Mars missions [52]. For a comprehensive review of space tethers, see Cartmell and McKenzie [53], Misra and Modi [54], and Cosmo and Lorenzini [55].

For a tethered spacecraft to thrust through the center of mass, the spacecraft can either spin down and reel in the tether during maneuvers or adjust the tether length to burn through the changing center of mass [41, 56–59]. The first scenario requires additional mass to despin the spacecraft (and lose artificial gravity), and the second scenario requires a more complex spacecraft.

The spacecraft could have artificial gravity for the entire mission with a fixed tether configuration if the thrust is on one end of the tether similar to the Galileo spacecraft which had control thrusters on two booms two meters away from the main spacecraft [60]. The thrusters on Galileo could be used in either continuous or pulsed mode [13], and performed maneuvers include spacecraft turns [60, 61], ΔV maneuvers [60], and spin-change maneuvers [35, 62, 63]. With inspiration from the Galileo spacecraft, the tethered spacecraft with artificial gravity will consider ΔV and spin-change maneuvers. During maneuvers, the spacecraft orientation is fixed relative to the spin axis by adjusting the thrust level or slightly rolling the thrust along the tether axis, allowing the entire burn to be in the desired direction.

Although artificial gravity is considered to be an important capability to serve human missions to Mars, no papers known to the author have appeared in the literature that address how maneuvers will be performed on a spinning tethered human spacecraft.

1.2 Overview

The four topics of this thesis are contained in the next four chapters. Chapter 2 covers an analytical solution for the inertial velocity and displacements of a spacecraft with a linear ramp-up thrust profile with non-zero initial conditions. Chapter 3 discusses other heuristic thrust profiles which reduce the velocity pointing error even further. Some of these profiles (exponential, logarithmic, parabolic, cubic, and cosine) can be considered effective solutions. Chapter 4 examines the dynamics of a tethered spacecraft which can produce artificial gravity by spinning and thrusting at an angle to the tether. This chapter is an expansion of work done by Landau [64]. Chapter 5 briefly examines the effectiveness of the Bödewadt solution for self-excited rigid bodies. The final chapter summarizes the conclusions and suggests opportunities for future work.

2. Analytical Solution for Spinning Thrusting Spacecraft with Transverse Ramp-Up Torques

2.1 Background

A misaligned and constant thruster can cause unwanted body-fixed constant torques forcing the spacecraft to deviate from its desired direction consequently requiring more propellant for the spacecraft to achieve its mission. Analytical results for the attitude have been found for near-symmetric spinning rigid bodies with a thruster that has constant torque [21–23] and time-varying torque [22, 24, 25] as well as bodies that are asymmetric [26]. The inertial velocity and displacement solutions for constant torque are known [32] but have only recently been reported for time-varying torque by Ayoubi, Martin, and Longuski [33].

Analytical solutions give insight into the behavior of the motion by providing explicit expressions for periodic motion, secular effects, and asymptotic limits. Identifying periodic and secular terms or determining the asymptotic limits arising from a complete but complicated analytical theory can lead to simple closed-form practical solutions. Moreover, the geometrically limiting cases such as a sphere, a thin rod, and a flat disk usually reduce significantly the number of terms in the full-blown theory. Such simplified expressions can give the practical engineer a way to understand the essential motion–a back-of-the envelope calculation.

In an axial-thrusting spacecraft maneuver, the velocity pointing error has historically been reduced by spinning at a high rate [34]. One method to reduce the pointing error is by gradually ramping up the axial thrust from zero to its maximum value [37]. While Javorsek and Longuski [37] discuss some analytical results, they did not derive the analytical expressions for the inertial velocity with linear torques and nonzero initial conditions.

This chapter extends previous works [14, 24, 25] in finding closed-form solutions for rotational and translational motion of a spinning spacecraft during thrusting maneuver and when the spacecraft is subjected to ramp-up(down) body-fixed forces and moments. Moreover, it extends the work by Javorsek and Longuski [37] for predicting the velocity pointing error of a thrusting, spinning spacecraft with constant mass properties and ramp-up(down) forcing condition. The angular velocity solution for this case can be found in Ayoubi, Landau, and Longuski [65], but the remaining solutions are presented here as well as in Ayoubi, Martin, and Longuski [33].

2.2   Governing Equations

Consider a spinning rigid body with constant mass properties as depicted in Fig. 2.1. The spacecraft has undesired transverse torques of M_x and M_y, no axial torque, a thruster offset of d, and a thruster misalignment of α. Assume the body-fixed reference frame, B, has its origin located at the center of mass and aligned with the principal axes of the rigid body. Capital letters signify the vector in the inertial reference frames, I and R, and lower case letters signify vectors in the body-fixed frame, B. The inertial R-frame is an intermediate inertial frame that is rotated from the inertial I-frame by a set of initial Euler angles. The rotated frame simplifies the velocity and displacement solutions when using a nonzero set of initial Euler angles.

It should be noted that the velocities and displacements in this chapter are the changes in velocity and displacement and are normally preceded by a Δ. However, for more efficient notation, the Δ is left out.

The angular velocity of a spacecraft is described by Euler's equations of motion [66] and can be written as

$$
\begin{aligned}
\dot{\omega}_x(t) &= M_x/I_x - \left[(I_z - I_y)/I_x\right]\omega_y\omega_z \\
\dot{\omega}_y(t) &= M_y/I_y - \left[(I_x - I_z)/I_y\right]\omega_z\omega_x \\
\dot{\omega}_z(t) &= - \left[(I_y - I_x)/I_z\right]\omega_x\omega_y
\end{aligned}
\tag{2.1}
$$
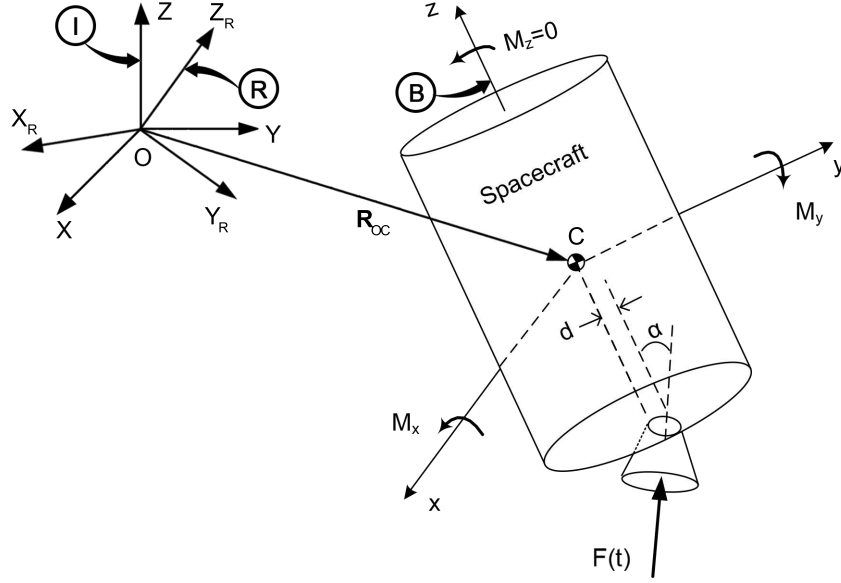
Figure 2.1. Model for thrusting, spinning spacecraft.

where it is assumed that there is no axial torque (i.e. $M_z = 0$) and that I_z is either the minimum or maximum moment of inertia (i.e. the spacecraft is spinning about a stable axis). Since the engine ramp-up time is presumed to be short compared to the entire burn, the principal moments of inertia are assumed to be constant.

It can be shown that for an axisymmetric, nearly-axisymmetric, and for an asymmetric rigid body when $[(I_y - I_x)/I_z]\omega_x\omega_y$ is small, Euler's equations of motion can be written as

$$\dot{\omega}_x(t) = M_x/I_x - [(I_z - I_y)/I_x]\,\omega_y\omega_z \tag{2.2}$$

$$\dot{\omega}_y(t) = M_y/I_y - [(I_x - I_z)/I_y]\,\omega_z\omega_x \tag{2.3}$$

$$\dot{\omega}_z(t) \approx 0 \tag{2.4}$$

As a practical example, in the case of the Galileo spacecraft, the assumption that the spin rate was constant during axial thrusting was reasonable for Galileo's maneuver analysis even though I_x was not equal to I_y (i.e. the spacecraft was nearly axisymmetric) [60].

The kinematic equations describe the orientation of a rigid body with respect to the inertial reference frame. For this analysis, a Type-I, Euler sequence 3-1-2 (ϕ_z, ϕ_x, ϕ_y) given by Wertz [67] is used.

$$\dot{\phi}_x = \omega_x \cos \phi_y + \omega_z \sin \phi_y \qquad (2.5)$$

$$\dot{\phi}_y = \omega_y - (\omega_z \cos \phi_y - \omega_x \sin \phi_y) \tan \phi_x \qquad (2.6)$$

$$\dot{\phi}_z = (\omega_z \cos \phi_y - \omega_x \sin \phi_y) \sec \phi_x \qquad (2.7)$$

For spin-stabilized spacecraft, assume that ϕ_x, ϕ_y, and the product $\phi_y \omega_x$ are small. Thus, the kinematic equations can be simplified as

$$\dot{\phi}_x = \omega_x + \phi_y \omega_z \qquad (2.8)$$

$$\dot{\phi}_y = \omega_y - \phi_x \omega_z \qquad (2.9)$$

$$\dot{\phi}_z = \omega_z \qquad (2.10)$$

When integrating Eqs. (2.8)–(2.10), initial Euler anglers appear as integration constants. By using the intermediate R-frame (essentially setting these constants to zero), lengthier velocity and displacement solutions are avoided. The R-frame is always chosen such that it is initially coincident with the B-frame (i.e. having zero initial Euler angles). Say the spacecraft is undergoing a ramp-up and a ramp-down maneuver. If the I-frame is chosen to be initially coincident with the B-frame, there are no initial Euler angles for the ramp-up maneuver. However for the ramp-down maneuver, the B-frame is no longer coincident with the I-frame. To simplify the analytical equations, a new R-frame is described which is coincident with the B-frame at the beginning of the ramp-down maneuver. Thus the initial Euler angles for the ramp-down maneuver describe how the I-frame is rotated initially with respect to the B-frame or, equivalently, how the I-frame is rotated with respect to the R-frame.

By assuming that the initial velocity constants, V_{X0}, V_{Y0}, and V_{Z0}, and the initial displacement constants, d_{X0}, d_{Y0}, and d_{Z0}, are in the I-frame, the velocity and displacement solutions in the I-frame are

$$
\begin{Bmatrix} V_X \\ V_Y \\ V_Z \end{Bmatrix} = {}^{I}\mathbf{R}_{312}^{R} \begin{Bmatrix} V_{XR} \\ V_{YR} \\ V_{ZR} \end{Bmatrix} + \begin{Bmatrix} V_{X0} \\ V_{Y0} \\ V_{Z0} \end{Bmatrix}
\tag{2.11}
$$

$$
\begin{Bmatrix} d_X \\ d_Y \\ d_Z \end{Bmatrix} = {}^{I}\mathbf{R}_{312}^{R} \begin{Bmatrix} d_{XR} \\ d_{YR} \\ d_{ZR} \end{Bmatrix} + \begin{Bmatrix} V_{X0} \\ V_{Y0} \\ V_{Z0} \end{Bmatrix} t + \begin{Bmatrix} d_{X0} \\ d_{Y0} \\ d_{Z0} \end{Bmatrix}
\tag{2.12}
$$

where the Type-I (3-1-2) direction cosine matrix [67], ${}^{I}\mathbf{R}_{312}^{R}$, is

$$
{}^{I}\mathbf{R}_{312}^{R} = \begin{bmatrix} c\phi_{y0}c\phi_{z0} - s\phi_{x0}s\phi_{y0}s\phi_{z0} & -c\phi_{x0}s\phi_{z0} & s\phi_{y0}c\phi_{z0} + s\phi_{x0}c\phi_{y0}s\phi_{z0} \\ c\phi_{y0}s\phi_{z0} + s\phi_{x0}s\phi_{y0}c\phi_{z0} & c\phi_{x0}c\phi_{z0} & s\phi_{y0}s\phi_{z0} - s\phi_{x0}c\phi_{y0}c\phi_{z0} \\ -c\phi_{x0}s\phi_{y0} & s\phi_{x0} & c\phi_{x0}c\phi_{y0} \end{bmatrix}
\tag{2.13}
$$

where c and s are abbreviations for cosine and sine functions, respectively. With the assumption that ϕ_x and ϕ_y are small, the direction cosine matrix which has the same form as Eq. (2.13) can be simplified as

$$
{}^{R}\mathbf{R}_{312}^{B} \approx \begin{bmatrix} c\phi_z & -s\phi_z & \phi_y c\phi_z + \phi_x s\phi_z \\ s\phi_z & c\phi_z & \phi_y s\phi_z - \phi_x c\phi_z \\ -\phi_y & \phi_x & 1 \end{bmatrix}
\tag{2.14}
$$

Therfore, the R-frame velocities can be solved by integrating

$$
\begin{Bmatrix} \dot{V}_{XR} \\ \dot{V}_{YR} \\ \dot{V}_{ZR} \end{Bmatrix} = {}^{R}\mathbf{R}_{312}^{B} \begin{Bmatrix} f_x/m \\ f_y/m \\ f_z/m \end{Bmatrix}
\tag{2.15}
$$

2.3   Analytical Solution

In this section, analytical solutions are presented for the angular velocity, Euler angles, inertial velocity and displacement, and velocity pointing error solutions when

the spacecraft is subjected to ramp-up transverse forces and consequently ramp-up moments.

2.3.1 The Angular Velocity Solution

For a linear ramp-up profile, the linear forces are defined as

$$
\begin{aligned}
f_x(t) &= f_{0x} + f_{1x}t \\
f_y(t) &= f_{0y} + f_{1y}t \\
f_z(t) &= f_{0z} + f_{1z}t
\end{aligned}
\tag{2.16}
$$

The torques, which are caused by forces, are

$$
\begin{aligned}
M_x(t) &= c_{0x} + c_{1x}t \\
M_y(t) &= c_{0y} + c_{1y}t \\
M_z &= 0
\end{aligned}
\tag{2.17}
$$

where the constants in Eqs. (2.16) and (2.17) are left in general form. The specific values depend on the force profile as given in the numerical analysis, section 2.4.

Equation (2.4) can be integrated as

$$
\omega_z(t) \approx \omega_{z0}, \qquad \omega_{z0} = \omega_z(0)
\tag{2.18}
$$

Now let $\omega_x(0) = \omega_{x0}$ and $\omega_y(0) = \omega_{y0}$. Integrating the remaining angular velocity equations yields [24]

$$
\begin{aligned}
\omega_x(t) =& \frac{c_{1x}}{k^2 I_x \omega_{z0}^2} - \frac{c_{0y} + c_{1y}t}{k_y I_y \omega_{z0}} + \left(\omega_{x0} - \frac{c_{1x}}{k^2 I_x \omega_{z0}^2} + \frac{c_{0y}}{k_y I_y \omega_{z0}} \right) \cos\left(k\omega_{z0}t \right) \\
& - \left(\omega_{y0}\frac{k_x}{k} - \frac{c_{1y}}{kk_y I_y \omega_{z0}^2} - \frac{c_{0x}}{k I_x \omega_{z0}} \right) \sin\left(k\omega_{z0}t \right)
\end{aligned}
\tag{2.19}
$$

$$
\begin{aligned}
\omega_y(t) =& \frac{c_{1y}}{k^2 I_y \omega_{z0}^2} + \frac{c_{0x} + c_{1x}t}{k_x I_x \omega_{z0}} + \left(\omega_{y0} - \frac{c_{1y}}{k^2 I_y \omega_{z0}^2} - \frac{c_{0x}}{k_x I_x \omega_{z0}} \right) \cos\left(k\omega_{z0}t \right) \\
& + \left(\omega_{x0}\frac{k_y}{k} - \frac{c_{1x}}{kk_x I_x \omega_{z0}^2} + \frac{c_{0y}}{k I_y \omega_{z0}} \right) \sin\left(k\omega_{z0}t \right)
\end{aligned}
\tag{2.20}
$$

where the parameters k_x, k_y, and k_z are defined as

$$
k_x \triangleq (I_z - I_y)/I_x, \qquad k_y \triangleq (I_z - I_x)/I_y, \qquad k \triangleq \sqrt{k_x k_y}
\tag{2.21}
$$

2.3.2   The Euler Angle Solution

To solve Eqs. (2.8) and (2.9), substitute the angular velocities found in Eqs. (2.18) – (2.20).

$$\phi_x(t) = \frac{c_{0x} + c_{1x}t}{I_z\omega_{z0}^2} + \frac{I_y\omega_y(t)}{I_z\omega_{z0}} - \frac{c_{1y}}{I_z\omega_{z0}^3}$$
$$- \left(\frac{c_{1x}}{I_z\omega_{z0}^3} + \frac{c_{0y}}{I_z\omega_{z0}^2} - \frac{I_x\omega_{x0}}{I_z\omega_{z0}} - \phi_{y0}\right)\sin\left(\omega_{z0}t\right) \qquad (2.22)$$
$$+ \left(\frac{c_{1y}}{I_z\omega_{z0}^3} - \frac{c_{0x}}{I_z\omega_{z0}^2} - \frac{I_y\omega_{y0}}{I_z\omega_{z0}} + \phi_{x0}\right)\cos\left(\omega_{z0}t\right)$$

$$\phi_y(t) = \frac{c_{0y} + c_{1y}t}{I_z\omega_{z0}^2} - \frac{I_x\omega_x(t)}{I_z\omega_{z0}} + \frac{c_{1x}}{I_z\omega_{z0}^3}$$
$$- \left(\frac{c_{1x}}{I_z\omega_{z0}^3} + \frac{c_{0y}}{I_z\omega_{z0}^2} - \frac{I_x\omega_{x0}}{I_z\omega_{z0}} - \phi_{y0}\right)\cos\left(\omega_{z0}t\right) \qquad (2.23)$$
$$- \left(\frac{c_{1y}}{I_z\omega_{z0}^3} - \frac{c_{0x}}{I_z\omega_{z0}^2} - \frac{I_y\omega_{y0}}{I_z\omega_{z0}} + \phi_{x0}\right)\sin\left(\omega_{z0}t\right)$$

$$\phi_z(t) = \omega_{z0}t + \phi_{z0} \qquad (2.24)$$

Note that ϕ_{x0}, ϕ_{y0}, and ϕ_{z0} are the initial Euler angles which describe how the rotated inertial R-frame is related to the original inertial I-frame.

The secular terms of Eqs. (2.22) and (2.23) are found by substituting Eq. (2.20) into Eq. (2.22) and Eq. (2.19) into Eq. (2.23). After simplifing, the secular term in ϕ_x is $c_{1x}t/\left[\omega_{z0}^2\left(I_z - I_y\right)\right]$ and in ϕ_y is $c_{1y}t/\left[\omega_{z0}^2\left(I_z - I_x\right)\right]$.

2.3.3   The Inertial Velocity and Displacement Solution

The desired inertial velocity and displacement solutions are in the original inertial I-frame. In Eqs. (2.11) and (2.12), the I-frame solutions are found by rotating the R-frame solutions using a rotation matrix which considerably lengthens the resulting velocity and displacement solutions. Instead, the solutions are reported in the intermediate R-frame which is defined to be coincident with the body-fixed B-frame at the beginning of each maneuver.

An alternative approach to obtain the velocity equations is to substitute Eqs. (2.22) – (2.24), including the initial Euler angles, into Eq. (2.15). After integrating,

the solution will be in the I-frame not the R-frame. With the addition of the nonzero Euler angles, the solutions become longer and more complicated than velocity solutions found in the R-frame. Furthermore, the matrix in Eq. (2.15) assumes that ϕ_x and ϕ_y, which would now include the initial Euler angles, are small. In the R-frame calculation presented in section II, the rotation matrix in Eq. (2.13) does not have small angle assumptions, so the calculation in section II is more accurate than this alternative method.

Now returning to the R-frame, the velocity solutions in the R-frame found by solving Eq. (2.15) are

$$
\begin{aligned}
V_{XR} =& A_0 + A_t t + A_{tt} t^2 + \left(A_{c0} + A_{ct} t + A_{ctt} t^2 \right) \cos \omega_{z0} t \\
&+ (A_{cc} + A_{cct} t) \cos k\omega_{z0} t \cos \omega_{z0} t + (A_{cs} + A_{cst} t) \sin k\omega_{z0} t \cos \omega_{z0} t \\
&+ \left(A_{s0} + A_{st} t + A_{stt} t^2 \right) \sin \omega_{z0} t + (A_{sc} + A_{sct} t) \cos k\omega_{z0} t \sin \omega_{z0} t \\
&+ (A_{ss} + A_{sst} t) \sin k\omega_{z0} t \sin \omega_{z0} t
\end{aligned}
\tag{2.25}
$$

$$
\begin{aligned}
V_{YR} =& B_0 + B_t t + B_{tt} t^2 + \left(B_{c0} + B_{ct} t + B_{ctt} t^2 \right) \cos \omega_{z0} t \\
&+ (B_{cc} + B_{cct} t) \cos k\omega_{z0} t \cos \omega_{z0} t + (B_{cs} + B_{cst} t) \sin k\omega_{z0} t \cos \omega_{z0} t \\
&+ \left(B_{s0} + B_{st} t + B_{stt} t^2 \right) \sin \omega_{z0} t + (B_{sc} + B_{sct} t) \cos k\omega_{z0} t \sin \omega_{z0} t \\
&+ (B_{ss} + B_{sst} t) \sin k\omega_{z0} t \sin \omega_{z0} t
\end{aligned}
\tag{2.26}
$$

$$
\begin{aligned}
V_{ZR} =& C_0 + C_t t + C_{tt} t^2 + C_{ttt} t^3 + (C_c + C_{ct} t) \cos \omega_{z0} t \\
&+ (C_{ck} + C_{ckt} t) \cos k\omega_{z0} t + (C_s + C_{st} t) \sin \omega_{z0} t \\
&+ (C_{sk} + C_{skt} t) \sin k\omega_{z0} t
\end{aligned}
\tag{2.27}
$$

where the A, B, and C coefficients are constants that are functions of the moments of inertia, ω_{z0}, and the coefficients from the torques and forces. The A, B, and C coefficients can be found in the Appendix. The subscripts s, c, and t are abbreviations for the coefficient multiplied by sine, cosine, and time respectively. In Eqs. (2.25) and (2.26), the second s and c subscript correspond to multiplying the coefficient by an additional sine or cosine term with a frequency of $k\omega_{z0}$. In Eq. (2.27), the subscript k represents that the frequency of the sinusoidal multiplier is $k\omega_{z0}$. In particular, take

note of the secular terms (which are annotated with t subscripts) as these terms grow without bound in time.

Simply integrating the inertial velocity solution in Eqs. (2.25) – (2.27) yields the R-frame displacement found in Eq. (2.12). The constant coefficients are the same for both the displacement and velocity solutions.

$$
\begin{aligned}
d_{XR} =&A_0 t + \frac{A_t t^2}{2} + \frac{A_{tt} t^3}{3} + \frac{A_{cs} k - A_{sc}}{(k^2 - 1)\,\omega_{z0}} \\
&- \frac{2A_{stt} + A_{ct}\omega_{z0} - A_{s0}\omega_{z0}^2}{\omega_{z0}^3} - \frac{A_{cct}\,(k^2 + 1) + 2A_{sst} k}{(k^2 - 1)^2\,\omega_{z0}^2} \\
&+ \left(-\frac{A_{stt} t^2 + A_{st} t + A_{s0}}{\omega_{z0}} + \frac{2A_{ctt} t + A_{ct}}{\omega_{z0}^2} + \frac{2A_{stt}}{\omega_{z0}^3} \right) \cos\omega_{z0} t \\
&+ \frac{A_{sc} + A_{sct} t - A_{cs} k - A_{cst} k t}{(k^2 - 1)\,\omega_{z0}} \cos k\omega_{z0} t \cos\omega_{z0} t \\
&+ \frac{A_{cct}\,(k^2 + 1) + 2A_{sst} k}{(k^2 - 1)^2\,\omega_{z0}^2} \cos k\omega_{z0} t \cos\omega_{z0} t \\
&+ \frac{A_{ss} + A_{sst} t + A_{cc} k + A_{cct} k t}{(k^2 - 1)\,\omega_{z0}} \sin k\omega_{z0} t \cos\omega_{z0} t \\
&+ \frac{A_{cst}\,(k^2 + 1) - 2A_{sct} k}{(k^2 - 1)^2\,\omega_{z0}^2} \sin k\omega_{z0} t \cos\omega_{z0} t \\
&+ \left(\frac{A_{ctt} t^2 + A_{ct} t + A_{c0}}{\omega_{z0}} + \frac{2A_{stt} t + A_{st}}{\omega_{z0}^2} - \frac{2A_{ctt}}{\omega_{z0}^3} \right) \sin\omega_{z0} t \\
&- \frac{A_{cc} + A_{cct} t + A_{ss} k + A_{sst} k t}{(k^2 - 1)\,\omega_{z0}} \cos k\omega_{z0} t \sin\omega_{z0} t \\
&+ \frac{A_{sct} t\,(k^2 + 1) - 2A_{cst} k}{(k^2 - 1)^2\,\omega_{z0}^2} \cos k\omega_{z0} t \sin\omega_{z0} t \\
&+ \frac{-A_{cs} - A_{cst} t + A_{sc} k + A_{sct} k t}{(k^2 - 1)\,\omega_{z0}} \sin k\omega_{z0} t \sin\omega_{z0} t \\
&+ \frac{A_{sst}\,(k^2 + 1) + 2A_{cct} k}{(k^2 - 1)^2\,\omega_{z0}^2} \sin k\omega_{z0} t \sin\omega_{z0} t
\end{aligned}
\tag{2.28}
$$

$$
\begin{aligned}
d_{YR} =& B_0 t + \frac{B_t t^2}{2} + \frac{B_{tt} t^3}{3} + \frac{B_{cs} k - B_{sc}}{(k^2 - 1)\,\omega_{z0}} \\
& - \frac{2B_{stt} + B_{ct}\omega_{z0} - B_{s0}\omega_{z0}^2}{\omega_{z0}^3} - \frac{B_{cct}\,(k^2 + 1) + 2B_{sst}k}{(k^2 - 1)^2\,\omega_{z0}^2} \\
& + \left(-\frac{B_{stt}t^2 + B_{st}t + B_{s0}}{\omega_{z0}} + \frac{2B_{ctt}t + B_{ct}}{\omega_{z0}^2} + \frac{2B_{stt}}{\omega_{z0}^3} \right) \cos\omega_{z0}t \\
& + \frac{B_{sc} + B_{sct}t - B_{cs}k - B_{cst}kt}{(k^2 - 1)\,\omega_{z0}} \cos k\omega_{z0}t \cos\omega_{z0}t \\
& + \frac{B_{cct}\,(k^2 + 1) + 2B_{sst}k}{(k^2 - 1)^2\,\omega_{z0}^2} \cos k\omega_{z0}t \cos\omega_{z0}t \\
& + \frac{B_{ss} + B_{sst}t + B_{cc}k + B_{cct}kt}{(k^2 - 1)\,\omega_{z0}} \sin k\omega_{z0}t \cos\omega_{z0}t \\
& + \frac{B_{cst}\,(k^2 + 1) - 2B_{sct}k}{(k^2 - 1)^2\,\omega_{z0}^2} \sin k\omega_{z0}t \cos\omega_{z0}t \\
& + \left(\frac{B_{ctt}t^2 + B_{ct}t + B_{c0}}{\omega_{z0}} + \frac{2B_{stt}t + B_{st}}{\omega_{z0}^2} - \frac{2B_{ctt}}{\omega_{z0}^3} \right) \sin\omega_{z0}t \\
& - \frac{B_{cc} + B_{cct}t + B_{ss}k + B_{sst}kt}{(k^2 - 1)\,\omega_{z0}} \cos k\omega_{z0}t \sin\omega_{z0}t \\
& + \frac{B_{sct}t\,(k^2 + 1) - 2B_{cst}k}{(k^2 - 1)^2\,\omega_{z0}^2} \cos k\omega_{z0}t \sin\omega_{z0}t \\
& + \frac{-B_{cs} - B_{cst}t + B_{sc}k + B_{sct}kt}{(k^2 - 1)\,\omega_{z0}} \sin k\omega_{z0}t \sin\omega_{z0}t \\
& + \frac{B_{sst}\,(k^2 + 1) + 2B_{cct}k}{(k^2 - 1)^2\,\omega_{z0}^2} \sin k\omega_{z0}t \sin\omega_{z0}t
\end{aligned}
\tag{2.29}
$$

$$
\begin{aligned}
d_{ZR} =& C_0 t + \frac{C_t t^2}{2} + \frac{C_{tt} t^3}{3} + \frac{C_{ttt} t^4}{4} - \frac{C_{ct}k^2 + C_{ckt}}{k^2 \omega_{z0}} + \frac{C_{sk} + C_s k}{k\omega_{z0}} \\
& + \frac{C_{ct} - (C_s + C_{st}t)\,\omega_{z0}}{\omega_{z0}^2} \cos\omega_{z0}t + \frac{C_{ckt} - k\,(C_{sk} + C_{skt}t)\,\omega_{z0}}{k^2\omega_{z0}^2} \cos k\omega_{z0}t \\
& + \frac{C_{st} + (C_c + C_{ct}t)\,\omega_{z0}}{\omega_{z0}^2} \sin\omega_{z0}t + \frac{C_{skt} + k\,(C_{ck} + C_{ckt}t)\,\omega_{z0}}{k^2\omega_{z0}^2} \sin k\omega_{z0}t
\end{aligned}
\tag{2.30}
$$

Note that Eqs. (2.28) and (2.29) have the same form but different coefficients.

2.3.4   The Velocity Pointing Error Definition and Solution

The velocity pointing error, ρ, shown in Fig. 2.2 is defined as the angle between the desired velocity direction (i.e. along the Z-axis) and the final velocity direction, $\mathbf{V}(t_f)$.

Before thrusting occurs, it is assumed that the body-fixed z-axis is aligned with the inertial Z-axis. During the engine burn, the velocity pointing error is caused by undesired transverse torques and follows the average direction of the inertial angular momentum vector, H_{avg}, over the burn. Fig. 2.2(a) shows the velocity pointing error due to constant torque; Fig. 2.2(b) shows how the velocity pointing error can be significantly reduced due to linear torque (ramp-up scheme). This behavior is discussed by Javorsek and Longuski [37].

(a) Constant torque　　　　　　　(b) Linear torque
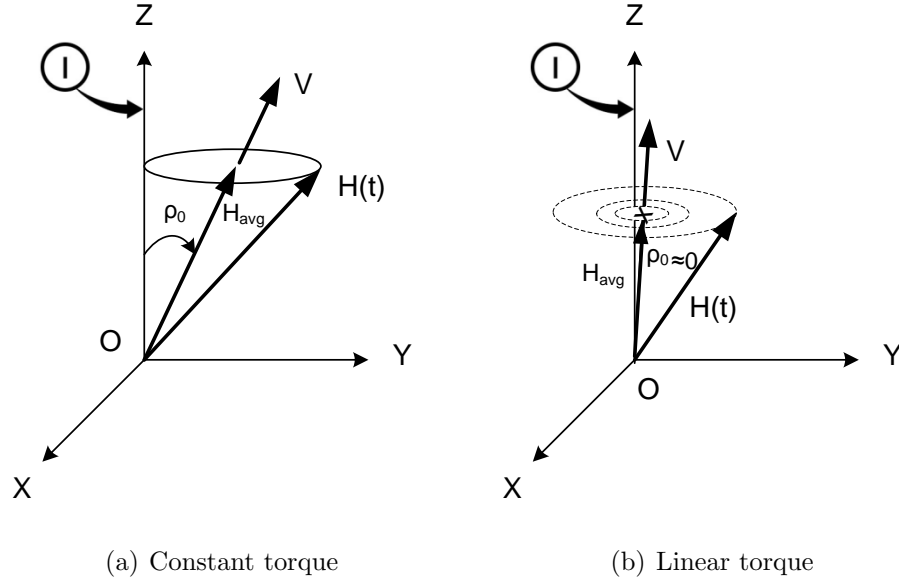
Figure 2.2. Velocity pointing error for two thrust profiles.

The velocity pointing error is defined as [37]

$$\rho \equiv \sqrt{\rho_X^2 + \rho_Y^2} \tag{2.31}$$

where ρ_X and ρ_Y are the velocity pointing error angles defined as

$$\tan \rho_X \equiv V_X/V_Z$$
$$\tan \rho_Y \equiv V_Y/V_Z \tag{2.32}$$

Since the velocity pointing error is small ($\ll 1$ rad), the velocity pointing error angles can be simplified to

$$\rho_X \approx V_X/V_Z$$
$$\rho_Y \approx V_Y/V_Z \tag{2.33}$$

2.3.5 Simplified Form of Velocity Pointing Error

The closed-form solution of the velocity pointing error has many terms when the forces and torques occur in all three directions. To simplify the velocity pointing error equations, assume the initial conditions are all zero, consider only the higher order terms (A_{tt}, B_{tt}, C_{tt}, and C_{ttt}) in Eqs. (2.25)–(2.27), and let

$$M_x(t) = c_{1x}t$$
$$f_z(t) = f_{1z}t \tag{2.34}$$
$$M_y = f_y = f_x = 0$$

Then the velocity pointing error equations are

$$\frac{V_X}{V_Z} = -\frac{c_{1x}\left(I_x k_x + 2I_z \cos \omega_{z0}t\right)}{I_z I_x k_x \omega_{z0}^3} \tag{2.35}$$

$$\frac{V_Y}{V_Z} = -\frac{2c_{1x}}{I_x k_x \omega_{z0}^3} \sin \omega_{z0}t \tag{2.36}$$

A more accurate (albeit more complicated) form for the velocity pointing error that includes ω_{x0}, ω_{y0}, and f_{1y} can be found in the numerical analysis section.

Equations (2.35) and (2.36) represent a circle with a radius of $2c_{1x}/(I_x k_x \omega_{z0}^3)$ and a center that is located $-c_{1x}/(I_z \omega_{z0}^3)$ away from the y-axis as shown qualitatively in Fig. 2.2(a). It is interesting to note that Eqs. (2.35) and (2.36) can be used to predict the behavior of the trapezoidal scheme of Javorsek and Longuski [37] which has three phases: ramp-up, thrusting at F_{max}, and ramp-down. In their scheme, the final velocity pointing error is in agreement to that given by Eqs. (2.35) and (2.36).

2.4 Simulation and Numerical Analysis

MATHEMATICA® and MATLAB® are used to verify the analytical solutions, i.e. Eqs. (2.18) – (2.20), (2.22) – (2.24), (2.11), and (2.12). The simulation uses a built in MATLAB® integrator, ode45, which is based on the Dormand Prince method, an explicit Runge-Kutta formula, to solve for the differential equations numerically. The variable step size integral uses tight relative and absolute error tolerances (on the order of 10^{-13}) and normal control.

To test the accuracy of the theory for the ramp-up maneuver, the mass properties and initial conditions are modeled on the insertion of the Ulysses spacecraft into an interplanetary trajectory to Jupiter. The Ulysses spacecraft was launched in 1990 from the Space Shuttle and used a Payload Assist Model (PAM) for insertion. The PAM has a total burn time of around 85 seconds with a maximum thrust, F_{max}, of 76,100 N and a total impulse, $\mathfrak{I}$, of 5.67×10^6 N·s.[†] The ramp time which minimizes the velocity pointing error is given by [37]

$$t_r = t_b - \mathfrak{I}/F_{max} \approx 10.6 \text{ s} \tag{2.37}$$

Javorsek and Longuski [37] used a t_r of 10.3 seconds, but the small difference is negligible to the results which follow.

For the present purpose, a fictitious thrust profile is used. The Ulysses PAM modeled here is a solid rocket motor, and while nontrivial, the propellant grain geometry or the choice of fuel and oxidizers in a solid rocket can be changed to model the fictitious thrust profile presented in this chapter. Furthermore, a liquid rocket engine that can be throttled is also an option to achieve the linear ramp-up profile [68].

The approximate mass, moments of inertia, and initial spin rates of the Ulysses spacecraft and attached PAM are [37]

$$m = 2500 \text{ kg}, \qquad I_x = I_y = 858 \text{ kg} \cdot \text{m}^2, \qquad I_z = 401 \text{ kg} \cdot \text{m}^2 \tag{2.38}$$

$$\omega_z(0) = 70 \text{ rpm}, \qquad \omega_x(0) = \omega_y(0) = \phi_x(0) = \phi_y(0) = \phi_z(0) = 0 \tag{2.39}$$

[†]*ATK Products Catalog*, www.atk.com/capabilities_space/documents/atk_catalog_may_2008.pdf
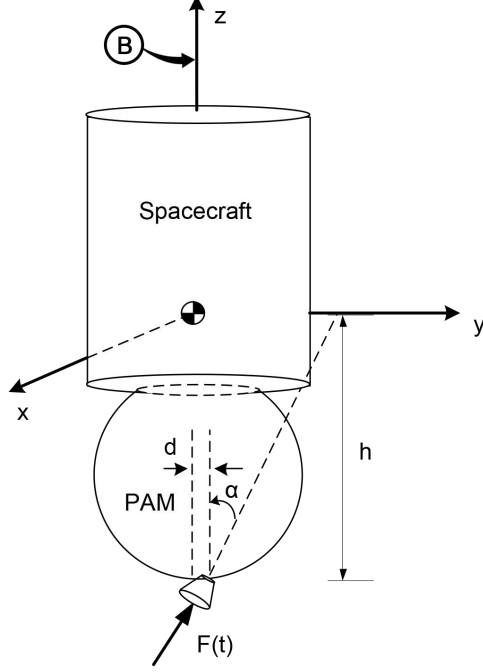
Figure 2.3. Model of Ulysses spacecraft with attached PAM [37].

The Ulysses spacecraft is modeled as shown in Fig. 2.3 with a thruster offset, d, and a thruster misalignment, α. The distance from the nozzle throat to the center of mass (assumed to be constant) is h. The values used in this simulation are

$$d = 0.02 \text{ m}, \qquad \alpha = 0.25 \text{ deg}, \qquad h = 0.8 \text{ m} \qquad (2.40)$$

In the example of the Ulysses spacecraft, all the initial conditions for angular velocity, Euler angles, velocity, and displacement except for ω_{z0} are set to zero. The case discussed by Javorsek and Longuski [37] which involves a ramp-up to maximum thrust, followed by an interval of maximum thrust, and completed by a ramp-down to zero thrust, serves to highlight the generality of the analytical solution. In this example, however, the constant burn phase is eliminated because no solution currently exists for the constant torque and variable mass case, so a triangular thrust profile is used. It is assumed that in the ramp-up phase, all the initial conditions except for ω_{z0} are set to zero, but at the end of the ramp-up phase, the values of ω_{xf}, ω_{yf}, ϕ_{xf},

ϕ_{yf}, ϕ_{zf}, V_{Xf}, V_{Yf}, V_{Zf}, d_{Xf}, d_{Yf}, and d_{Zf} are nonzero. These final conditions at the end of the ramp-up become the initial conditions for the ramp-down phase. This example, provides a stringent test of the nonzero initial condition analytical solution.

In the triangular thrust profile that is used, the thrust linearly increases to its maximum value in the ramp time, t_r, and then linearly decreases from its maximum value to zero in the same amount of time. The total burn time is twice the ramp time or 21.2 seconds. For this simulation, the force profile is

$$F(t) = \begin{cases} (F_{max}/t_r)\, t; & t < t_r \\ F_{max} - (F_{max}/t_r)\, t; & t_r \leq t \leq 2t_r \\ 0 & \text{otherwise} \end{cases} \tag{2.41}$$

As noted earlier, two different inertial reference frames are used in the analytical solution. Because the initial Euler angles for the ramp-up phase are zero, the two reference frames, I and R, are the same in this phase. The ramp-down analytical solutions are first found in the R-frame by Eqs. (2.25) – (2.30) assuming zero initial Euler angles, velocity, and displacement. The solutions are rotated into the original inertial reference frame. Then the nonzero initial velocity and displacement values are added as given in Eqs. (2.11) – (2.12).

Because the thruster offset, d, and the misalignment angle, α, are in the body-fixed y-z plane, the only torque the thruster produces is M_x where

$$M_x(t) = F(t)(h \sin \alpha + d \cos \alpha), \qquad M_y = M_z = 0 \tag{2.42}$$

For the simulation, the term "exact" is used to represent the results of a highly precise numerical integration of Eqs. (2.1), (2.5) – (2.7), and (2.15). The analytical solution is found using Eqs. (2.19), (2.20), (2.22), (2.23), and (2.11) – (2.12).

Figure 2.4 and Fig. 2.5 present the angular velocities and the Euler angles respectively. The analytical and exact solutions are indistinguishable for the entire burn for both the angular velocities and the Euler angles. All of the solutions dramatically change at 10.6 seconds when the ramp-down phase begins.

(a) $\omega_x(t)$ (b) $\omega_y(t)$
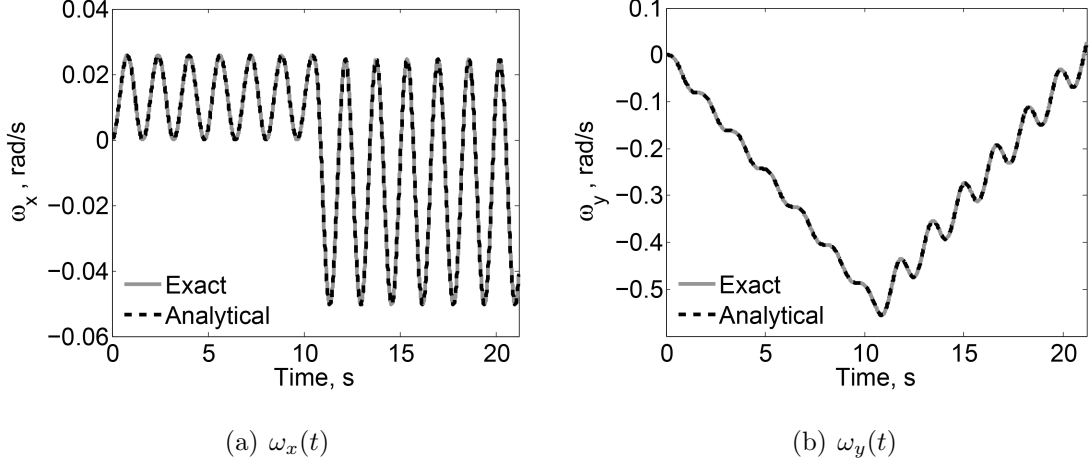
Figure 2.4. Angular velocities for exact and analytical cases.

(a) $\phi_x(t)$ (b) $\phi_y(t)$
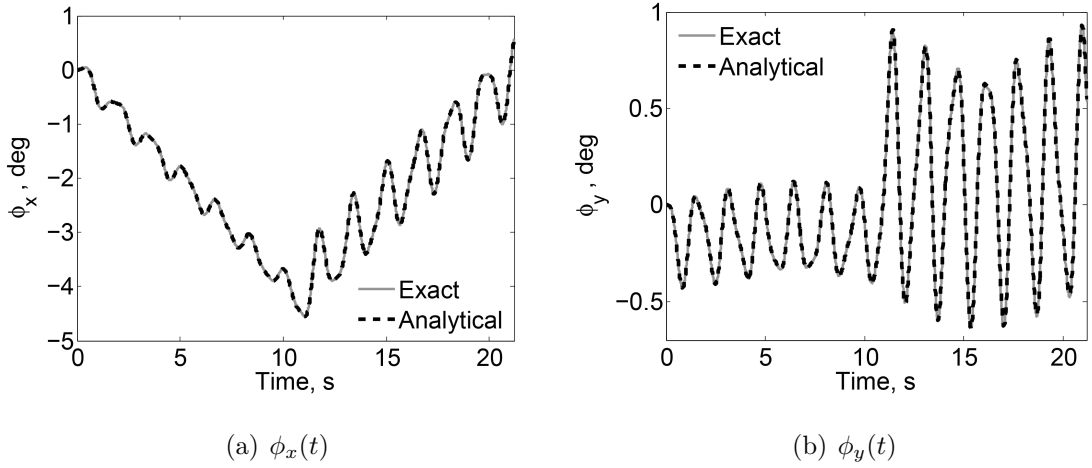
Figure 2.5. Euler angles for exact and analytical cases.

The ω_x solution originally oscillates around an average value of 0.013 rad/s with an amplitude of 0.013 rad/s, but during the ramp-down phase, the solution oscillates around -0.013 rad/s with an amplitude of 0.037 rad/s. The amplitude increase is due to the second set of initial conditions (i.e. ω_{x0} and ω_{y0}) positively contributing to the coefficients in front of periodic terms in Eq. (2.19). The period of the oscillations are unchanged since ω_{z0} is constant. The ω_y solution linearly decreases to -0.55 rad/s

and then linearly increases to 0.024 rad/s due to c_{1x} changing signs. The ω_y solution is not symmetric because of the ramp-down phase's nonzero initial conditions.

The Euler angles appear to have the opposite behavior. The ϕ_x solution decreases linearly to -4.5 deg and then increases to 0.5 deg while ϕ_y oscillates from -0.4 to 0.1 deg and then from -0.6 to 0.9 deg. Once again, the sudden change in the solutions occurs at the beginning of the ramp-down phase with the addition of nonzero initial conditions. As a rule of thumb, the Euler angles must be less than approximately 15 deg for the exact and analytical solutions to closely match. The oscillations in Fig. 2.4 exhibit simple harmonic motion while the oscillations in Fig. 2.5 are more complicated because the Euler angle solutions include additional circular terms with a frequency of $k\omega_{z0}$.

The velocity solutions plotted in Fig. 2.6 are indistinguishable until the end of the ramp-up phase when the analytical solution begins to diverge slightly from the exact solution; the same is true of the exact and analytical velocity pointing error in Fig. 2.7. The errors in the solution are relatively small and caused by compounding errors from the angular velocities and Euler angles.
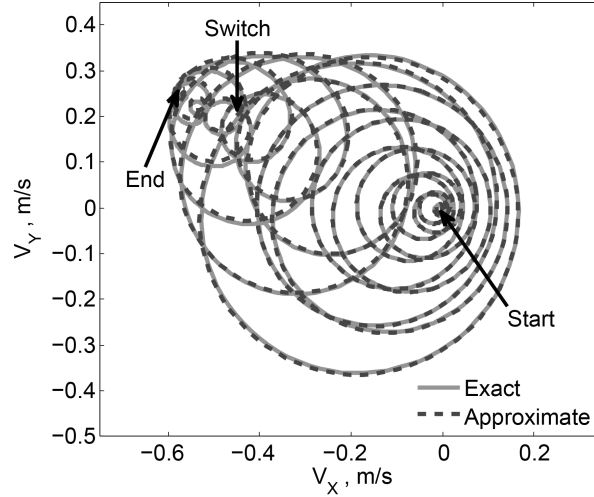
Figure 2.6. Exact and analytical V_X and V_Y solutions.
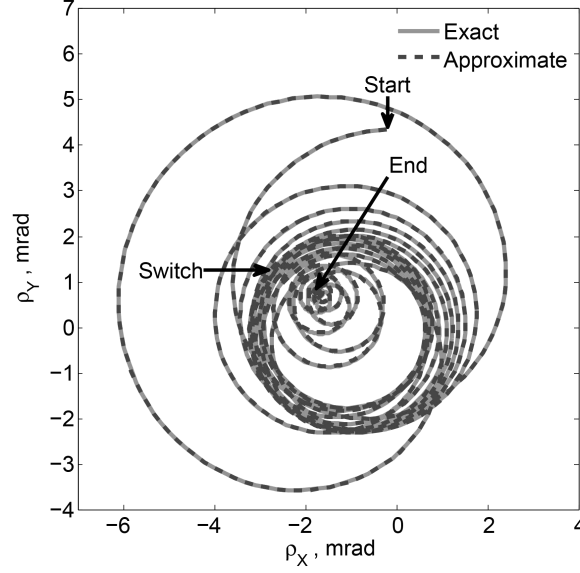
Figure 2.7. Exact and analytical velocity pointing errors.
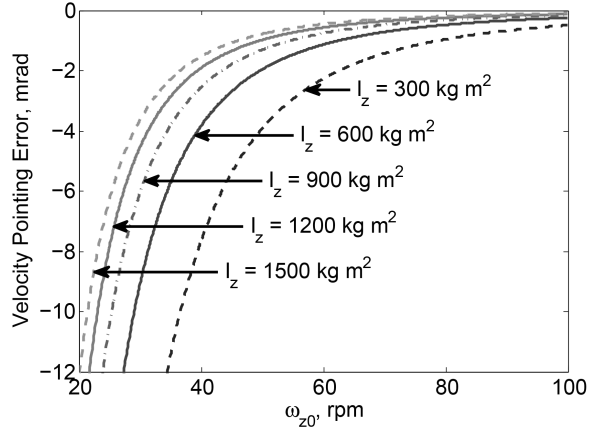
Figure 2.8. Velocity pointing errors using Eq. (2.43) for varying I_z and ω_{z0}.

The ramp-up phase in Fig. 2.6 begins at the origin and then spirals out into larger circles. The ramp-down phase involves the off-center circles which have decreasing radii. In Fig. 2.7, the pointing error begins away from the origin and then forms a circular solution. During the ramp-down phase, the solution spirals asymptotically to a point.

The velocity pointing error is found by dividing the transverse velocity components in Fig. 2.6 by the axial velocity. Ending at 320 m/s, the axial velocity is significantly larger than the transverse velocities. The average velocity pointing error for the ramp-up phase is determined by substituting values into Eqs. (2.35) and (2.36) which results in a circle with radius of 1.9 mrad and a center at (-1.1, 0) mrad. When fitting a circle to the ramp-up phase's last few tenths of a second, the numerical results compares favorably to the simplified analytical results. The simplified analytical equations assume zero initial conditions, so they cannot predict the pointing error for the ramp-down case. With the introduction of nonzero initial Euler angles, the pointing error for the ramp-down case contains circular terms in both the numerator and denominator and is no longer simple. By the end of the ramp-down phase, the pointing error asymptotically approaches a point at around (-1, 1) mrad.

Using Eqs. (2.35) and (2.36), the average pointing error can be estimated as

$$\rho_{avg} = -\frac{c_{1x}}{I_z \omega_{z0}^3} \tag{2.43}$$

Changing c_{1x} results in a linear change in the pointing error, but the other two variables have an inverse relationship. To see how I_z and ω_{z0} change the pointing error, consider Fig. 2.8. Clearly, as the spin rate increases, the pointing error decreases. Also as I_z increases or the spacecraft becomes more disk-like, the pointing error also decreases. Figure 2.8 is useful to find spacecraft parameters based on desired spin rates or pointing error. For example, if the spacecraft is to be spun at 20 rpm and have a pointing error of less than 2 mrad, I_z would have to be greater than 1200 kg·m^2. Alternatively, one could choose an acceptable pointing error for a specific value of I_z and find the resulting initial spin rate.

At an intermediate step in the process of deriving Eqs. (2.35) and (2.36), the velocity pointing error is as follows

$$\frac{V_X}{V_Z} = -\frac{3f_{1z}\left(c_{1x} - I_x\omega_{z0}^2\omega_{x0}\right)I_x k_x + 6f_{1z}I_z \cos\omega_{z0}t}{\omega_{z0}I_z\left(3f_{1z}I_x k_x\omega_{z0}^2 + 2f_{1y}c_{1x}t\right)} \tag{2.44}$$

$$\frac{V_Y}{V_Z} = \frac{3f_{1z}\omega_{z0}^2\omega_{y0}I_y I_x k_x - 6f_{1z}c_{1x}I_z \sin\omega_{z0}t}{\omega_{z0}I_z\left(3f_{1z}I_x k_x\omega_{z0}^2 + 2f_{1y}c_{1x}t\right)} \tag{2.45}$$

where f_{1y}, ω_{x0}, and ω_{y0} are no longer zero. At first glance, the time term in the denominator suggests that the pointing error goes to zero as time goes to infinity. However, the ramp-up time is finite, and f_{1y} produces an insignificant effect in practice, 0.2 μrad, over the ramp-up time for this Ulysses example. The nonzero angular velocities are included to demonstrate that it is much easier to include them than nonzero Euler angles. By increasing α; f_{1z}, f_{1y}, and c_{1x} change so that the numerator increases faster than the denominator for a given (fixed) ramp-up time.
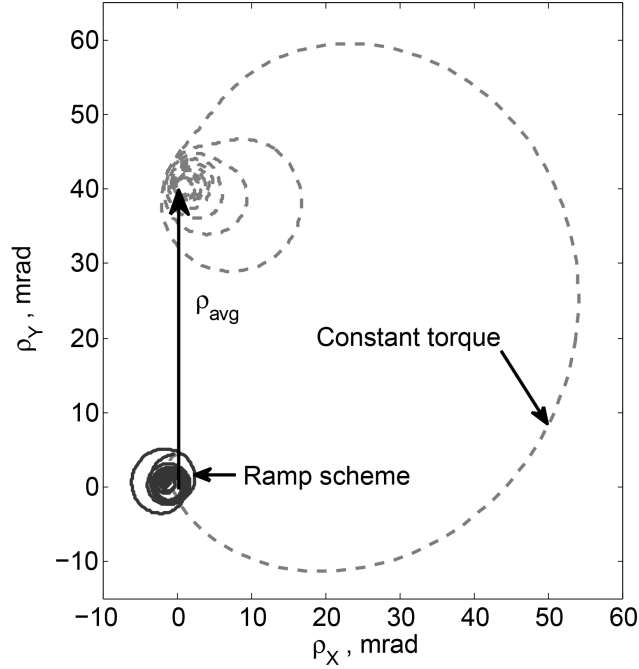
Figure 2.9. Velocity pointing errors for constant torque and ramp scheme.

To show how effective the ramp-up scenario is to reducing the pointing error, the same simulation was run with a constant thrust profile as shown in Fig. 2.9. The constant thrust profile has the same total impulse as the previous scheme with a constant thrust of $F_{max}/2$. The constant force has an average velocity pointing error of around 41 mrad which is more than twenty times larger than the pointing error of the ramp-up maneuver (followed by the ramp-down) of around 2 mrad. The average velocity pointing error for the constant torque was determined by running

the simulation until it converged on a point. Incidentally, a simplified analytical expression for the velocity pointing error is [35]

$$\rho_X = -M_y/(I_z\omega_{z0}^2)$$
$$\rho_Y = M_x/(I_z\omega_{z0}^2)$$

(2.46)

For this example, the average pointing error from Eq. (2.46) is 41 $mrad$ and within 2.5% of the actual value (40 mrad). This discrepancy is due to the fact that the term $\phi_y\omega_x$ which was dropped from Eqs. (2.6) and (2.7) is much larger for the constant burn than for the linear ramp. Adding the side force, f_y, into Eq. (2.46), results in a negligible change of the pointing error of less than 0.02%.
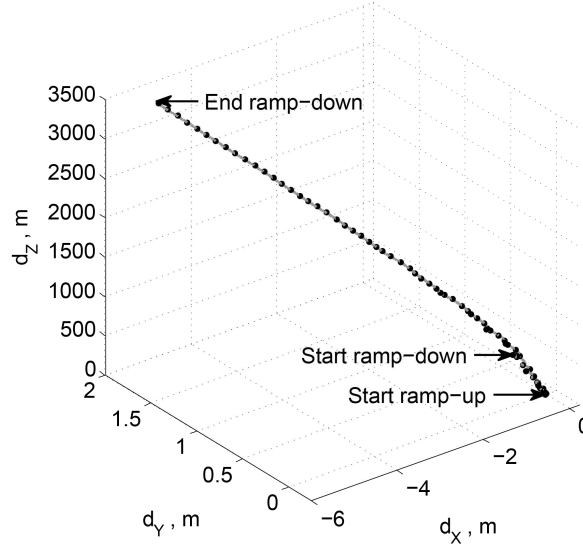
Figure 2.10. Displacement solution for exact (gray line) and analytical solutions (dots).

Assuming the velocity pointing error of the constant thrust profile (about 40 mrad) is acceptable for a 70 rpm spin rate, a spacecraft with a ramp profile could be spun at a lower rate. Using Eq. (2.43), the spacecraft with a ramp profile would only need to be spinning at about 21 rpm which is a 70% decrease.

Figure 2.10 presents the inertial displacement of the spacecraft obtained by Eq. (2.12). The exact and analytical solutions are indistinguishable from each other.

Note that the axes are not equally scaled. During the ramp-up phase, the solution has the appearance of a stretched-out spring with smaller coils at the beginning of the simulation and larger coils at the end. In the ramp-down phase, the coils become smaller as the thrust decreases until the trajectory appears to become linear. At the end of the simulation, the exact and analytical solutions are 7.9 m apart. Since the ending displacement is around 3400 m, the difference between the two solutions is less than 0.3%.

It is interesting to note that a remarkably simple approximation for the displacement can be obtained for the ramp-up phase by multiplying the third-order term in Eq. (2.30), $C_{tt}t^3/3$, by the average velocity pointing error given by Eqs. (2.35) and (2.36). The result of this simple approximation is illustrated by the asymptotic line in Fig. 2.11 which passes through the center of the "stretched-out spring." This approximation could be useful in the assessment of spinning spacecraft maneuvers that are, for example, in proximity to the International Space Station or other spacecraft.
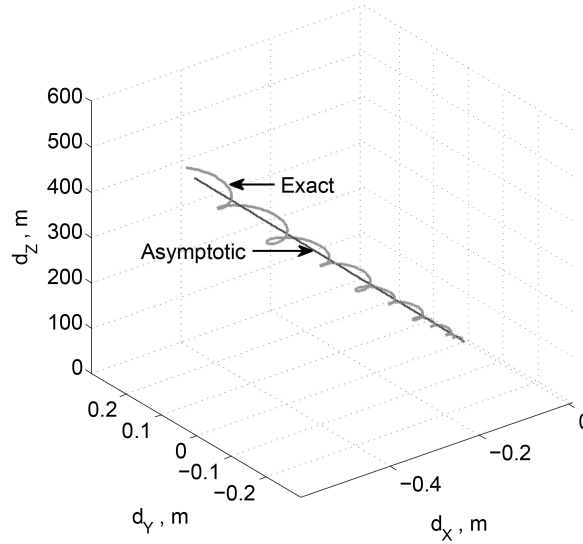
Figure 2.11. Ramp-up phase displacements for exact and asymptotic solutions.

2.5   Summary

This chapter has developed an analytical theory for the ramp-up and ramp-down thrust profiles that provide highly accurate, approximate solutions for the angular velocity, Euler angles, inertial velocity, and inertial displacement. The solutions contain both secular and circular terms that are functions of the moments of inertia, initial spin rate, torques, forces, and time. Asymptotic solutions are derived from the general theory which leads to compact, simple equations that capture the essential spacecraft behavior.

Numerical tests have validated the theory including a hypothetical spin-stabilized spacecraft with a Payload Assist Module. In this case, the velocity pointing error is reduced by an order of magnitude over the usual constant burn profile. If the velocity pointing error for the constant thrust profile was acceptable, the spin rate could be reduced by as much as 70%.

3. Velocity Pointing Error Reduction for Spinning Thrusting Spacecraft via Heuristic Thrust Profiles

3.1 Background

The motion of spacecraft subject to body-fixed forces and torques is discussed by Leimanis in his classic treatise, *The General Problem of the Motion of Coupled Rigid Bodies about a Fixed Point* [1]. In many cases, spacecraft can be treated as spinning symmetric or nearly-symmetric rigid bodies. During axial thrusting of a spinning spacecraft, thrust misalignment and center-of-mass offset create transverse body-fixed torques which perturb the angular momentum vector from its desired inertial direction. The bias in the angular momentum vector directly results in velocity pointing errors which cause the spacecraft to deviate from its desired trajectory, subsequently requiring more propellant for the spacecraft to achieve its mission.

Angular velocity, attitude, and inertial velocity solutions for the spinning spacecraft have been found via perturbation methods [15, 16, 19, 20]. Non-perturbation methods are used to find analytical results for more specific cases such as nearly-symmetric spinning rigid bodies with constant torque [21,22] and time-varying torque [24,25] as well as bodies that are asymmetric [26]. The inertial velocity and displacement solutions for constant torque [32] and linear torque [33] are also known.

Historically, the velocity pointing error has been reduced by spinning at a high rate [34]. It has been shown that if the axial thrust is a linear function of time beginning at zero and ramping up to maximum thrust, the velocity pointing error could be significantly decreased with respect to the usual case where the thrust can be modeled as a step function since the average angular momentum vector for the linear ramp now remains pointing in the desired direction [37].

While a linear thrust profile can reduce velocity pointing errors, it is unclear what is the best scheme to ramp-up the thruster to minimize pointing error. Finding the optimal solution for the thrust history (i.e. the control) to minimize the velocity pointing error is difficult to solve using indirect methods since the solution involves nine nonlinear differential equations and the ending velocity pointing error tends to oscillate at a high frequency (typically 1 rev/s) with respect to the ramp-up time. Instead, a heuristic approach is first taken to find a suboptimal ramp-up profile.

This analysis considers suboptimal ramp-up thrust profiles which are expressed as exponential, logarithmic, parabolic, cosine, sine, and cubic functions. The minimum velocity pointing error from each of these profiles except the sine profile is essentially zero and so can be considered to be an effective solution.

In practice, these profiles may be difficult to realize. The intent of this analysis is to identify a method that, in principle, can passively reduce velocity pointing errors. Despite a thorough literature search, the author does not know of a case where improvements from a modified thrust profile have been observed empirically. A detailed discussion on the practical applications of this method can be found in section 3.4.

3.2 Solution Model

Consider a spinning rigid body depicted in Fig. 3.1. The spacecraft has the undesired transverse torques M_x and M_y, no axial torque, a thrust offset of d, and a thrust misalignment of α. The distance from the center of mass of the vehicle to the nozzle throat, h, is constant for these simulations since h only affects ω_x and ω_y which are two orders of magnitude smaller than w_z. Assume the body-fixed reference frame, B, is located at the center of mass and aligned with the principal axes of the rigid body. Throughout this analysis, capital letters signify the vector in inertial reference frame, I, and lower case letters signify vectors in body-fixed frame, B.
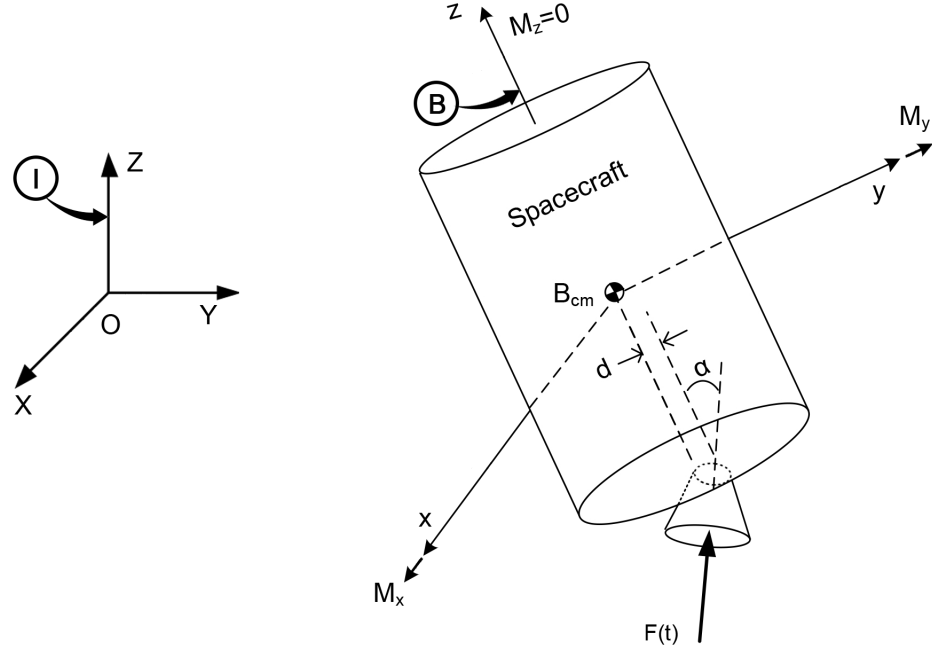
Figure 3.1. Model for thrusting, spinning spacecraft.

3.2.1 Velocity Pointing Error

The velocity pointing error, ρ, shown in Fig. 2.2 is once again defined as the time-varying angle between the desired velocity direction (i.e. along the Z-axis) and the ensuing velocity, $\Delta \mathbf{V}$. Before thrusting occurs, it is assumed that the body-fixed z-axis is aligned with the inertial Z-axis. During the engine burn, the undesired transverse torques generate the velocity pointing error; in the cases of the constant and linear force profiles, the velocity pointing error tends to follow the average direction of the inertial angular momentum vector, $\mathbf{H}_{avg}$. Figure 2.2(a) shows the velocity pointing error due to constant torque; Figure 2.2(b) shows how the velocity pointing error can be significantly reduced due to linear torque (ramp-up scheme). This behavior is discussed by Javorsek and Longuski [37].

The velocity pointing error is given by Eq. (2.31). Since the velocity pointing error is small ($\rho \ll 10$ degrees), the velocity pointing error angles are simplified to Eq. (2.33).

3.2.2 Ramp-Up Scheme

The linear ramp-up scheme given by Javorsek and Longuski [37] is used as inspiration for this analysis to reduce the velocity pointing error. In the linear ramp-up scheme shown in Fig. 3.2 (as solid lines), the thrust linearly increases from zero to its maximum value with constant mass properties, burns at maximum with changing mass properties, and then at burn out discontinuously decreases to zero. While the linear ramp-up profile dramatically decreases the velocity pointing error, other ramp-up profiles, also illustrated in Fig. 3.2 (as dashed lines), may reduce the pointing error further.
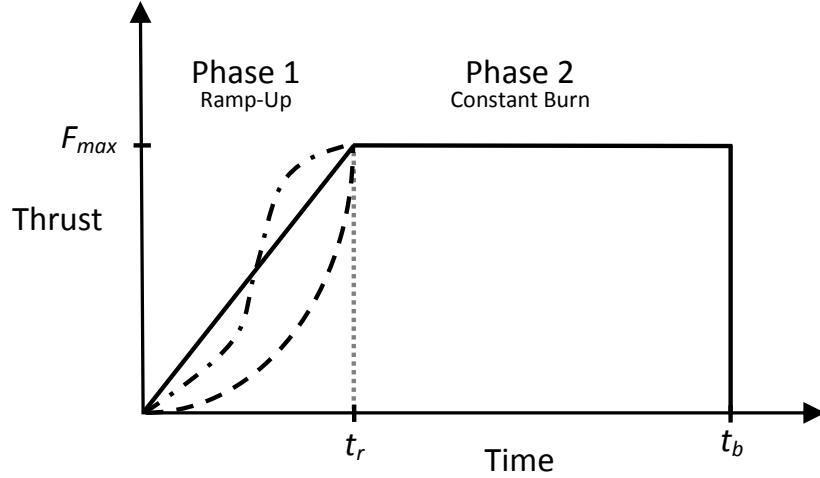
Figure 3.2. Linear ramp-up scheme thrust profile adapted from Javorsek and Longuski [37] modified by different ramp-up profiles.

To fairly compare the different ramp-up profiles, the total impulse, $\mathfrak{I}$, remains constant and the profiles end at the same maximum force, F_{max}. To satisfy these constraints, the ramp-up time, t_r, for each profile can vary such that

$$\mathfrak{I} = \int_0^{t_r} F(t)dt$$

$$F(t_r) = F_{max}$$

(3.1)

In addition to these two equality constraints, the force is also constrained to be between zero and maximum thrust so that

$$0 \leq F(t) \leq F_{max}$$

(3.2)

An example of the velocity pointing error for a cubic ramp-up profile is shown in Fig. 3.3. The other thrust profiles produce similar figures. At the beginning of Phase 1, shown in black, the velocity pointing error is large (around 4 mrad). The velocity pointing error does not start at zero due to the nonzero thrust misalignment. By the end of Phase 1, the velocity pointing error forms an approximate circle. During Phase 2, shown in gray, the pointing error spirals down to a very small circle (with a radius of 0.02 mrad) which is obscured by the many revolutions of the converging trajectory. The ending velocity pointing error in Fig. 3.3 is approximately 0.

Ideally, one could analytically solve for the velocities where the optimal control for $F(t)$ is found by setting the final velocity components to have zero pointing error. This approach was considered and rejected because the equations of motion governing Phase 2 are analytically intractable.

A second approach is to use indirect optimization. To find the optimal ramp-up profile, a two-point boundary-value problem (TPBVP) was previously explored (see Appendix B). To solve the TPBVP, the velocity pointing error was evaluated at the end of Phase 1 to obtain a transversality condition. Even with this simplification, no converged solution was found. A new approach was deemed necessary.

Finally, a direct approach, in which heuristic solutions were considered, led to practical solutions. Some of these solution provide such small velocity pointing errors that they can be considered an effective solution.
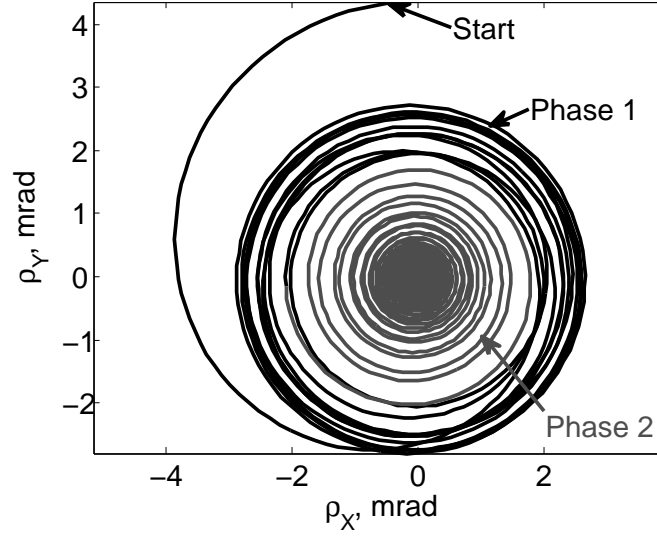
Figure 3.3. Velocity pointing error example for Phase 1 (black) and Phase 2 (gray) for a cubic ramp-up profile.

3.2.3 Equations of Motion for the Ramp-Up Phase

The heuristic force profiles considered in this analysis which begin at zero have the form of

$$F(t) = c_1 \left[\exp(c_2 t) - 1 \right] \tag{3.3}$$

$$F(t) = c_1 \log \left(c_2 t + 1 \right) \tag{3.4}$$

$$F(t) = c_1 \sin c_2 t \tag{3.5}$$

$$F(t) = c_1 (1 - \cos c_2 t) \tag{3.6}$$

$$F(t) = c_1 t + c_2 t^2 \tag{3.7}$$

$$F(t) = c_1 t + c_2 t^2 + c_3 t^3 \tag{3.8}$$

where c_1, c_2, and c_3 are constants.

The force profiles in Eqs. (3.3)–(3.7) have three unknown parameters, two constant coefficients (c_1 and c_2) and the ramp-up time. With the two equality constraints in Eq. (3.1), varying the ramp-up time will yield all available force profiles. The ramp-up time range is limited by the inequality constraints in Eq (3.2).

The cubic force profiles in Eq. (3.8) have an additional unknown parameter, c_3. With the two equality constraints in Eq. (3.1) and the inequality constraints in Eq. (3.2), varying the the ramp-up time and one free parameter c_1 will yield all available force profiles. Since the two inequality constraints in Eq. (3.2) severely limit the search space, a two-dimensional grid search (i.e. a two parameter optimization) can find the best case for a certain total impulse and maximum force.

To find the velocity of a spinning spacecraft, three sets of differential equations are needed: angular velocity rate equations, kinematic equations to describe how the B-frame is moving relative to the I-frame, and acceleration equations which rotate the B-frame forces to the I-frame.

Since the engine ramp-up time is much shorter than the total burn time, the mass properties are assumed to be constant for the ramp-up phase. Then the angular velocity of a spacecraft, described by Euler's equations of motion [66], is

$$
\begin{aligned}
\dot{\omega}_x(t) &= M_x/I_x - \left[(I_z - I_y)/I_x\right]\omega_y\omega_z \\
\dot{\omega}_y(t) &= M_y/I_y - \left[(I_x - I_z)/I_y\right]\omega_z\omega_x \\
\dot{\omega}_z(t) &= M_z/I_z - \left[(I_y - I_x)/I_z\right]\omega_x\omega_y
\end{aligned}
\tag{3.9}
$$

where ω_x, ω_y, and ω_z are components of the angular velocity vector in the B-frame; I_x, I_y, and I_z are constant principal moments of inertia; and M_x, M_y, and M_z are torques along the body-fixed x, y, and z axes, respectively.

Without loss of generality, assume the spin axis is the z-axis which may be either the minimum or maximum moment-of-inertia axis. If I_z were the intermediate moment-of-inertia, it is well known that the spacecraft attitude motion would be unstable. In this analysis, the vehicle is assumed to be a thrusting, spinning spacecraft in which the axial torque, M_z, is zero. The non-axial torques have the same heuristic profile as the forces.

The kinematic equations describe the orientation of a rigid body with respect to the inertial reference frame, I. For this analysis, a Type-I, Euler sequence 3-1-2 (ϕ_z, ϕ_x, ϕ_y) given by Wertz [67] is used where

$$
\begin{aligned}
\dot{\phi}_x &= \omega_x \cos \phi_y + \omega_z \sin \phi_y \\
\dot{\phi}_y &= \omega_y - (\omega_z \cos \phi_y - \omega_x \sin \phi_y) \tan \phi_x \\
\dot{\phi}_z &= (\omega_z \cos \phi_y - \omega_x \sin \phi_y) \sec \phi_x
\end{aligned}
\tag{3.10}
$$

The velocity solution can be found by rotating the body-fixed forces from the B-frame to the I-frame by using the following Type-I 3-1-2 direction cosine matrix [67]

$$
{}^{I}\mathbf{R}_{312}^{B} =
\begin{bmatrix}
c\phi_y c\phi_z - s\phi_x s\phi_y s\phi_z & -c\phi_x s\phi_z & s\phi_y c\phi_z + s\phi_x c\phi_y s\phi_z \\
c\phi_y s\phi_z + s\phi_x s\phi_y c\phi_z & c\phi_x c\phi_z & s\phi_y s\phi_z - s\phi_x c\phi_y c\phi_z \\
-c\phi_x s\phi_y & s\phi_x & c\phi_x c\phi_y
\end{bmatrix}
\tag{3.11}
$$

where c and s are abbreviations for cosine and sine functions, respectively.

The I-frame velocities can be solved by integrating

$$
\begin{Bmatrix}
\Delta \dot{V}_X \\
\Delta \dot{V}_Y \\
\Delta \dot{V}_Z
\end{Bmatrix}
= {}^{I}\mathbf{R}_{312}^{B}
\begin{Bmatrix}
f_x/m \\
f_y/m \\
f_z/m
\end{Bmatrix}
\tag{3.12}
$$

where f_x, f_y, and f_z are the body-fixed forces.

3.2.4   Equations of Motion for the Constant Burn Phase

The second portion of the burn, at maximum thrust, is much longer than the ramp-up phase, so the mass properties of the spacecraft are no longer assumed to be constant. During this phase, the mass and moments of inertia are modeled as linearly decreasing as assumed by Javorsek and Longuski [37]. The mass-flow rate, $\dot{m}$, is assumed to be constant.

The velocity in Phase 2 is found similarly to the velocity in Phase 1 with three sets of differential equations. Equations (3.10)–(3.12) remain the same but now have constant forces and changing mass. The angular velocity equations, however, are

different from Phase 1 and now include jet-damping for a higher fidelity model. Following Thomson [69], the angular velocity equations for Phase 2 are

$$
\begin{aligned}
\dot{\omega}_x(t) &= M_x/I_x - \omega_y\omega_z(I_z - I_y)/I_x - \left[\dot{I}_x - \dot{m}(h^2 + d^2)\right]\omega_x/I_x \\
\dot{\omega}_y(t) &= M_y/I_y - \omega_z\omega_x(I_x - I_z)/I_y - \left(\dot{I}_y - \dot{m}h^2\right)\omega_y/I_y \\
\dot{\omega}_z(t) &= M_z/I_z - \omega_x\omega_y(I_y - I_x)/I_z - \left(\dot{I}_z - \dot{m}d^2\right)\omega_z/I_z
\end{aligned}
\tag{3.13}
$$

where h is the distance from the spacecraft's center of mass to the nozzle throat and is assumed to be constant. The axial torque, M_z, is zero, and the remaining body-fixed torques are constant since the spacecraft is burning at a constant maximum thrust. A detailed discussion on jet damping can be found in van der Ha and Janssens [70].

3.3 Simulation and Numerical Analysis

MATLAB® is used to calculate the velocity pointing error for these heuristic thrust profiles. The simulation uses a built in MATLAB® integrator, ode45, which is based on the Dormand Prince method, an explicit Runge-Kutta formula, to solve for the differential equations numerically. The variable step size integral uses tight relative and absolute error tolerances (on the order of 10^{-13}).

To test the accuracy of the theory for the ramp-up maneuver, the mass properties and initial conditions are modeled on the insertion of the Ulysses spacecraft into an interplanetary trajectory to Jupiter [37]. For this simulation, fictitious thrust profiles are used. The Ulysses spacecraft with attached PAM is modeled as shown in Fig. 2.3. The constant values for the offset and misalignment used in this simulation are

$$
d = 0.02 \text{ m}, \qquad \alpha = 0.25 \text{ deg } (4.4 \text{ mrad}), \qquad h = 0.8 \text{ m}
\tag{3.14}
$$

Because the thrust offset, d, and the misalignment angle, α, are in the body-fixed y-z plane, the thrust only produces an x-direction torque, M_x, such that

$$
M_x = F(t)(h\sin\alpha + d\cos\alpha), \qquad M_y = M_z = 0
\tag{3.15}
$$

where $F(t)$ is given by Eqs. (3.3)–(3.8) for Phase 1 and F_{max} for Phase 2. Since the spacecraft is axisymmetric, the y-z plane is defined to be the plane which the thrust offset lies in.

The Ulysses spacecraft was launched in 1990 from the Space Shuttle and used a Payload Assist Model (PAM) for insertion. The PAM has a total burn time of around 85 seconds with a maximum thrust, F_{max}, of 76,100 N and a total impulse, $\mathfrak{I}$, of 5.67×10^6 N s.[†] To find the total impulse for Phase 1, the linear profile ramp time for Phase 1 is defined as [37]

$$t_{rlin} = t_b - \mathfrak{I}/F_{max} \approx 10.6 \text{ s} \tag{3.16}$$

Then the total impulse of the ramp-up phase, which is constant for all the profiles, is determined by

$$\mathfrak{I}_r = F_{max} \ t_{rlin}/2 \approx 4.03 \times 10^5 \text{ N} \cdot \text{s} \tag{3.17}$$

To have the total impulse of the entire burn (Phase 1 and Phase 2) equal the total impulse of the actual PAM, the Phase 2 burn at maximum thrust which is identical for all profiles, lasts for 69.2 seconds. If instead the thruster burns only at maximum thrust (i.e. with no ramp-up), the total burn time for the same total impulse as the PAM would be 74.5 seconds. This burn is shorter than the actual PAM's 85 second burn due to the assumption that the PAM always burns at maximum thrust whereas in reality, the PAM has a smaller average thrust of 67,200 N. An actual PAM is not able to reproduce these thrust profiles but is used for an estimate for maximum thrust and total impulse values. The maximum thrust and total impulse values could be replicated by a liquid or hybrid engine.

In this example, all the initial conditions for angular velocity, Euler angles, and inertial velocity except for ω_{z0} are set to zero for Phase 1. The initial spin rate, w_{z0}, is set to 70 rpm. The constant mass properties for Phase 1 are [37]

$$m(0) = 2500 \text{ kg}, \quad I_x(0) = I_y(0) = 858 \text{ kg} \cdot \text{m}^2, \quad I_z(0) = 401 \text{ kg} \cdot \text{m}^2 \tag{3.18}$$

[†]*ATK Products Catalog*, http://www.atk.com/wp-content/uploads/2013/02/ATK-Motor-Catalog-2012.pdf

The initial conditions for Phase 2 are the final conditions of Phase 1. The moments of inertia at the end of the burn and the constant mass flow rate are [37]

$$\dot{m} = -24 \text{ kg/s}, \quad I_x(t_b) = I_y(t_b) = 222 \text{ kg} \cdot \text{m}^2, \quad I_z(t_b) = 102 \text{ kg} \cdot \text{m}^2 \qquad (3.19)$$

3.3.1 Heuristic Profiles

The heuristic force profiles are shown in Fig. 3.4 with various ramp-up times. These profiles all end at F_{max} and have the same total impulse. The profiles shown in Fig. 3.4 are representative of the studied profiles and do not result in the minimum velocity pointing errors. The complete force profile for the entire ramp scheme (not shown) would also include a constant burn for 69.2 seconds after the ramp-up phase for all of the profiles in Fig. 3.4. The particular force profile which results in the minimum velocity pointing error depends on the mass properties, initial spin rates, thrust misalignment and offset, as well as the distance from the thrust nozzle to the center of mass.
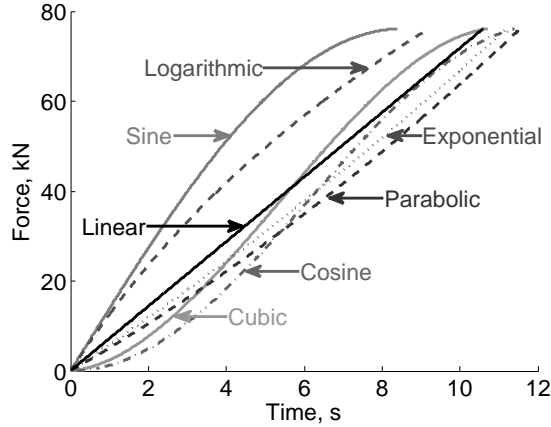
Figure 3.4. Force profile examples for linear, exponential, logarithmic, sine, cosine, parabolic, and cubic (c_1 of 800 N/s) force profiles.

With the exception of the sine and cosine profiles, the heuristic profiles can have ramp-up times that are shorter or longer than the linear ramp-up profile (shown as the black line in Fig. 3.4). The range of available t_r for these profiles is limited due to the inequality constraints.

The cosine and sine profiles are restricted from having longer or shorter ramp-up profiles due to the definition of profiles in Eqs. (3.5) and (3.6) and the fact that they must be shorter than a half period to adhere to the inequality constraints. The sine and cosine profiles could have a larger range of ramp-up times if a phase angle (or equivalently another degree of freedom) was added to Eqs. (3.5) and (3.6). However, adding this additional variable is not considered here since a similar analysis is done with cubic profiles.

A cubic force profile with a c_1 (the free parameter) value of 800 N/s is also shown in Fig. 3.4. Since the cubic force profiles have an additional free variable, there is a range of available c_1 values for this ramp-up time unlike the other profiles which only have one solution for a particular t_r.

As the cubic solutions approach the linear ramp-up time, they become more similar to the cosine curves. Conversely, as the solutions diverge from the linear ramp-up profile, the cubic profiles tend toward the shape of parabolic or exponential profiles. For the remaining profiles (logarithmic, sine, exponential, and parabolic), the profiles become more linear as they approach the linear ramp-up time.

3.3.2 Velocity Pointing Error

The velocity pointing error is found by dividing the transverse velocity components by the axial velocity. At the end of Phase 2, the velocity pointing error has spiraled down to a very small circle (around 0.02 mrad) as represented in Fig. 3.3.

Due to stochastic errors in the real system, it is expected that the velocity pointing error could end at any point on this small circle, so in this analysis, the ending velocity pointing error is *defined* as the point on the circle which is farthest away from the

origin as shown in Fig. 3.5. This velocity pointing error or ρ_{max} is the center, ρ_{cent}, plus the radius, ρ_r, of the small circle. The radius and center are determined by fitting the last 4% of the data to a circle. This definition of ρ_{max} slightly overestimates the actual velocity pointing error and can never be zero.
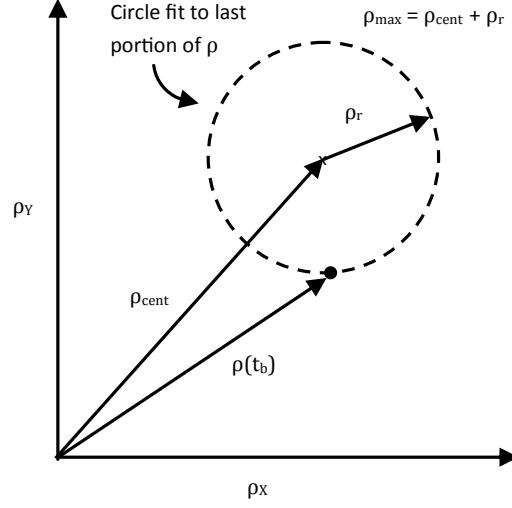
Figure 3.5. The definition of ρ_{max} is based on a circle fit of the last portion of the velocity pointing error, ρ.

The maximum ending velocity pointing errors for the one parameter profiles are shown in Fig. 3.6. In general, the exponential, parabolic, logarithmic, and sine profiles with ramp-up times that are much shorter than the linear ramp-up time have larger ρ_{max}. Only when the ramp-up time of these profiles approaches the linear ramp-up time does ρ_{max} become smaller than the linear ρ_{max}. As the ramp-up times of the parabolic, logarithmic, exponential, and cosine profiles initially increase over the linear ramp-up time, the profiles have a smaller ρ_{max} than the linear profile. If the engine burned at F_{max} for the entire burn, the ρ_{max} would be around 74 mrad.

Near the linear ramp-up time, the logarithmic, exponential, sine, and parabolic profiles have similar ρ_{max} because the force profiles in this range are almost identical. However, the ρ_{max} for the exponential, sine, and logarithmic profiles are not available
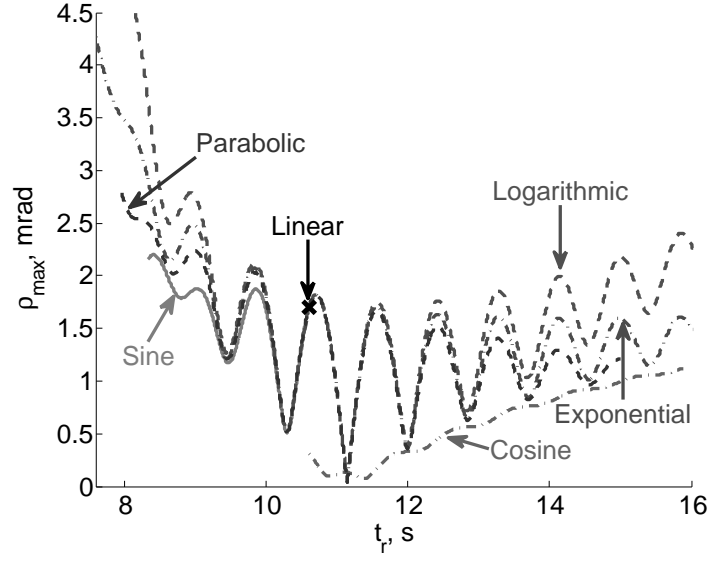
Figure 3.6. Velocity pointing error for linear, parabolic, sine, cosine, logarithmic, and exponential profiles.

less than 0.2 seconds away from the linear ramp-up time because of mathematical convergence problems when solving for the constant coefficients in Eqs. (3.3)–(3.6).

As the ramp-up time increases further, the ρ_{max} of the heuristic profiles diverge. At around 14 seconds, the logarithmic profile diverges from the parabolic and exponential profiles and begins to linearly increase with smaller oscillations to around 7 mrad at 25 seconds. The cosine, parabolic, and exponential profiles appear to approach 1.7 mrad.

The parabolic, sine, logarithmic, and exponential profiles have sensitivities to t_r as shown by the large oscillations in ρ_{mas} in Fig. 3.6. However, the cosine profile, which does not produce the minimum ρ_{max}, is overall less sensitive to changes in t_r.

To compare cubic profiles with the one parameter profiles, consider Fig. 3.7. Here of the linear profile (black "x"), parabolic profiles (gray dashed line), logarithmic profiles (lighter gray dashed and dotted line), and cosine profiles (lightest dashed and dotted line) of Fig. 3.6 are plotted against a range of cubic profiles (solid lines).
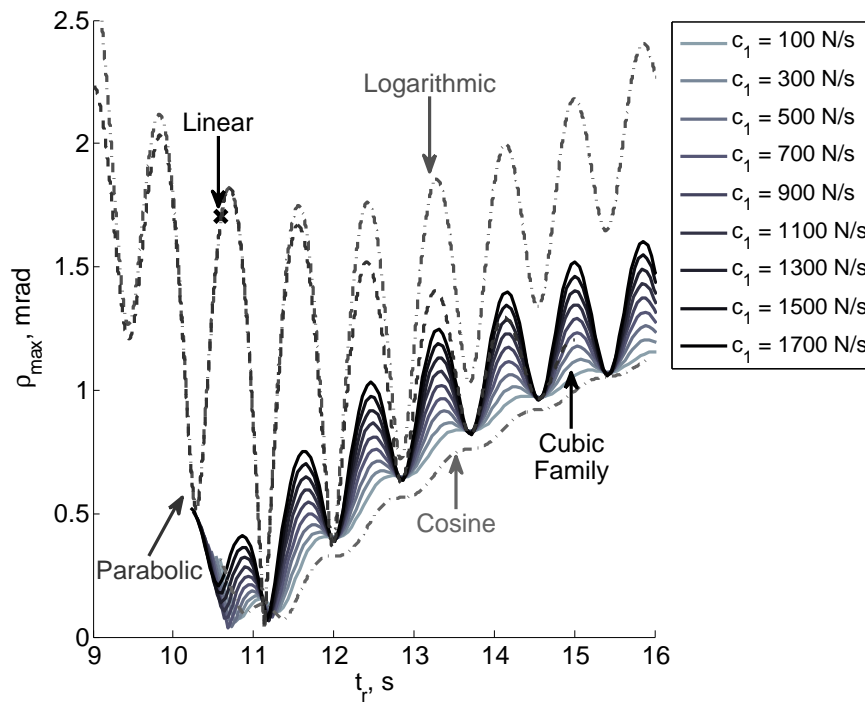
Figure 3.7. Comparison of velocity pointing errors for linear, logarithmic, cosine, parabolic, and a small set of cubic profiles.

The exponential profiles (not shown in Fig. 3.7) have similar results to the parabolic profiles.

The best solution for the one parameter profiles is a logarithmic solution which has a minimum velocity pointing error of 0.04 mrad with a ramp-up time of 11.1 seconds. Some of the cubic profiles in Fig. 3.7 not only have a lower minimum velocity pointing error than the logarithmic profile with a minimum of 0.02 mrad but also have smaller oscillation amplitudes. While the cubic profiles shown in Fig. 3.7 have a lower minimum than the cosine profile, the cosine profile is once again less sensitive to changing ramp-up time. As the ramp-up time increases, the ρ_{max} of the low c_1 cubic profiles approaches 1.7 mrad.

Figure 3.8 shows the velocity pointing error for the entire search space of the cubic thrust profiles. The shape of the search space is determined by the inequality
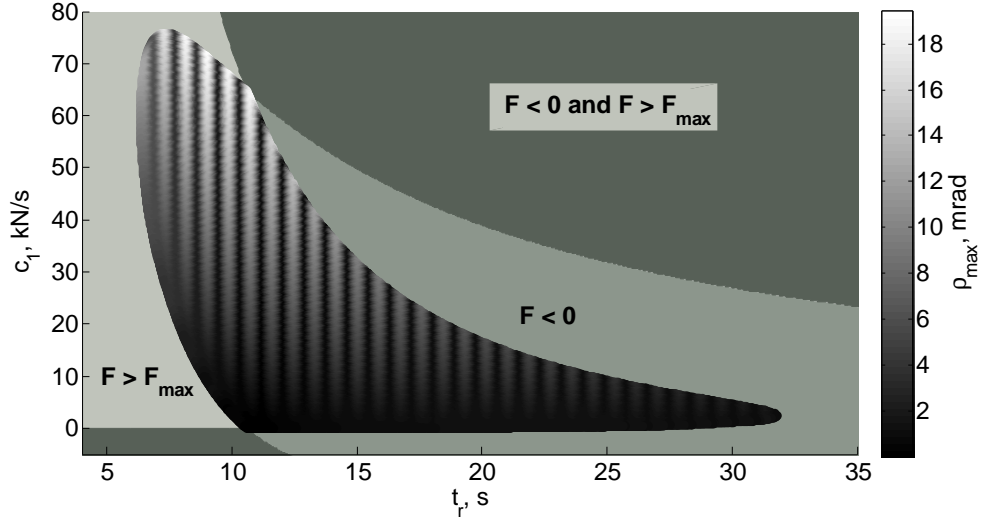
Figure 3.8. Velocity pointing errors for all possible cubic profiles following criteria in Eqs. (3.1) and (3.2) with an initial spin rate of 70 rpm.

constraints in Eq. (3.2). The thrust in the lightest shaded exceeds the maximum value, the thrust in the next lightest area is negative, and the thrust in the darkest areas both exceeds F_{max} and is negative. The coefficient c_1 must remain positive otherwise the force will at some point be negative, representing a non-physical case.

In general, the cubic force profiles that have lower c_1 values have smaller ending pointing errors. For a given c_1 value, the velocity pointing error oscillates as shown by the vertical lines in Fig. 3.8. The minimum velocity pointing error for this search space is 0.020 mrad for a c_1 value of 634 N/s and a ramp-up time of 10.71 seconds. The region with the lowest c_1 values is in the lower left corner of Fig. 3.8. The cubic velocity pointing errors in Fig. 3.7 are horizontal lines in the lower region of Fig. 3.8.

One might wonder if a cycloid, the solution to the classical brachistochrone problem, could also reduce the velocity pointing error. However, it turns out that only one cycloid solution exists and the resulting velocity pointing error of 5.3 mrad is much larger than the linear ramp-up profile's 1.7 mrad velocity pointing error.

Table 3.1 gives the minimum velocity pointing error for each of the heuristic profiles. The heuristic profiles, except for the cycloid, have smaller pointing errors than the linear case which is much less than the 74 mrad ρ_{max} when the engine burns at F_{max} for the entire burn. The two cubic profiles with the smallest pointing error are presented to show the robustness of the cubic profile. The minimum ending pointing error in Table 3.1 is 0.0200 mrad for a cubic force profile which is *essentially zero*. The velocity pointing error for this minimum cubic profile is shown earlier when describing the velocity pointing error behavior in Fig. 3.3.

Table 3.1. Minimum ρ_{max} for all force profiles with $\alpha = 0.25$ deg (4.4 mrad), d = 0.2 cm

Force Profile	t_r, s	ρ_{max}, mrad
Constant	–	74
Linear	10.6	1.70
Cubic ($c_1 = 634$ N/s)	10.71	0.0200*
Cubic ($c_1 = 3950$ N/s)	11.14	0.0202*
Cosine	11.38	0.0701*
Parabolic	11.14	0.0398*
Exponential	11.14	0.0400*
Logarithmic	11.14	0.517
Sine	10.29	0.512
Cycloid	8.20	5.28

* For all practical purposes, $\rho_{max} < 0.1$ mrad can be considered essentially zero.

For the heuristic profiles investigated in this analysis, the radius of the ending circle is, at a minimum, around 0.02 mrad. As a smaller radius is not produced, the best possible solution for the current definition of the velocity pointing error is this radius of 0.02 mrad which is found with one of the cubic profiles. Further decreases could occur if a ramp-down phase was added, but the slight theoretical improvements

would not be practical given the difficulties of implementing a ramp-down phase in an actual thruster. Thus the cubic solution with a velocity pointing error of 0.02 mrad is the best solution found in this analysis.

3.3.3 Velocity Pointing Error for Various Moments of Inertia

Several moments of inertia were considered to determine if the heuristic profiles had improvements over the linear case. Table 3.2 lists the velocity pointing errors for different moments of inertia. All of the profiles resulted in improvements over the linear ramp-up profile. For all of these moments of inertia, the cosine profiles had relatively flat ρ_{max} with respect to t_r, and the exponential curves were more sensitive. When the spacecraft was almost symmetric ($I_x/2$ and $2I_z$), the cosine profiles were a slight improvement over the linear case, and the exponential curves had the lowest minimum. Conversely when the transverse and axial moments of inertia were furthers apart ($2I_x$ and $I_z/2$), the cosine profiles still had low sensitivities to t_r and had the largest improvement over linear profile.

Table 3.2. Minimum ρ_{max} for force profiles with $\alpha = 0.25$ deg (4.4 mrad), d = 0.2 cm, and varying moments of inertia.

Moment of Inertia	Linear* ρ_{max}, mrad	Cosine t_r, s	ρ_{max}, mrad	Exponential t_r, s	ρ_{max}, mrad
I_x, I_z	1.7	11.4	0.070	11.1	0.040
$I_x/2, I_z$	1.4	10.6	1.3	10.4	0.29
$2I_x, I_z$	1.9	10.7	0.011	11.1	0.24
$I_x, I_z/2$	3.6	10.8	0.041	11.1	0.20
$I_x, 2I_z$	0.68	15.0	0.64	9.8	0.13

* The linear profiles all have t_r of 10.6 sec.

3.3.4 Velocity Pointing Error for Various Spin-Rates

Taking an entirely different perspective, if the velocity pointing error of the constant burn (at 74 mrad) *is acceptable*, the spacecraft could spin at a lower rate while using one of these ramp-up thrust profiles. Figure 3.9 shows the available c_1 values and ramp-up times for cubic profiles with a spin rate of 25 rpm and 35 rpm that produce ending velocity pointing errors that are less than or equal to the constant burn of 74 mrad. For a spin rate of 50 rpm (not shown), the entire search space has velocity pointing errors which are less than the constant burn. As the spin rate decreases, the available c_1 values decrease, but when spinning at 25 rpm (about a third of the original spin rate), there is still a range of c_1 and t_r values which give velocity pointing errors that are smaller than the constant burn.

The one parameter profiles (not shown here) have similar increases in their ending velocity pointing errors. Once again, the cosine profiles are close to the cubic profiles with low c_1 values and are relatively flat compared to the other results. The logarithmic, parabolic, and exponential profiles produce velocity pointing errors with even larger sensitivities and similar differences to the cosine profiles as shown in Fig. 3.6. With a cosine ramp-up profile, the minimum spin rate to achieve a 74 mrad velocity pointing error is 11 rpm which is around 15% of the original spin rate.

The minimum velocity pointing errors are reported for the various one parameter profiles and the cubic profiles in Table 3.3. The cycloid and sine values are not included since the minimum ending velocity pointing errors are larger than the other profiles listed. The minimum velocity pointing errors for these various profiles at different spin rates are all smaller than the respective linear velocity pointing error. The cubic profiles have the smallest values of the tested heuristic profiles with minimums that are all less than the linear velocity pointing error of 1.7 mrad at 70 rpm.
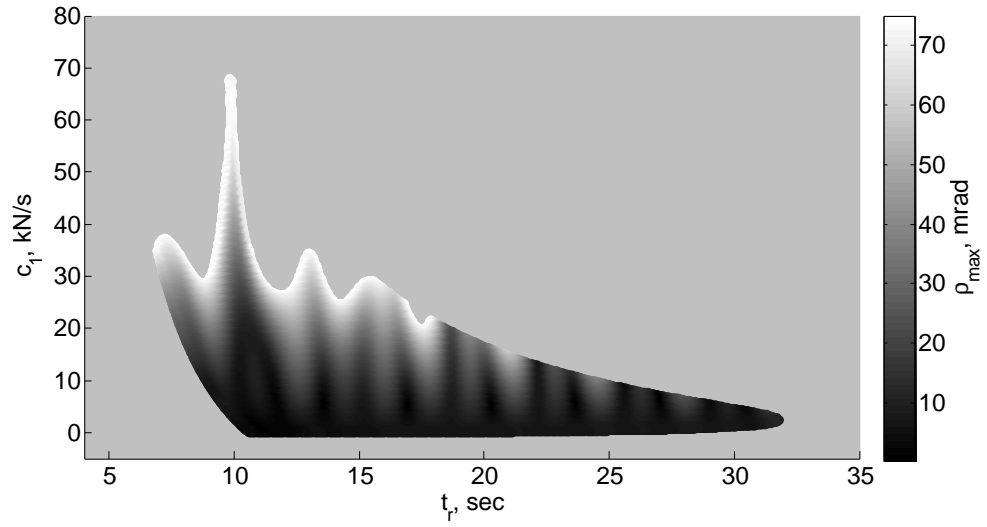
(a) $\omega_{z0} = 35$ rpm
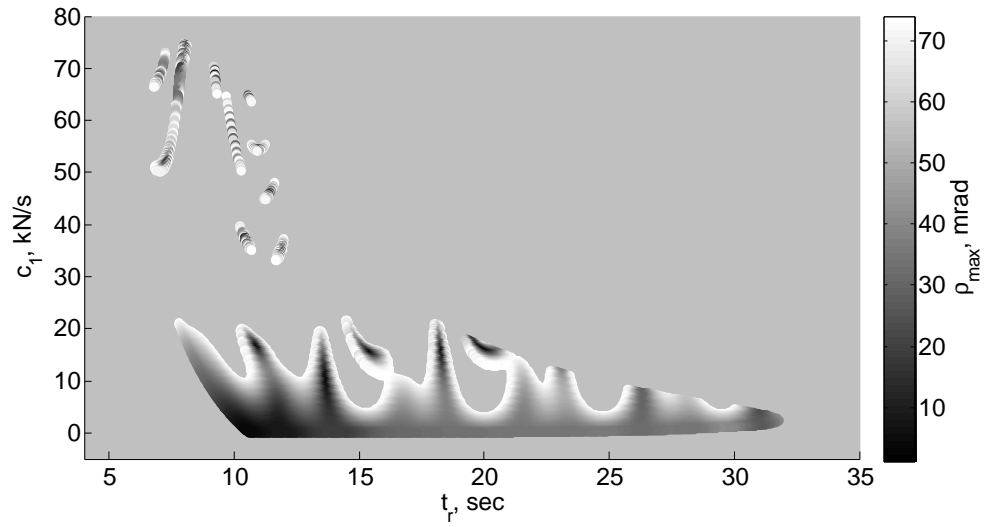
(b) $\omega_{z0} = 25$ rpm

Figure 3.9. Cubic velocity pointing errors that are less than the constant burn value of 74 rpm at 35 and 25 rpm.

Table 3.3. Minimum ρ_{max} for force profiles with $\alpha = 0.25$ deg (4.4 mrad), d = 0.2 cm, and varying spin rates

Profile	50 rpm		35 rpm		25 rpm	
	t_r, s	ρ_{max}, mrad	t_r, s	ρ_{max}, mrad	t_r, s	ρ_{max}, mrad
Linear	10.6	2.22	10.6	7.98	10.6	51.7
Cosine	11.3	0.0663*	11.1	0.346	10.6	2.47
Parabolic	10.8	0.601	11.7	1.77	11.7	16.3
Exponential	10.8	0.602	11.6	1.82	11.7	17.0
Logarithmic	10.8	0.602	27.9	0.431	11.7	18.1
Cubic	11.1	0.0498*	13.5	0.153	10.8	0.347
(Cubic c_1)	(337 N/s)		(4,600 N/s)		(15,900 N/s)	

* For all practical purposes, $\rho_{max} < 0.1$ mrad can be considered essentially zero.

3.3.5 Velocity Pointing Error for Various Thrust Misalignment and Offset

As another test, the thrust misalignment and offset are varied to see if the heuristic profiles still produce smaller velocity pointing errors since in most practical cases, d and α are not known. The results are given in Table 3.4 while using the original spin rate of 70 rpm. The sine and cycloid profiles are excluded because the velocity pointing errors are larger than the remaining profiles.

In Table 3.4, the minimum ρ_{max} values are for the smallest engine offset and misalignment. As the engine offset and misalignment grow, ρ_{max} also grows. In this table, the parabolic, exponential, and logarithmic profiles produce similar ending pointing errors because the corresponding force profiles are close to each other.

If Figs. 3.6 and 3.7 are reproduced for the various d and α values in Table 3.4, the figures will be similar. The ending velocity pointing errors for parabolic, logarithmic, and exponential will still be highly sensitive as in Fig. 3.6, but the oscillations tend

Table 3.4. Minimum ρ_{max} for various d and α

α, deg	d, m	Force Profile	t_r, s	ρ_{max}, mrad
0.25	0.02*	Linear	10.6	1.70
		Cosine	11.4	$0.0701^{\dagger}$
		Parabolic	11.1	$0.0398^{\dagger}$
		Exponential	11.1	$0.0400^{\dagger}$
		Logarithmic	11.1	$0.0395^{\dagger}$
		Cubic ($c_1 = 634$ N/s)	10.7	$0.0200^{\dagger}$
	0.2	Linear	10.6	7.43
		Cosine	11.0	0.355
		Parabolic	12.3	0.458
		Exponential	12.3	0.535
		Logarithmic	12.3	0.413
		Cubic ($c_1 = 6270$ N/s)	15.9	0.349
2.5	0.02	Linear	10.6	4.18
		Cosine	10.9	0.266
		Parabolic	11.1	0.218
		Exponential	11.1	0.218
		Logarithmic	11.1	0.218
		Cubic ($c_1 = 1810$ N/s)	11.1	$0.0767^{\dagger}$
	0.2	Linear	10.6	15.8
		Cosine	10.8	0.656
		Parabolic	12.9	0.887
		Exponential	12.9	0.689
		Logarithmic	12.9	0.945
		Cubic ($c_1 = 440$ N/s)	11.4	0.350

*Table 3.1 information is duplicated here.

† $\rho_{max} < 0.1$ mrad can be considered an effective solution.

to have larger amplitudes and do not approach the same minimum velocity pointing errors. The cosine curve meanwhile will stay relatively flat around the minimum value. The minimum value for the parabolic, exponential, and logarithmic cases will switch between ending on the first (around 11 seconds) or second oscillation (around 12 seconds).

In addition, the cubic force profiles with a thrust offset of 20 cm and a misalignment of 0.25 deg (4.4 mrad) have multiple local minima that are within 0.1 mrad of the reported values. For example, a cubic profile with a ramp-up time of 11.1 seconds has a ending pointing error that is within 0.001 mrad of the minimum reported in Table 3.4.

For these offset and misalignment changes, the linear profiles have the largest ρ_{max} values. For small thrust offsets, the parabolic, exponential, and logarithmic profiles have almost identical results, and the cosine profiles have the second largest minimum values. For large thrust offsets, the parabolic, exponential, and logarithmic profiles still have close results within 0.3 mrad, but the cosine profiles have the second smallest minimum values. The cubic profiles produce the minimum velocity pointing errors for these thrust offsets and misalignments.

The order-of-magnitude change in α has less of an effect on the velocity pointing error than an order-of-magnitude change in d due to Eq. (3.15) where the torque is dependent on d and the cosine or sine of α. Furthermore, using a ramp-up time of around 11 seconds will produce minimum values for cubic profiles and the less sensitive cosine profiles.

3.4   Practical Applications

One might wonder if these heuristic profiles are physically realizable with the current engine technology for solid, liquid, or hybrid engines. Two problems exist: throttling the engine to a very low thrust level, called deep throttling, and starting the engine at this very low thrust.

While nontrivial, the propellant grain geometry or the choice of fuel and oxidizers in a solid rocket can be changed to model various profiles [68]. Solid rockets can be throttled [71], but it is difficult to deeply throttle solid rockets due to the coupling between the propellant gasification rate and the chamber pressure [72]. Furthermore, thrust profiles are easier to design with liquid propellant rocket engines which also have the additional benefit of multiple burns [73].

Numerous throtteable liquid propellant rockets have been tested [73] including a few deep throttling rockets which can throttle to less than 40% thrust [74]. One of the most famous throttling engines is the Lunar Module Descent Engine which had a 10-to-1 throttling capability and could achieve a cold start at 10% thrust [74]. Other deep throttling engines include, the RL10A-1 which was throttled to below 10% [75], the RD-0120 which was throttled to 25% [76], the Space Shuttle main engine which was throttled down to 17% [77], and the TR202 which was throttled to 7.5% [78]. In addition, the Common Extensible Cryogenic Engine can be throttled down to 5.9% thrust with a cold start at 10% [79]. To prevent flame out (when the flame in the combustion chamber is extinguished), the liquid propellant engines need to start at a non-zero thrust level.

Hybrid rockets, while not as efficient as liquid rockets, are another option for throttling rockets. Hybrid rockets have been throttled down to 10% of thrust and then throttled up from 10% to full power [80]. One of the deepest throttling engines is a hybrid rocket which has a turndown ratio of 67:1 or 1.5% of thrust [72].

Current throttleable engines are primarily tested by throttling down for applications (such as landing) which do not require an engine to throttle up. However, it can be argued that the same technology could be used to throttle up an engine as shown by Austen, et al. [80]. While current off-the-shelf engine technology may be unable to perform these heuristic profiles starting at zero thrust, deep throttling engines are close to implementing this passive control scheme.

To demonstrate that a ramp-up scheme can reduce velocity pointing errors even when not starting at zero thrust, the simulation is run again where the initial thrust

value is now a percentage of F_{max}, given by β. The total impulse for the ramp-up phase remains the same as when starting at zero thrust to fairly compare the simulations. Table 3.5 gives the resulting minimum ending velocity pointing errors for the various heuristic profiles. The velocity pointing errors increase with increasing initial force, but are all much less than the 74 mrad from the constant thrust case.

In Table 3.5, the cubic profile has the minimum velocity pointing error for when the initial thrust is at or below 1% F_{max}. For the larger initial thrust values, the logarithmic profile results in a smaller velocity pointing error. To achieve these minimum velocity pointing errors for the logarithmic profiles, the solutions are highly sensitive. For example, less than a half a second after the 5% initial F_{max} logarithmic minimum ρ_{max}, the velocity pointing error is above 7 mrad. This difference in velocity pointing error increases with increasing initial F_{max}. Less dramatic sensitivities occur for the cubic, parabolic, and exponential profiles.

For the cubic values with initial forces (i.e. β values) at 5%, 10%, and 20% F_{max}, the minimum values occur at c_1 values which are on the bounds of the search space where a larger c_1 value would result in a partially negative thrust profile. Unlike the previous simulations, the search space changes with the initial thrust value. Due to the minimum ρ_{max} being on the bounds, the cases with β larger than 1% do not have a smaller minima than the logarithmic case. Once again to achieve these low ρ_{max} values with a higher initial thrust level, the velocity pointing error is highly sensitive. To decrease the sensitivity, a lower c_1 value should be used which gives results that are slightly less than the cosine ρ_{max} values.

Table 3.5 only shows the minimum ρ_{max}, but the profiles, specifically the cubic profiles, have multiple local minima that are within 10% of the reported value. With the exception of an initial thrust of 5% F_{max}, the cubic profiles have multiple minima within 5% of the reported value. These ρ_{max} may not be the minimum values but are still smaller than the other profiles except the logarithmic profiles as well as the exponential profile in the 10% F_{max} case. The cubic cases with various β all have a local minimum at 12.7 seconds. The cases with smaller sensitivities but higher ρ_{max}

Table 3.5. Minimum ρ_{max} for varying initial force

Profile	20% F_{max}		10% F_{max}		5% F_{max}		1% F_{max}		0% F_{max}	
	t_r, s	ρ_{max}, mrad	t_r, s	ρ_{max}, mrad	t_r, s	ρ_{max}, mrad	t_r, s	ρ_{max}, mrad	t_r, s	ρ_{max}, mrad
Linear	8.33	17.2	9.18	9.64	10.1	3.54	10.5	1.93	10.6	1.70
Sine	8.40	16.1	9.24	7.84	10.1	3.61	10.2	0.705	10.3	0.512
Exponential	19.5	12.3	39.2	2.29	36.6	1.64	11.9	0.0677	11.1	0.0400
Parabolic	10.9	15.4	12.6	7.11	14.4	2.98	11.9	0.0843	11.1	0.0398
Cosine	10.9	15.6	12.6	7.24	14.4	3.00	13.5	0.0829	11.4	0.0701
Logarithmic	16.8	2.29	18.6	0.380	17.6	0.0698	11.9	0.0321	11.1	0.0395
Cubic	11.0	10.3	12.7	3.71	15.3	0.739	12.7	0.0200	10.7	0.0200
(Cubic c_1)	(50,200 N/s)		(40,200 N/s)		(28,400 N/s)		(1,420 N/s)		(634 N/s)	

values also have local minima around 12.7 seconds. If the initial thrust level is not precisely known, this ramp-up time of 12.7 seconds would be a practical ramp-up time to use.

3.5   Summary

Ideally, the ramp-up profile which minimizes the velocity pointing error would be found by implicit optimization. However, due to the complicated nature of the problem, no solution has been found. Instead heuristic solutions for ramp-up profiles have been found which lead to highly effective solutions. The sine profiles tested here present an order-of-magnitude velocity pointing error improvement over the linear ramp-up profile, while the cosine, parabolic, exponential, logarithmic, and cubic profiles reduce the velocity pointing error further, by up to two orders of magnitude. These profiles have more than a three order-of-magnitude improvement compared to the typical constant burn profile.

With a small thrust misalignment and offset, the velocity pointing error for cosine, parabolic, exponential, logarithmic, and cubic profiles is essentially zero. These profiles are an improvement over the linear ramp-up profile for various moments of inertia, spin-rates, and thrust offset and misalignment. In the simulation, a ramp-up time around 11 seconds for different engine misalignments and offsets results in velocity pointing errors which are either the minimum value or very close to the minimum.

While current engine technology may not be able to duplicate ramp-up profiles starting at zero, ramp-up profiles, especially the cubic profile, decrease the velocity pointing error over the typical constant burn even with an initial non-zero thrust.

4. Method to Maintain Artificial Gravity during Transfer Maneuvers for Tethered Spacecraft*

4.1 Background

One of the most recognizable spacecraft with artificial gravity is a large toroidal space station similar to the one in *2001: A Space Odyssey*. With a toroidal spacecraft such as the one in Fig. 4.1(a), the engines thrust through the center of mass along the spin axis to preserve artificial gravity. However, to produce artificial gravity at a practical spin rate, the spacecraft must have a large radius can lead to prohibitive launch masses.

(a) Cabin provides spin length.   (b) Tether or truss provides spin length.
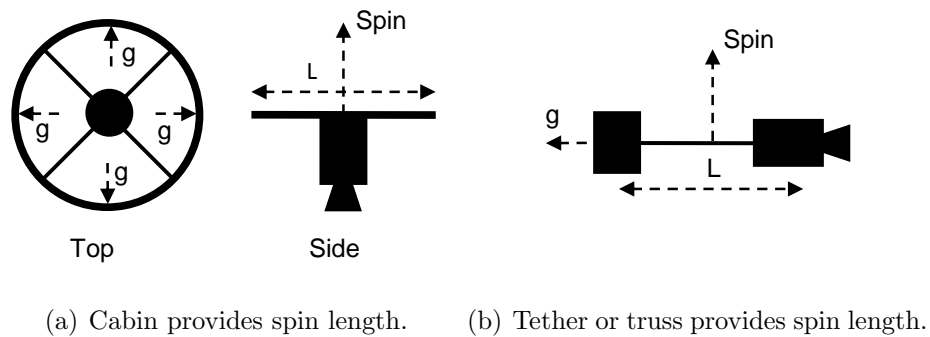
Figure 4.1. Potential spacecraft configurations to provide artificial gravity. Adapted with permission from Landau [64].

To minimize mass, the crew cabin could be tethered to the propellant tanks and spun up to produce artificial gravity as in Fig. 4.1(b). Instead of propellant tanks, a riskier counterweight such as a power system, lander, or consumables could be

---

*This chapter resulted from a collaboration with Dr. Damon Landau at JPL who first published this control method [64]. A journal article with Dr. Damon Landau on the subject is currently under preparation.

used, but this counterweight would separate the crew from potential life supporting systems. Alternatively, the crew cabin and propulsion system could reside on one side of the tether with a counterweight of spent rocket engines. For any of these scenarios, the required additional mass to produce artificial gravity is the relatively low-mass tether.

Two scenarios exist to thrust through the center of mass of a tethered spacecraft. As depicted in Fig. 4.2(a), the spacecraft can spin down and reel in the tether, but the resulting engine burn would decrease or potentially reverse the gravity direction. The tether in Fig. 4.2(a) could be replaced with a truss but the spacecraft would still be required to despin and lose artificial gravity during a manuever. The other case occurs in Fig. 4.2(b) where the tether length is constantly adjusted during the burn so that the center of mass remains fixed with the engine [41, 56–59].

(a) Non-spinning spacecraft.　　　　(b) Spacecraft with moving thrust.
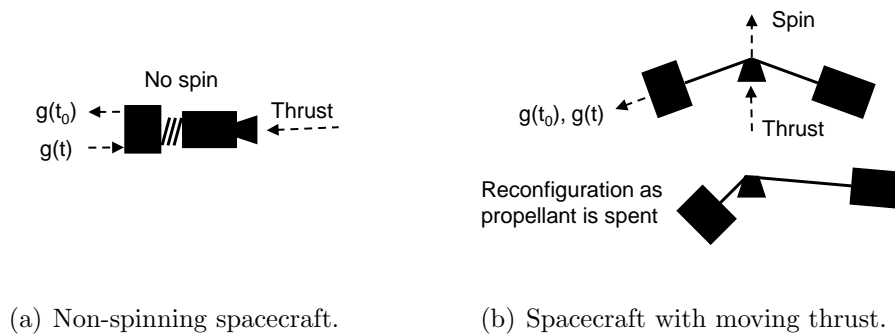
Figure 4.2. Issues with thrusting through the center of mass for tethered systems. When Fig. 4.2(a) despins and thrusts, the gravitational acceleration reverses direction from $g(t_0)$ to $g(t)$. The gravity direction in Fig. 4.2(b) remains the same at the cost of moving the thruster to the center of mass. Adapted with permission from Landau [64].

To provide artificial gravity for the entire mission with a fixed tether configuration, consider Fig. 4.3 where the thrust is no longer aligned with the center of mass. In this scenario, the crew habitat is pulled along by the thrusters at an angle to the spin axis. The resulting moment from the offset thrust cancels out the moment caused by the product of inertia, and the angular momentum circles the spin axis. During
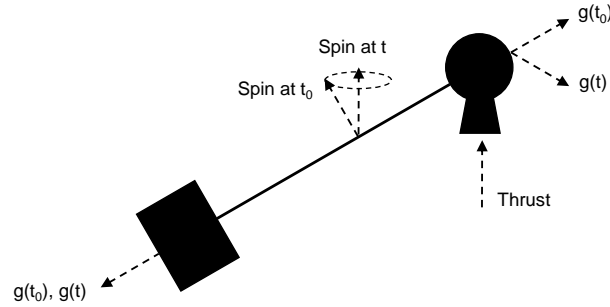
Figure 4.3. Spacecraft configuration which keeps the gravity direction and system configuration the same while thrusting. Adapted with permission from Landau [64].

maneuvers, the orientation is fixed relative to the spin axis by adjusting the thrust level or slightly rolling the thrust along the tether axis, allowing the entire burn to be in the desired direction.

The spacecraft configuration in Fig. 4.3 is more desirable than the design options in Fig. 4.2 since the fixed tether length and thruster position are more robust and less expensive to manufacture. Furthermore, the design in Fig. 4.3 does not change the gravity direction during maneuvers. This chapter expands work by Landau [64] to derive the dynamics and control for such a tethered spacecraft with various mass assumptions and to apply the control scheme to a round-trip mission to Mars. For completeness, sections 4.2.5 and 4.3 are included from Landau's paper [64], but the remaining sections are original work.

4.2 Dynamics of Tethered Spacecraft with Offset Thruster

A major transfer maneuver such as insertion from Earth orbit to an interplanetary orbit with a chemical system may use more than half of a spacecraft's propellant over several minutes. Not only does the spacecraft undergo large accelerations, but the spacecraft's orientation will dramatically change due to the large torques from high thrust and the large changes in the center-of-mass location. A low-thrust system

produces the same orientation changes but over a much longer period of time making the maneuver more controllable. While the governing equations of motion for the system will remain the same for either propulsion system, the simulation in the next section assumes a chemical system for a shorter simulation time.

The orientation errors from such a large burn translate into additional propellant costs and the potential for a lost mission. To reduce these errors, it is necessary that the desired ΔV direction be controlled either through a change in the thrust level or a small rotation of the thrust along the tether axis.

The orientation of the spacecraft is defined in Fig. 4.4 with a body-fixed 3-2 rotation sequence. For this scenario, the propulsion and habitation systems are on opposite sides of the tether, but the resulting equations also hold for the case where the habitation module and the propulsion system are attached to a counterweight, possibly of spent rocket bodies.
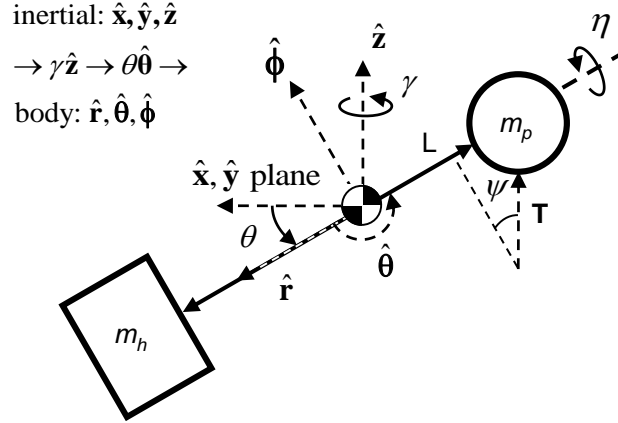
Figure 4.4. Spacecraft orientation angles, a body-fixed 3-2 rotation sequence, for a spacecraft with total tether length L. Adapted with permission from Landau [64].

In this derivation, the propulsion system and crew habitat are assumed to be point masses, so there is no dynamical significance to a rotation about the $\hat{\mathbf{r}}$ axis. Furthermore, the tether is modeled as massless and inelastic. To keep the thrust direction along $\hat{\mathbf{z}}$, the tether offset from $\hat{\mathbf{z}}$, namely θ, is controlled to be along the

thrust offset from the tether, ψ, so that when $\theta = \psi$, the thrust is in the direction of $\hat{\mathbf{z}}$.

The angular velocity for the given rotation sequence is

$$^x\overline{\omega}^r = \dot{\gamma}\hat{\mathbf{z}} + \dot{\theta}\hat{\boldsymbol{\theta}} \tag{4.1}$$

where γ is the angle of rotation about $\hat{\mathbf{z}}$. Rotating the $\hat{\mathbf{z}}$ component in Eq. (4.1) into the body frame results in

$$^x\overline{\omega}^r = -\dot{\gamma}\sin\theta\hat{\mathbf{r}} + \dot{\theta}\hat{\boldsymbol{\theta}} + \dot{\gamma}\cos\theta\hat{\boldsymbol{\phi}} \tag{4.2}$$

4.2.1 Constant Mass

The simplest case occurs when the spacecraft has a fixed mass and is forced to rotate at a constant rate, $\dot{\gamma}$, at a fixed angle, $\theta = \psi$. To maintain the spin rate and angle, a transverse torque along $\hat{\boldsymbol{\theta}}$ is required. This scenario is analogous to a ceiling fan rotating at a fixed angle. (See Greenwood [66] where a thin rod is forced to rotate at a constant rate around an inertially-fixed, nonprincipal axis.)

One approach to solve for the required transverse torque is to derive the results in a rotated body-fixed coordinate frame where the body-fixed coordinate frame $(\hat{\mathbf{r}}-\hat{\boldsymbol{\theta}}-\hat{\boldsymbol{\phi}})$ in Fig. 4.4 is rotated such that $\hat{\boldsymbol{\phi}}$ is aligned with $\hat{\mathbf{z}}$. The principal moments of inertia in the body-fixed coordinate frame $\hat{\mathbf{r}} - \hat{\boldsymbol{\theta}} - \hat{\boldsymbol{\phi}}$ shown in Fig. 4.4 are

$$\begin{aligned} I_r &= 0 \\ I_\theta = I_\phi &= \frac{m_p m_h L^2}{m} \end{aligned} \tag{4.3}$$

where L is the total length of the tether (from the crew habitat to the propulsion module), m_p is the mass of the propulsion system, and m is the total mass of the

system (the habitat and propulsion system). The moments and products of inertia in the rotated body-fixed frame are then found by

$$
\mathbf{I} = \begin{bmatrix} \cos\theta & 0 & \sin\theta \\ 0 & 1 & 0 \\ -\sin\theta & 0 & \cos\theta \end{bmatrix} \begin{bmatrix} I_r & 0 & 0 \\ 0 & I_\theta & 0 \\ 0 & 0 & I_\phi \end{bmatrix} \begin{bmatrix} \cos\theta & 0 & -\sin\theta \\ 0 & 1 & 0 \\ \sin\theta & 0 & \cos\theta \end{bmatrix}
$$
$$
= \frac{m_p m_h L^2}{m} \begin{bmatrix} \sin^2\theta & 0 & \sin\theta\cos\theta \\ 0 & 1 & 0 \\ \sin\theta\cos\theta & 0 & \cos^2\theta \end{bmatrix}
$$
(4.4)

Using the inertia values in Eq. (4.4) and the assumption that the angular velocities do not change with time, the general rotational equations [66] become

$$
M_x = I_{xz}\omega_x\omega_y + (I_{zz} - I_{yy})\,\omega_y\omega_z
$$
$$
M_y = (I_{xx} - I_{zz})\,\omega_x\omega_z + I_{xz}\left(\omega_z^2 - \omega_x^2\right)
$$
(4.5)
$$
M_z = -I_{xz}\omega_y\omega_z + (I_{yy} - I_{xx})\,\omega_x\omega_y
$$

Since the only force is from the spacecraft's thruster in the $\hat{\mathbf{z}}$ direction, the only torque present is in the $\hat{\mathbf{y}}$ direction (aligned with $\hat{\boldsymbol{\theta}}$). Furthermore, the spacecraft is forced to rotate such that ω_x and ω_y are zero. These assumptions cause the first and third equations in Eq. (4.5) to drop out leaving

$$
M_y = I_{xz}\omega_z^2 = \frac{m_p m_h L^2}{m}\dot{\gamma}^2 \sin\theta\cos\theta
$$
(4.6)

The torque caused by the spacecraft's thrust is

$$
M_y = \frac{m_h L}{m} T \cos\psi
$$
(4.7)

Since θ equals ψ, Eq. (4.7) can be substituted into Eq. (4.6) resulting in

$$
T = \dot{\gamma}^2 m_p L \sin\psi
$$
(4.8)

In this case, $\dot{\gamma}$, m_p, and T are constant. The thrust cannot use the typical thruster modeled $(-\dot{m}gI_{sp})$ since the mass is constant. Even if $\dot{m}$ is very small, the corresponding thrust and the spin rate would also be relatively small. However, the thrust from a solar sail (based on distance from the Sun, solar flux, sail area, sail reflection, and sail tilt [81]) could be used to model a constant mass spacecraft with thrust.

4.2.2 Constant Thrust

Building on the previous model, now consider the case when the mass changes linearly with time. Here the mass of the propulsion system, m_p, is variable with a mass flow rate, $\dot{m}$, which is negative as propellant is expelled from m_p. The mass of the habitation system is assumed to remain constant. In this case, the thrust is given by

$$T = -\dot{m}gI_{sp} \tag{4.9}$$

where $\dot{m}$ is constant and the mass is modeled as

$$m = m_0 + \dot{m}t \tag{4.10}$$

The principal moments of inertia are now time varying but of the same form as Eq. (4.3) with

$$\dot{I}_r = 0$$
$$\dot{I}_\theta = \dot{I}_\phi = \frac{\dot{m}m_h^2 L^2}{m^2} \tag{4.11}$$

Euler's equations of motion for a system with changing mass are [69]

$$M_r = I_r\dot{\omega}_r + \dot{I}_r\omega_r + (I_\phi - I_\theta)\,\omega_\theta\omega_\phi$$
$$M_\theta = I_\theta\dot{\omega}_\theta + \dot{I}_\theta\omega_\theta + (I_r - I_\phi)\,\omega_r\omega_\phi \tag{4.12}$$
$$M_\phi = I_\phi\dot{\omega}_\phi + \dot{I}_\phi\omega_\phi + (I_\theta - I_r)\,\omega_r\omega_\theta$$

The effect of jet damping cancels out the changing moments of inertia terms since this model assumes that habitation module and propulsion system are both point masses [69]. Then Eq. (4.12) becomes

$$M_r = I_r\dot{\omega}_r + (I_\phi - I_\theta)\,\omega_\theta\omega_\phi$$
$$M_\theta = I_\theta\dot{\omega}_\theta + (I_r - I_\phi)\,\omega_r\omega_\phi \tag{4.13}$$
$$M_\phi = I_\phi\dot{\omega}_\phi + (I_\theta - I_r)\,\omega_r\omega_\theta$$

Substituting Eq. (4.3) into Eq. (4.13) results in

$$M_r = 0$$
$$M_\theta = I\dot{\omega}_\theta - I\omega_r\omega_\phi \tag{4.14}$$
$$M_\phi = I\dot{\omega}_\phi + I\omega_r\omega_\theta$$

where $I = I_\theta = I_\phi$.

Recall the angular velocity components from Eq. (4.2) as

$$\omega_r = -\dot{\gamma}\sin\theta$$
$$\omega_\theta = \dot{\theta} \tag{4.15}$$
$$\omega_\phi = \dot{\gamma}\cos\theta$$

Differentiating these components results in

$$\dot{\omega}_r = -\ddot{\gamma}\sin\theta - \dot{\gamma}\dot{\theta}\cos\theta$$
$$\dot{\omega}_\theta = \ddot{\theta} \tag{4.16}$$
$$\dot{\omega}_\phi = \ddot{\gamma}\cos\theta - \dot{\gamma}\dot{\theta}\sin\theta$$

Substituting Eqs. (4.15) and (4.16) into Eq. (4.14) gives

$$M_\theta = I\ddot{\theta} + I\dot{\gamma}^2\sin\theta\cos\theta$$
$$M_\phi = I\ddot{\gamma}\cos\theta - 2I\dot{\gamma}\dot{\theta}\sin\theta \tag{4.17}$$

The goal of this derivation is to find the thrust and mass history which results in θ equal to the constant body-fixed thrust direction, ψ. Assuming θ is constant and equal to ψ, Eq. (4.17) becomes

$$M_\theta = I\dot{\gamma}^2\sin\psi\cos\psi$$
$$M_\phi = I\ddot{\gamma}\cos\psi \tag{4.18}$$

When the thrust is in the $\hat{\mathbf{r}} - \hat{\boldsymbol{\phi}}$ plane as shown in Fig. 4.4, the torque is

$$\mathbf{M}^{CM} = \mathbf{r}^{CMp} \times \mathbf{T} = -\frac{m_h L}{m}\hat{\mathbf{r}} \times \left(-T\sin\psi\hat{\mathbf{r}} + T\cos\psi\hat{\boldsymbol{\phi}}\right) = \frac{m_h L}{m}T\cos\psi\hat{\boldsymbol{\theta}} \quad (4.19)$$

Substituting Eqs. (4.3) and (4.19) into Eq. (4.18) and reducing the equations results in

$$T = m_p L\dot{\gamma}^2\sin\psi$$
$$\ddot{\gamma} = 0 \tag{4.20}$$

where the first equation is the same control law as Eq. (4.8). The control law shows how the changing mass of the propulsion system, m_p, affects the spacecraft's orientation. When the spacecraft is burning propellant, the thrust must decrease or the

spin rate, $\dot{\gamma}$, must increase to keep the spacecraft configuration of $\theta = \psi$. To maintain this orientation, the tether length or the thruster angle, ψ, could also be modified but would then require a more complex reconfigurable spacecraft.

For this particular derivation, T, $\dot{\gamma}$, L, and ψ are constant and therefore force the time-varying m_p to also be constant, a contradiction. With a constant planar thrust, there is no means to control the system, so the control law breaks down.

To overcome this contradiction, a slight roll, η along $\hat{\mathbf{r}}$, would point a portion of the thrust along $\hat{\boldsymbol{\theta}}$ resulting in a control force and allowing M_ϕ to be nonzero. For a roll along $\hat{\mathbf{r}}$, the thrust is

$$\mathbf{T}_\eta = -T\sin\psi\hat{\mathbf{r}} - T\cos\psi\sin\eta\hat{\boldsymbol{\theta}} + T\cos\psi\cos\eta\hat{\boldsymbol{\phi}} \tag{4.21}$$

where η is the roll along $\hat{\mathbf{r}}$. The torque is then

$$\mathbf{M}^{CM} = \frac{m_h L}{m}T\cos\eta\cos\psi\hat{\boldsymbol{\theta}} + \frac{m_h L}{m}T\sin\eta\cos\psi\hat{\boldsymbol{\phi}} \tag{4.22}$$

To maximize the amount of thrust in the desired direction, η is kept small. Then $\cos\eta$ is assumed to be unity so that

$$\begin{aligned} M_\theta &= \frac{m_h L}{m}T\cos\psi \\ M_\phi &= \frac{m_h L}{m}T\sin\eta\cos\psi \end{aligned} \tag{4.23}$$

Equation (4.18) becomes

$$\begin{aligned} T &= m_p L\dot{\gamma}^2\sin\psi \\ \sin\eta &= m_p L\ddot{\gamma}/T \end{aligned} \tag{4.24}$$

where the first equation is once again the same control law as Eq. (4.8).

Since the thrust and mass are known, the first equation in Eq. (4.24) gives the spin rate where

$$\dot{\gamma}^2 = \frac{T}{m_p L\sin\psi} \tag{4.25}$$

Differentiating Eq.(4.25) results in

$$\ddot{\gamma} = -\frac{T\dot{m}}{2m_p^2 L\dot{\gamma}\sin\psi} \tag{4.26}$$

After substituting for $\dot{\gamma}$ and $\ddot{\gamma}$, the equation for η in Eq. (4.24) becomes

$$\sin \eta = -\frac{\dot{m}}{2}\sqrt{\frac{L}{Tm_p \sin \psi}} \qquad (4.27)$$

The system is now controlled by η determined by Eq. (4.27) with a spin rate governed by Eq. (4.25). Since $\dot{m}$ is likely to be much smaller than m_p and the thrust is a function of $\dot{m}$, η will remain small. When initializing the maneuver, $\dot{m}$ is chosen such that Eq. (4.25) holds for the current spin rate, and then the burn time is found based on the maneuver's propellant mass.

4.2.3 Planar Non-Constant Thrust

A more complicated scheme occurs when the thrust is no longer constant (so that $\dot{m}$ can vary) but is constrained in the $\hat{\mathbf{r}} - \hat{\boldsymbol{\phi}}$ plane. Then Euler's equations of motion are the same as Eq. (4.17) with the torque given in Eq. (4.19). Assuming θ is constant, these equations reduce into

$$T = m_p L \dot{\gamma}^2 \sin \psi$$
$$\ddot{\gamma} = 0 \qquad (4.28)$$

Once again $\dot{\gamma}$ is constant, but since the thrust is not constant, it can vary according to the first equation in Eq. (4.28). Using $T = -\dot{m}gI_{sp}$ and $\dot{\gamma} = \dot{\gamma}_0$, the first equation in Eq. (4.28) becomes

$$\frac{\dot{m}}{m_p} = -\frac{L}{gI_{sp}}\dot{\gamma}_0^2 \sin \psi \qquad (4.29)$$

To find the mass time history, Eq. (4.29) is integrated to obtain

$$m_p = m_{p0} \exp\left(-\frac{L\dot{\gamma}_0^2 \sin \psi}{gI_{sp}}t\right) \qquad (4.30)$$

The mass is then substituted into Eq. (4.29) to find the required $\dot{m}$ (and corresponding thrust) which results in a constant θ.

4.2.4 Non-Planar Non-Constant Thrust

Instead of a planar thrust, consider a spacecraft with a non-constant and non-planar thrust. Using Eq. (4.21) as the new thrust, the torques are the same as in Eq. (4.23). Assuming θ is constant, Eq. (4.17) reduces into

$$T = m_p L \dot{\gamma}^2 \sin \psi$$

$$\sin \eta = m_p L \ddot{\gamma}/T$$

(4.31)

where $T = -\dot{m} g I_{sp}$ and $\dot{m}$ is time varying. In this case, $\dot{\gamma}$ is no longer constant and varies according to

$$\ddot{\gamma} = -\frac{\ddot{m} g I_{sp} + \dot{\gamma}^2 \dot{m} L \sin \psi}{2 \dot{\gamma} m_p L \sin \psi}$$

(4.32)

which is found by differentiating the first equation in Eq. (4.31). Substituting Eq. (4.32) into the second equation in Eq. (4.31) gives

$$\sin \eta = \frac{\ddot{m} g I_{sp} + \dot{\gamma}^2 \dot{m} L \sin \psi}{2 \dot{m} g I_{sp} \dot{\gamma} \sin \psi}$$

(4.33)

If $\dot{m}$ is constant, Eq. (4.33) becomes Eq. (4.27). The spin rate is found from the first equation in Eq. (4.31) where

$$\dot{\gamma}^2 = -\frac{\dot{m} g I_{sp}}{m_p L \sin \psi}$$

(4.34)

which is identical to Eq. (4.8). After choosing the desired mass history (and consequently the thrust history), the required spin rate follows Eq. (4.34) which is then used to solve for the necessary η in Eq. (4.33) to control θ.

4.2.5 Newtonian Analysis of Non-Constant Thrust

Alternatively instead of deriving the control law from Euler's equations of motion, one could start with the center of mass as Landau did in Ref. [64]. The derivation is included here for completeness.

When the thrust is assumed to be non-constant, the resulting solutions match Eqs. (4.33) and (4.34). The spacecraft is still assumed to have a fixed configuration where L and ψ are constant and a fixed habitation system mass.

The position of the habitat with respect to the center of mass is

$$\mathbf{r}_h - \mathbf{r}_{cm} = \frac{Lm_p}{m}\hat{\mathbf{r}} \tag{4.35}$$

Taking into account the angular velocity in Eq. (4.2), the velocity and acceleration of the habitat with respect to the center of mass are

$$\mathbf{v}_h - \mathbf{v}_{cm} = \frac{L\dot{m}m_h}{m^2}\hat{\mathbf{r}} + \frac{Lm_p}{m}\dot{\gamma}\cos\theta\hat{\boldsymbol{\theta}} - \frac{Lm_p}{m}\dot{\theta}\hat{\boldsymbol{\phi}} \tag{4.36}$$

$$\begin{aligned}
\mathbf{a}_h - \mathbf{a}_{cm} &= \left[\frac{-2L\dot{m}^2 m_h}{m^3} + \frac{L\ddot{m}m_h}{m^2} - \frac{Lm_p}{m}\left(\dot{\gamma}^2\cos^2\theta + \dot{\theta}^2\right)\right]\hat{\mathbf{r}} \\
&+ \left[\frac{2L\dot{m}m_h}{m^2}\dot{\gamma}\cos\theta + \frac{Lm_p}{m}\left(\ddot{\gamma}\cos\theta - 2\dot{\gamma}\dot{\theta}\sin\theta\right)\right]\hat{\boldsymbol{\theta}} \\
&+ \left[-\frac{2L\dot{m}m_h}{m^2}\dot{\theta} - \frac{Lm_p}{m}\left(\dot{\gamma}^2\cos\theta\sin\theta + \ddot{\theta}\right)\right]\hat{\boldsymbol{\phi}}
\end{aligned} \tag{4.37}$$

Similarly, the position, velocity, and acceleration of the propulsion system with respect to the center of mass are

$$\mathbf{r}_p - \mathbf{r}_{cm} = -\frac{Lm_h}{m}\hat{\mathbf{r}} \tag{4.38}$$

$$\mathbf{v}_p - \mathbf{v}_{cm} = \frac{L\dot{m}m_h}{m^2}\hat{\mathbf{r}} - \frac{Lm_h}{m}\dot{\gamma}\cos\theta\hat{\boldsymbol{\theta}} + \frac{Lm_h}{m}\dot{\theta}\hat{\boldsymbol{\phi}} \tag{4.39}$$

$$\begin{aligned}
\mathbf{a}_p - \mathbf{a}_{cm} &= \left[-\frac{2L\dot{m}^2 m_h}{m^3} + \frac{L\ddot{m}m_h}{m^2} + \frac{Lm_h}{m}\left(\dot{\gamma}^2\cos^2\theta + \dot{\theta}^2\right)\right]\hat{\mathbf{r}} \\
&+ \left[\frac{2L\dot{m}m_h}{m^2}\dot{\gamma}\cos\theta - \frac{Lm_h}{m}\left(\ddot{\gamma}\cos\theta - 2\dot{\gamma}\dot{\theta}\sin\theta\right)\right]\hat{\boldsymbol{\theta}} \\
&+ \left[-\frac{2L\dot{m}m_h}{m^2}\dot{\theta} + \frac{Lm_h}{m}\left(\dot{\gamma}^2\cos\theta\sin\theta + \ddot{\theta}\right)\right]\hat{\boldsymbol{\phi}}
\end{aligned} \tag{4.40}$$

By the definition of the center of mass, the position of the center of mass is

$$\mathbf{r}_{cm} = \left(m_h\mathbf{r}_h + m_p\mathbf{r}_p\right)/m \tag{4.41}$$

The velocity and acceleration of the center of mass are found by differentiating Eq. (4.41) which yields

$$\mathbf{v}_{cm} = \left[m_h\mathbf{v}_h + m_p\mathbf{v}_p + \dot{m}\left(\mathbf{r}_p - \mathbf{r}_{cm}\right)\right]/m \tag{4.42}$$

$$\mathbf{a}_{cm} = \left[m_h\mathbf{a}_h + m_p\mathbf{a}_p + 2\dot{m}\left(\mathbf{v}_p - \mathbf{v}_{cm}\right) + \ddot{m}\left(\mathbf{r}_p - \mathbf{r}_{cm}\right)\right]/m \tag{4.43}$$

For a planar thrust,

$$\mathbf{T} = -T \sin \psi \hat{\mathbf{r}} + T \cos \psi \hat{\boldsymbol{\phi}} \tag{4.44}$$

For a more general derivation, the system also includes control forces in the $\hat{\boldsymbol{\theta}}$ or $\hat{\boldsymbol{\phi}}$ direction applied at either the habitat ($R_{\theta h}$ and $R_{\phi h}$) or propulsion system the ($R_{\theta p}$ and $R_{\phi p}$) so that

$$\mathbf{R} = \left(R_{\theta h} + R_{\theta p} \right) \hat{\boldsymbol{\theta}} + \left(R_{\phi h} + R_{\phi p} \right) \hat{\boldsymbol{\phi}} \tag{4.45}$$

Since the system has time-varying mass, Newton's second law must be carefully applied. For time-varying mass, Newton's second law is

$$\mathbf{F} + \mathbf{v}_{rel} \frac{dm}{dt} = m \frac{d\mathbf{v}}{dt} \tag{4.46}$$

where $\mathbf{F}$ are the external forces, $\mathbf{v}_{rel}$ is the velocity of the departing mass with respect to the center of mass, and $\mathbf{v}$ is the system's velocity. However, as revealed by Belknap, the effect of jet damping cancels out the effects from the decreasing spacecraft inertia [82]. Then mass that leaves the spacecraft with zero relative velocity does not change the angular velocity but affects the translational motion according to Eq. (4.43). Any mass that departs with non-zero relative velocity is modeled as thrust or

$$T = -\dot{m} g I_{sp} \tag{4.47}$$

Then $\dot{m} \mathbf{v}_{rel}$ in Eq. (4.46) can replaced with the thrust ($-\dot{m} g I_{sp}$), so that the acceleration for the entire system is

$$m_h \mathbf{a}_h + m_p \mathbf{a}_p = -T \sin \psi \hat{\mathbf{r}} + \left(R_{\theta h} + R_{\theta p} \right) \hat{\boldsymbol{\theta}} + \left(T \cos \psi + R_{\phi h} + R_{\phi p} \right) \hat{\boldsymbol{\phi}} \tag{4.48}$$

Substituting Eqs. (4.37)–(4.40) and (4.43) into Eq. (4.48), the acceleration of the center of mass in body coordinates is

$$\begin{aligned}
\mathbf{a}_{cm} = {} & \left(-\frac{T \sin \psi}{m} + \frac{2L\dot{m}^2 m_h}{m^3} - \frac{L\ddot{m} m_h}{m^2} \right) \hat{\mathbf{r}} \\
& + \left(\frac{R_{\theta h} + R_{\theta p}}{m} - \frac{2L\dot{m} m_h}{m^2} \dot{\gamma} \cos \theta \right) \hat{\boldsymbol{\theta}} \\
& + \left(\frac{T \cos \psi}{m} + \frac{R_{\phi h} + R_{\phi p}}{m} + \frac{2L\dot{m} m_h}{m^2} \dot{\theta} \right) \hat{\boldsymbol{\phi}}
\end{aligned} \tag{4.49}$$

To convert the acceleration into an inertial frame, the direction cosine matrix is used for the rotation sequence depicted in Fig. 4.4, so that the acceleration in Eq. (4.49) becomes

$$
\mathbf{a}_{cm} = \begin{bmatrix} \cos\gamma\cos\theta & -\sin\gamma & \cos\gamma\sin\theta \\ \sin\gamma\cos\theta & \cos\gamma & \sin\gamma\sin\theta \\ -\sin\theta & 0 & \cos\theta \end{bmatrix}
$$

$$
\times \begin{bmatrix} -T\sin\psi/m + 2L\dot{m}^2 m_h/m^3 - L\ddot{m}m_h/m^2 \\ (R_{\theta h} + R_{\theta p})/m - (2L\dot{m}m_h/m^2)\,\dot{\gamma}\cos\theta \\ T\cos\psi/m + (R_{\phi h} + R_{\phi p})/m + (2L\dot{m}m_h/m^2)\,\dot{\theta} \end{bmatrix}
$$

(4.50)

If instead the particles are considered separately, internal tether forces must be taken into account where $f_{rh} = -f_{rp}$ is the tether tension and $f_{\theta h} = -f_{\theta p}$, $f_{\phi h} = -f_{\phi p}$ are transverse forces applied at the tether endpoints. The transverse forces are in opposite directions at a distance L from each other, so they would produce a torque on the tether. However, the tether is massless, so a net torque is not possible. Therefore the transverse forces must be zero or $f_{\theta h} = f_{\theta p} = f_{\phi h} = f_{\phi p} = 0$.

The acceleration for the habitat can be found by substituting Eq. (4.49) into Eq. (4.37). Using Newton's second law, the equations of motion for the habitat are

$$
\begin{aligned}
\hat{\mathbf{r}}: \quad & f_{rh} = -\frac{m_h}{m}T\sin\psi - \frac{Lm_p m_h}{m}\left(\dot{\gamma}^2\cos^2\theta + \dot{\theta}^2\right) \\
\hat{\boldsymbol{\theta}}: \quad & R_{\theta h} + f_{\theta h} = \frac{m_h}{m}\left(R_{\theta h} + R_{\theta p}\right) + \frac{Lm_p m_h}{m}\left(\ddot{\gamma}\cos\theta - 2\dot{\gamma}\dot{\theta}\sin\theta\right) \\
\hat{\boldsymbol{\phi}}: \quad & R_{\phi h} + f_{\phi h} = \frac{m_h}{m}T\cos\psi + \frac{m_h}{m}\left(R_{\phi h} + R_{\phi p}\right) \\
& \qquad\qquad - \frac{Lm_p m_h}{m}\left(\dot{\gamma}^2\cos\theta\sin\theta + \ddot{\theta}\right)
\end{aligned}
$$

(4.51)

Similarly, the accelerations for the propulsion system are found by substituting Eq. (4.49) into Eq. (4.40). The resulting equations of motion for the propulsion system are

$$
\begin{aligned}
\hat{\mathbf{r}}: \quad & -T\sin\psi + f_{rp} = -\frac{m_p}{m}T\sin\psi + \frac{Lm_pm_h}{m}\left(\dot{\gamma}^2\cos^2\theta + \dot{\theta}^2\right) \\
\hat{\boldsymbol{\theta}}: \quad & R_{\theta p} + f_{\theta p} = \frac{m_p}{m}\left(R_{\theta h} + R_{\theta p}\right) - \frac{Lm_pm_h}{m}\left(\ddot{\gamma}\cos\theta - 2\dot{\gamma}\dot{\theta}\sin\theta\right) \\
\hat{\boldsymbol{\phi}}: \quad & T\cos\psi + R_{\phi p} + f_{\phi p} = \frac{m_p}{m}T\cos\psi + \frac{m_p}{m}\left(R_{\phi h} + R_{\phi p}\right) \\
& \qquad\qquad\qquad\qquad + \frac{Lm_pm_h}{m}\left(\dot{\gamma}^2\cos\theta\sin\theta + \ddot{\theta}\right)
\end{aligned}
\tag{4.52}
$$

Since $f_{\theta h}$ and $f_{\phi h}$ are zero, the $\hat{\boldsymbol{\theta}}$ and $\hat{\boldsymbol{\phi}}$ components in Eq. (4.51) or Eq. (4.52) provide the equations of motion for the system or

$$
\begin{aligned}
\ddot{\gamma} &= 2\dot{\gamma}\dot{\theta}\tan\theta + \frac{m_pR_{\theta h} - m_hR_{\theta p}}{Lm_hm_p\cos\theta} \\
\ddot{\theta} &= -\dot{\gamma}^2\cos\theta\sin\theta + \frac{T\cos\psi}{Lm_p} - \frac{m_pR_{\phi h} - m_hR_{\phi p}}{Lm_hm_p}
\end{aligned}
\tag{4.53}
$$

To enforce $\theta = \psi$ (so that the thrust is along $\hat{\mathbf{z}}$), $\ddot{\theta}$ and the control forces are set to zero in the second equation of Eq. (4.53) to obtain

$$
T/\dot{\gamma}^2 = m_pL\sin\psi
\tag{4.54}
$$

which is the same equation as Eq. (4.8) as found in all the earlier cases.

The second equation in Eq. (4.54) can be differentiated to produce a control law for the spin rate or

$$
\ddot{\gamma} = -\frac{\ddot{m}gI_{sp} + \dot{\gamma}^2\dot{m}L\sin\psi}{2\dot{\gamma}Lm_p\sin\psi}
\tag{4.55}
$$

The desired change in spin rate is then substituted into the first equation of Eq. (4.53) to solve for the control force required to track Eq. (4.55) or

$$
R_{\theta h}m_p - R_{\theta p}m_h = -\frac{m_h\left(\ddot{m}gI_{sp} + \dot{\gamma}^2\dot{m}L\sin\psi\right)}{2\dot{\gamma}\tan\psi}
\tag{4.56}
$$

If the engine is throttled as shown in section 4.2.3, no additional control forces are required, and the mass history follows Eq. (4.30). Whenever the engine does not conform to this thrust profile, the spin rate has to be adjusted by thrusting along $\hat{\boldsymbol{\theta}}$

to maintain $\theta = \psi$. From the second equation in Eq. (4.53), the control force could be along $\hat{\boldsymbol{\phi}}$ to maintain θ, but this control force would be of the same magnitude as the main thruster T.

Slightly rolling the thrust along $\hat{\mathbf{r}}$ points a portion of the main thrust along $\hat{\boldsymbol{\theta}}$ to provide a control force. The new thrust vector in body coordinates is given by Eq. (4.21). The control force is the difference between Eqs. (4.21) and (4.44) or

$$\mathbf{R}_p = \mathbf{T}_\eta - \mathbf{T} = -T \cos \psi \sin \eta \hat{\boldsymbol{\theta}} + T \cos \psi \left(\cos \eta - 1 \right) \hat{\boldsymbol{\phi}} \tag{4.57}$$

By adjusting the roll angle, the control force in Eq. (4.57) follows the nonlinear control input. Then $R_{\theta p}$ in Eq. (4.56) may be replaced with the $\hat{\boldsymbol{\theta}}$ component in Eq. (4.57) resulting in

$$\sin \eta = \frac{\ddot{m} g I_{sp} + \dot{\gamma}^2 \dot{m} L \sin \psi}{2 \dot{m} g I_{sp} \dot{\gamma} \sin \psi} \tag{4.58}$$

where the control force on the habitat or $R_{\theta h}$ is zero. This equation matches the roll angle equation, Eq. (4.33), found previously.

For small angles, the $R_{\phi p}$ component in Eq. (4.56) is essentially zero, and the spin rate is adjusted for almost no cost. Therefore to maintain Eq. (4.54), Eq. (4.58) is used so that a spacecraft can maintain artificial gravity when undergoing a maneuver. The rotational motion is governed by Eq. (4.53), and the inertial accelerations are found by Eq. (4.50).

4.2.6   One Thruster Spin Up

Consider the necessary propellant needed to spin up the tethered spacecraft. Assuming the spin up is done by a thruster on the propulsion system, the only force on the spacecraft is $R_{\theta p} = -\dot{m} g I_{sp}$. The propulsion system mass changes with time while the crew habitat's mass remains constant, so the moments of inertia can still

be modeled as Eq. (4.3). Including jet damping which cancels out some of the effects from the changing inertia [69], Euler's equations of motion reduce to

$$0 = -\frac{L^2 m_h^2 \dot{m}}{m^2} \dot{\eta}$$
$$0 = I\ddot{\theta} + \dot{I}\dot{\theta} \qquad (4.59)$$
$$M_\phi = I\ddot{\phi}$$

where $\dot{\eta}$ is the angular velocity around $\hat{\mathbf{r}}$ and $\dot{\phi}$ is the angular velocity around $\hat{\boldsymbol{\phi}}$. From Eq. (4.59)

$$\dot{\eta} = 0$$
$$\dot{\theta} = \frac{I_0 \theta_0}{I} \qquad (4.60)$$

For a positive spin around $\hat{\boldsymbol{\phi}}$, the thruster must point in the negative $\hat{\boldsymbol{\theta}}$ direction with a torque of

$$M_\phi = -\frac{L g I_{sp} m_h \dot{m}}{m} \qquad (4.61)$$

Integrating the third equation in Eq. (4.59) with this torque gives

$$\dot{\phi} = \frac{g I_{sp}}{L} \log \frac{m_{p0}}{m_p} + \dot{\phi}_0 \qquad (4.62)$$

The artificial gravity level sensed by the crew when the spacecraft is not thrusting is

$$\dot{\phi}_{AG}^2 = \frac{a_{AG} m}{L m_p} \qquad (4.63)$$

where a_{AG} is the desired artificial gravity level. The propellant required to reach this artificial gravity level is found by substituting Eq. (4.63) into Eq. (4.62) for

$$m_{p0} = m_p \exp\left(\frac{1}{g I_{sp}} \sqrt{\frac{a_{AG} L m}{m_p}} - \frac{L \dot{\phi}_0}{g I_{sp}} \right) \qquad (4.64)$$

with

$$m_{p0} = m_p + m_{prop} \qquad (4.65)$$

where m_{prop} is the mass of the propellant. Then the mass required to spin up the spacecraft to a certain artificial gravity level is

$$m_{prop} = m_p \left[\exp\left(\frac{1}{g I_{sp}} \sqrt{\frac{a_{AG} L m}{m_p}} - \frac{L \dot{\phi}_0}{g I_{sp}} \right) - 1 \right] \qquad (4.66)$$

For the one thruster spin-up case, the difference between including and excluding jet damping is very small (less than 1%). When jet damping is not included in the model and there is no initial spin, the expression becomes

$$m_{propNoJet} = m \left[1 - \exp \left(-\frac{1}{gI_{sp}} \sqrt{\frac{a_{AG}Lm_p}{m}} \right) \right] \tag{4.67}$$

To find the inertial velocities, consider Eq. (4.49). For the spin-up case, the only force is $R_{\theta p}$ in the negative $\hat{\theta}$ direction. Then the body fixed accelerations are

$$a_{cm} = \left(\frac{2L\dot{m}^2 m_h}{m^3} - \frac{L\ddot{m}m_h}{m^2} \right) \hat{r} + \left(\frac{\dot{m}gI_{sp}}{m} - \frac{2L\dot{m}m_h}{m^2}\dot{\phi} \right) \hat{\theta} + \frac{2L\dot{m}m_h}{m^2}\dot{\theta}\hat{\phi} \tag{4.68}$$

where $R_{\theta p}$ is $-\dot{m}gI_{sp}$.

If $\dot{\theta}$ is zero, the only angular velocity is $\dot{\phi}$, so the spacecraft is only rotating about the $\hat{\phi}$ axis. Then the inertial accelerations are

$$
\begin{aligned}
a_{cm} = & \left[\left(\frac{2L\dot{m}^2 m_h}{m^3} - \frac{L\ddot{m}m_h}{m^2} \right) \cos\phi + \left(\frac{\dot{m}gI_{sp}}{m} - \frac{2L\dot{m}m_h}{m^2}\dot{\phi} \right) \sin\phi \right] \hat{x} \\
& + \left[\left(\frac{L\ddot{m}m_h}{m^2} - \frac{2L\dot{m}^2 m_h}{m^3} \right) \sin\phi + \left(\frac{\dot{m}gI_{sp}}{m} - \frac{2L\dot{m}m_h}{m^2}\dot{\phi} \right) \cos\phi \right] \hat{y}
\end{aligned} \tag{4.69}
$$

The single thruster causes an undesired velocity in the $\hat{x}$ and $\hat{y}$ directions which can be reduced using a two-burn scheme [30]. The two-burn scheme momentarily suspends the thrust so that when restarted, the velocity is redirected to more desirable position.

4.2.7 Coupled Thruster Spin Up

If an additional equal thruster is added to the habitation system, the spacecraft would not have an inertial acceleration since the force from the thrusters cancel each other out. In this case, the mass of the habitation system and the propulsion system are both changing with time and have the same mass flow rate. The moments of inertia are the same as before, but the time rate of change of the moments of inertia are different where

$$\dot{I} = \frac{L^2\dot{m}\left(m_h^2 + m_p^2\right)}{m^2} \tag{4.70}$$

Including jet damping [69], Euler's equations of motion reduce to

$$0 = -\frac{L^2 \left(m_h^2 + m_p^2\right) \dot{m}}{m^2} \dot{\eta}$$

$$0 = I\ddot{\theta} + \dot{I}\dot{\theta} \tag{4.71}$$

$$M_\phi = I\ddot{\phi}$$

where once again

$$\dot{\eta} = 0$$

$$\dot{\theta} = \frac{I_0 \theta_0}{I} \tag{4.72}$$

For a positive spin around $\hat{\boldsymbol{\phi}}$, the thrusters are aligned in opposite directions where

$$M_\phi = -L\dot{m}gI_{sp} \tag{4.73}$$

Then the equation for $\ddot{\phi}$ is

$$\ddot{\phi} = -\frac{m\dot{m}gI_{sp}}{Lm_p m_h} \tag{4.74}$$

The mass of the habitation system can be written as

$$m_h = m_p + m_{h0} - m_{p0} \tag{4.75}$$

where m_{h0} and m_{p0} are the initial mass values for the habitation and propulsion systems. Equation (4.74) can be rewritten as

$$\ddot{\phi} = -\frac{\dot{m}gI_{sp} \left(2m_p + m_{h0} - m_{p0}\right)}{Lm_p \left(m_p + m_{h0} - m_{p0}\right)} \tag{4.76}$$

which can be integrated into

$$\dot{\phi} = \frac{gI_{sp}}{L} \log \frac{m_{p0} m_{h0}}{m_p m_h} + \dot{\phi}_0 \tag{4.77}$$

To determine the amount of propellant to spin up the spacecraft to a certain artificial gravity level, substitute Eq. (4.63) for $\dot{\phi}$ and solve for m_{prop} noting that

$$m_{p0} = m_{prop}/2 + m_p$$

$$m_{h0} = m_{prop}/2 + m_h \tag{4.78}$$

Then the required mass propellant assuming no initial spin is

$$m_{prop} = -m + \sqrt{m^2 - 4m_p m_h \left[1 - \exp\left(\frac{1}{gI_{sp}}\sqrt{\frac{a_{AG}Lm}{m_p}}\right)\right]} \qquad (4.79)$$

The difference between including and excluding jet damping is even smaller in this case (less than 0.25%). Without jet damping, the required propellant mass is

$$m_{propNoJet} = 2\frac{m_h}{gI_{sp}}\sqrt{\frac{a_{AG}Lm_p}{m}} \qquad (4.80)$$

For a coupled spin up, the forces from the two thrusters cancel out leaving no external forces resulting in no accumulated velocity. While a zero net velocity is attractive, including an additional thruster on the habitation system adds complexity and expense over the simple and elegant single-thruster system discussed throughout this chapter.

4.3 Round Trip Mission to Mars Application

For this analysis, a stop-over mission architecture [83] is assumed in which the unoccupied interplanetary transfer vehicle (Fig. 4.3) stars off in a long period, elliptical orbit around Earth. The crew rendezvous with the transfer vehicle via a smaller "taxi" vehicle which liftoffs from Earth and transfers to the same orbit as the transfer vehicle. A 1 km/s ΔV Earth departure is preformed, and the crew, taxi, and transfer vehicle proceed on a several-month journey to Mars. When approaching Mars, the crew departs the transfer vehicle in the taxi and lands on the surface of Mars. The transfer vehicle performs a 1.5 km/s ΔV to capture into another long period elliptical orbit where it remains in orbit while the crew is on Mars. At the end of the surface stay, the taxi and crew rendezvous with the transfer vehicle in Mars orbit and undergo another 1.5 km/s ΔV burn to escape Mars. Following another several-month journey, the crew departs the transfer vehicle in the taxi and lands on Earth. The transfer vehicle captures into Earth orbit with a 1 km/s ΔV and waits to be resupplied for subsequent missions. The key design parameters for this mission are provided in Table 4.1.

Table 4.1. Mission design assumptions. Reproduced with permission from Landau [64].

Parameter	Value	Notes
Earth orbit capture or departure ΔV	1 km/s	Long period elliptical orbit and moderate interplanetary V_∞
Mars orbit capture or departure ΔV	1.5 km/s	Long period elliptical orbit and moderate interplanetary V_∞
Crew habitat mass	40 t	Crew of 6
Engine I_{sp}	450 s	Liquid hydrogen/liquid oxygen engine
Engine inert/propellant mass ratio	0.16	Cryogenic upper stage
Propulsion system staging	After Mars orbit insertion	Mass optimal to split mission ΔV equally with Earth-Mars stage expended at Mars
Engine throttle range	60–100 %	Limited range simplifies engine design
Engine ramp-up/ramp-down	5 s	Time between zero thrust and full throttle
Artificial gravity level	1 g at Earth 0.38 g at Mars	Vary linearly during interplanetary transit to acclimate crew
Maximum spin rate	4 rpm	Avoid motion sickness
Maximum acceleration	2 g	Limit stress to crew and tether tension

To size the propulsion system, the rocket equation is used where

$$m_p = \frac{m_{payload} \exp\left(\Delta V / g I_{sp}\right)}{1 - \mu\left[\exp\left(\Delta V / g I_{sp}\right) - 1\right]} - m_{payload} \tag{4.81}$$

where $m_{payload}$ is the payload mass and μ is the engine inert-to-propellant mass ratio (0.16 in this case). The propellant mass, m_{prop}, is found by

$$m_{prop} = m\left[1 - \exp\left(-\Delta V/gI_{sp}\right)\right] \tag{4.82}$$

To calculate the required vehicle masses, the Mars departure and Earth arrival are first considered where $m_{payload}$ is only the crew habitat. Then m_p for Mars departure is found by Eq. (4.81) with a ΔV that includes both the Mars departure and Earth arrival ΔV (i.e. 2.5 km/s). The propellant mass, m_{prop}, for Mars departure is calculated by Eq. (4.82) with a ΔV of only the 1.5 km/s (i.e. Mars departure ΔV). The mass of the propulsion system at Earth arrival is found by subtracting the propellant used for the Mars departure from the Mars departure propulsion system mass. The propellant required at Earth arrival is calculated by Eq. (4.82) with a ΔV of 1 km/s. The inert mass, m_{inert} is found by subtracting the propellant used for Earth arrival from the mass of the propellant system at Earth arrival. The resulting vehicle masses are provided in Table 4.2 where m_{prop} is the propellant mass for a single maneuver.

For Earth departure and Mars arrival sizing, the payload is the total mass of the system at Mars departure. Then m_p for Earth departure is found by Eq. (4.81) with a ΔV of 2.5 km/s (i.e. Earth departure and Mars arrival ΔV), and m_{prop} for Earth departure is given by Eq. (4.82) with a ΔV of 1 km/s (i.e. Earth departure ΔV). At Mars arrival, m_p is the mass of the propulsion system at Earth departure minus the propellant needed for Earth departure. The propellant required for Mars arrival with a ΔV of 1.5 km/s is calculated by Eq. (4.82). The inert mass for the Earth-Mars stage, which is discarded after Mars orbit insertion, is the difference between the mass of the propulsion system at Mars arrival and the masses of the propulsion system at Mars departure and the propellant needed for Mars arrival. These values are listed in Table 4.2.

When the spacecraft is not thrusting, the artificial gravity, a_{AG}, sensed by the crew is

$$a_{AG} = \omega^2 L m_p/m \tag{4.83}$$

Table 4.2. Vehicle mass at major events. Reproduced with permission from Landau [64].

Event	m, t	m_p, t	m_{prop}, t	m_{inert}, t
Earth departure	161	121	32.6	
Mars arrival	128	88.4	37.0	11.1
Mars departure	80.3	40.3	23.1	
Earth arrival	57.1	17.1	11.6	5.5

To determine the tether length, the smallest m_p/m of the four maneuvers is obtained which occurs at Earth arrival from Table 4.2. Assuming a maximum angular velocity of 4 rpm [45], the tether length at Earth arrival needed to produce 1 g of artificial gravity is, from Eq. (4.83), at least 187 m. For additional margin, a tether length of 200 m is selected. For improved physiological and psychological health, a spin rate of 1 to 2 rpm is desired [43,84], but at this spin rate, the tether length would be almost 2 km for 1 g of artificial gravity which was deemed less feasible than a high spin rate.

From the first equation in Eq. (4.51), the sensed acceleration is determined by

$$a_{thrusting} = \frac{T \sin \psi}{m} + \frac{L m_p}{m} \left(\dot{\gamma}^2 \cos^2\theta + \dot{\theta}^2 \right) \qquad (4.84)$$

During the controlled burns, $\theta = \psi$ and $\dot{\theta} = 0$. After the maneuver when there is no thrust with $\theta = \psi$ and $\dot{\theta} = 0$, Eq. (4.84) becomes

$$a_{AG} = \frac{L m_p}{m} \dot{\gamma}^2 \cos^2 \psi \qquad (4.85)$$

The largest acceleration is most likely to happen at Earth arrival because the artificial gravity level begins at 1 g and increases with increasing thrust. To reduce the gravity level, the spacecraft could be spun down slightly with additional propellant or alternatively the spacecraft could have a lower artificial gravity level for the return trajectory which may have physiological consequences. In this simulation, however, the crew is not on the spacecraft during Earth arrival since they left on the taxi

Table 4.3. Thrust design points. Reproduced with permission from Landau [64].

Event	a_{AG}, g	$\dot{\gamma}$, rpm	T, kN
End of Earth departure	1	3.60	1,781
Beginning of Mars arrival	0.38	2.22	677
End of Mars departure	0.38	3.37	301
Beginning of Earth arrival	1	5.46	793

previously to land on Earth, so the Earth departure maneuver is where the crew will sense the largest acceleration.

To find the spin rate at Earth departure, $\dot{\gamma}$, the maximum acceleration limit of 2 g is used in Eq. (4.83) where the masses are at the end of the Earth departure burn (from Table 4.2, $m_p = 121 - 32.6 = 88.4$ t). The body-fixed thrust angle, $\psi = 45$ deg is then found by Eq. (4.85) where the artificial gravity level is set to 1 g and the mass values are again at the end of the Earth departure burn. Using the values for ψ and $\dot{\gamma}$, the thrust at the end of the Earth departure burn is determined by Eq. (4.54). The values for $\dot{\gamma}$ and T at the end of the Earth departure are given in Table 4.3. The thrust and body-fixed thrust angle could be found similarly for a maximum acceleration at Earth arrival with Eq. (4.85) applied to the beginning of the burn and Eq. (4.83) applied at the end of the burn, when the largest acceleration is most likely to occur.

The spin rates for the required artificial gravity and associated thrust values for the remaining maneuvers are provided in Table 4.3. The spin rates are found from Eq. (4.85) where the mass values are for either the beginning of the burn or the end of the burn when the mass is diminished by the appropriate m_{prop}. The thrust values are then determined by Eq. (4.54). Since the thrust values in Table 4.3 are sized based on the required artificial gravity before or after the maneuver, additional propellant is not needed to adjust the spin rate.

The Earth departure manuever has the highest thrust level since the spacecraft is the most massive during this burn, so the thrust at the end of the Earth departure burn is used to size the engine. The Earth and Mars arrival maneuvers require half of the Earth departure thrust, and the Mars departure maneuver requires one sixth of the Earth departure thrust. Since the spacecraft rotates on a shorter radius to maintain the desired thrust direction, the spin rate during thrusting, $\dot{\gamma}$, is larger than a simple spin about $\hat{\boldsymbol{\phi}}$.

The spacecraft design would be complete at this point if the engines could throttle to any thrust level to match the spin rate and mass according to Eq. (4.54). However, many engines are unable to operate at low thrust levels due to combustion instability [73], so for this simulation, the engine has a throttle range of 60–100%. By adjusting the spin rate before maneuvers, the spacecraft can still be controlled with a more limited throttle range, but the large difference between required thrust levels imply that the design should incorporate more than one engine. With a 60% thrust level, four 500 kN engines are needed for the maneuvers with four engines at Earth departure, two engines at Mars arrival and Earth arrival, and a single engine at Mars departure as provided in Table 4.4. Four engines of the same size have the additional benefit of reducing the cost of each engine since only one engine would need to be built and qualified.

After the Mars arrival maneuver, the Earth-Mars inert mass is discarded. When releasing the inert mass, the angular velocity does not change, but the spacecraft does gain a few m/s of ΔV.

The angular velocities at the end of the Mars arrival maneuver and the beginning of the Mars departure maneuver should be equal so that no additional thrust is required between the two maneuvers. To achieve the same angular velocity, the thrust at the end of the Mars arrival and the beginning of the Mars departure are throttled so the angular velocities are equal.

After the Earth arrival maneuver, a new 121 t propulsion system replaces the 5.5 t inert Mars-Earth mass to start the cycle again. The new propulsion system docks at

Table 4.4. Derived spacecraft parameters. Reproduced with permission from Landau [64].

Parameter	Value
Tether length	200 m
Engine thrust	500 kN
Number of Earth departure engines	4
Number of Mars arrival engines	2
Number of Mars departure engines	1
Number of Earth arrival engines	2
Thruster offset angle	45 deg

the center of mass and crawls to the end of the tether so that angular momentum is conserved during the acquisition of the new propulsion system. The angular velocity, however, is reduced by

$$\frac{m_{p0}/m_0}{m_{pf}/m_f} = \frac{5.5/45.4}{121/161} = 0.160 \qquad (4.86)$$

To decrease the difference between the angular velocities at the end of the Earth arrival and Earth departure burn, the engines are throttled to maximize the angular velocity at the end of the Earth arrival burn and to minimize the angular velocity at the beginning of Earth departure.

When the engines are starting and ending, the burn is not controlled. Since the spacecraft is spinning at 4 rpm, it undergoes a full revolution every 15 seconds, so the start-up and ending thrust is only aligned in the desired direction for a fraction of time. Even for a few seconds of ramp-up time, the thrust will be misaligned from the desired direction causing a ΔV pointing error. To include these effects, the engines are assumed to take five seconds to linearly ramp-up to the desired thrust level and five seconds to linearly ramp-down to zero. The ramp-up and ramp-down phases of the burn affect the angular velocities, so additional propellant is needed to have equal angular velocities between the Earth maneuvers and the Mars maneuvers.

4.4 Simulation

MATLAB$^{\circledR}$ is used to numerically find the artificial gravilty level and inertial velocity for the four maneuvers. The simulation uses a built in MATLAB$^{\circledR}$ integrator, ode45, which is based on the Dormand Prince method, an explicit Runge-Kutta formula, to solve for the differential equations numerically. The variable step size integral uses tight relative and absolute error tolerances (on the order of 10^{-13}).

For this simulation, the thrust is assumed to vary linearly for the controlled and uncontrolled portions of the burn so that $\ddot{m}$ is constant or equivalently

$$m = m_0 + \dot{m}_0 t + \ddot{m} t^2 \tag{4.87}$$

The propellant required for each maneuver in Table 4.2 assumes all of the velocity occurs in one direction. However, the maneuvers discussed here require slightly more propellant than given in Table 4.2 (totaling around 7 kg for the four maneuvers) to correct small transverse velocities to achieve the required ΔV in Table 4.1. The engines here can only throttle to 60% unlike in Table 4.1 where the engines can achieve any thrust level. The number of engines for each maneuver is also given in Table 4.4.

4.4.1 Earth Departure

For the Earth departure burn, this simulation assumes that the m_{prop} in Table 4.2 plus a small margin is used during the controlled and uncontrolled burns. The next step is to find the initial $\dot{m}$ and constant $\ddot{m}$ values for each of the three sections of the thrust profile: ramp-up (1), controlled (2), and ramp-down (3).

Table 4.2 gives the required spin rate at the end of the Earth departure burn, $\dot{\gamma}_2$. Ideally this spin rate would be targeted at the end of the ramp-down phase, but since there is no relationship between thrust and spin rate in the uncontrolled sections, the spin rate is targeted at the end of the control burn where the spin rate and thrust

level are related by Eq. (4.54). After some algebra, the mass of propellant for the ramp-up and controlled burn is

$$m_{prop12} = (m_{prlp} - \beta m_0 + \beta m_h) / (1 - \beta) \tag{4.88}$$

where m_{prop} is the propellant used for the Earth departure burn plus the propellant margin, m_0 is the mass of the spacecraft at the beginning of the burn plus the propellant margin, and β is

$$\beta = L \ t_r \dot{\gamma}_2^2 \sin \psi / (2g I_{sp}) \tag{4.89}$$

where t_r is the ramp-up time (5 seconds).

The propellant for the ramp-down section, m_{prop3}, is the difference between the total propellant, m_{prop}, and the propellant for the ramp-up and controlled sections, m_{prop12}. The mass flow rate at the end of the controlled section is

$$\dot{m}_{2f} = -2m_{prop3}/t_r \tag{4.90}$$

and the mass flow rate at the beginning of the controlled section is

$$\dot{m}_{20} = - \left(2m_{prop12} + \dot{m}_{2f}\right) / \left(t_2 + t_r\right) \tag{4.91}$$

where t_2 is the time of the controlled burn which is adjusted to achieve the desired ending ΔV_Z.

Since the maximum thrust is limited and equal to $-\dot{m}gI_{sp}$, the mass flow rates at the beginning and end of the controlled section must be below the maximum thrust. However, the calculated mass flow rates from Eqs. (4.90) and (4.91) both exceed the maximum thrust because the m_{prop} in Table 4.2 is now split over the three sections of the burn. The thrust linearly increases during Earth departure, so the maximum thrust is set to be at the end of the controlled section where

$$\dot{m}_{2f} = -T_{max} / (gI_{sp}) \tag{4.92}$$

Then the propellant for the ramp-up and ramp-down sections is

$$m_{prop1} = -\dot{m}_{20}t_r/2$$
$$m_{prop3} = -\dot{m}_{2f}t_r/2 \tag{4.93}$$

The mass flow rate at the beginning of the controlled section is found by Eq. (4.91) where m_{prop12} is the total propellant minus m_{prop3} found in Eq. (4.93). The initial thrust does not fall below the 60% throttle range, so $\dot{m}_{20}$ does not have to be modified further.

The $\ddot{m}$ values are calculated by

$$\ddot{m}_1 = \dot{m}_{20}/t_r$$
$$\ddot{m}_2 = (\dot{m}_{2f} - \dot{m}_{20})/t_2 \tag{4.94}$$
$$\ddot{m}_3 = -\dot{m}_{2f}/t_r$$

Then the mass for each section of the thrust is

$$m_1 = m_0 + \ddot{m}_1 t^2/2$$
$$m_2 = m_0 - m_{prop1} + \dot{m}_{20}t + \ddot{m}_2 t^2/2 \tag{4.95}$$
$$m_3 = m_0 - m_{prop12} + \dot{m}_{2f}t + \ddot{m}_3 t^2/2$$

where t starts at 0 and goes to t_r or t_2.

Since the thrust level at the end of the controlled thrust is now at maximum thrust, the spin at the end of the burn must be reevaluated by the control law in Eq. (4.54) or

$$\dot{\gamma}_{2f}^2 = -\frac{\dot{m}_{2f}gI_{sp}}{L\sin\psi\,(m_0 - m_h - m_{prop12})} \tag{4.96}$$

To simulate the ramp-up phase, the final conditions of the ramp-up phase must match the initial conditions of the controlled phase to ensure that the controlled burn occurs when $\theta = \psi$. Since θ is constant during the controlled burn, the only unknown initial condition is the initial spin rate, $\dot{\gamma}_{20}$. To find the initial spin rate, the controlled burn is integrated backwards with the spin rate as given by Eq. (4.96) and the constant $\theta = \psi$. The mass is given by the second equation in Eq. (4.95). The angular rates are found by integrating Eq. (4.17) with the moment of inertia given by Eq. (4.3) and the torques given in Eq. (4.22) where $\cos\eta$ is not reduced to unity and η follows Eq. (4.58). The inertial velocities arise from the integration of Eq. (4.50).

Once the conditions at the start of the burn are known, they are used as the final conditions for the 5 second ramp-up phase. Here the same equations are used to

simulate the motion except that η is constant and fixed to be the η at the beginning of the controlled burn. The mass is given by the first equation in Eq. (4.95).

The ramp-down phase uses the conditions at the end of the controlled burn as the initial conditions, and the same differential equations are now integrated forwards with a fixed η that is the η at the end of the controlled burn. The mass is found by the third equation in Eq. (4.95).

To achieve a 1 km/s ΔV_Z at the end of the ramp-down phase, the controlled burn time and propellant margin are adjusted. During the three burn sections, the artificial gravity level is found by Eq. (4.84).

4.4.2   Mars Arrival

For the Mars arrival burn, the spin rate in Table 4.3 is the spin rate at the beginning of the controlled burn. Then the propellant mass used during the ramp-up is

$$m_{prlp1} = (m_0 - m_h)\, \beta / (1 + \beta) \tag{4.97}$$

where m_0 is the mass of the spacecraft plus the propellant margin at the beginning of the manuever and β is found by Eq. (4.89). The initial and final mass flow rates of the controlled burn are

$$
\begin{aligned}
\dot{m}_{20} &= -2m_{prop1}/t_r \\
\dot{m}_{2f} &= -\left(2m_{prop23} - \dot{m}_{20}t_2\right)/\left(t_r + t_2\right)
\end{aligned}
\tag{4.98}
$$

where m_{prop23} is the mass of the propellant used during the controlled and ramp-down sections $(m_{prop} - m_{prop1})$.

According to Table 4.4, the Mars arrival manuever uses two of the four engines which have a minimum thrust of 600 kN. Since the thrust linearly decreases during the Mars arrival maneuver, $\dot{m}_{2f}$ must have a resulting thrust that is above 600 kN. In this simulation, the minimum thrust ends below this threshold, so the thrust at the end of the controlled burn and its corresponding $\dot{m}$ are fixed at the minimum level

(i.e. $\dot{m}_{20}$ remains the same). Then the propellant used during the ramp-down section is determined by Eq. (4.93), and the controlled burn time is determined by

$$t_2 = -2m_{prop12}/\left(\dot{m}_{20} + \dot{m}_{2f}\right) \tag{4.99}$$

The initial spin rate is then reevaluated by Eq. (4.54) or

$$\dot{\gamma}_{20}^2 = -\frac{\dot{m}_{20}gI_{sp}}{L\sin\psi\left(m_0 - m_h - m_{prop1}\right)} \tag{4.100}$$

The $\ddot{m}$ values are given by Eq. (4.94) and the masses are given by Eq. (4.95).

Since $\dot{\gamma}_{20}$ is known, the ramp-up phase is first simulated backwards with a constant η given by Eq. (4.58) using the initial conditions of the controlled burn. The angular rates are found by integrating Eq. (4.17) with the moment of inertia given by Eq. (4.3) and the torques given in Eq. (4.22). The inertial velocities arise from the integration of Eq. (4.50).

The controlled burn is propagated forward using these same equations except that η now follows Eq. (4.58). The ramp-down phase uses the conditions at the end of the controlled burn as the initial conditions, and the same equations are now simulated forwards with a fixed η that is the the value of η at the end of the controlled burn. During the three burn sections, the artificial gravity level is found by Eq. (4.84).

Since the controlled burn time is fixed in this case, only the propellant margin can be changed to achieve the ending ΔV_Z of 1.5 km/s.

4.4.3 Mars Departure

Similar to the Earth departure scenario, the spin rate given in Table 4.3 for Mars departure occurs at the end of the manuever. Then the propellant for the ramp-up and controlled burns is given by Eq. (4.88) while β is obtained from Eq. (4.89). The initial and final mass flow rates for the controlled section are found from Eqs. (4.90) and (4.91).

From Table 4.4, the Mars departure has one engine, and the resulting thrust from $\dot{m}_{20}$ and $\dot{m}_{2f}$ is in the throttable range of the engine. Then the propellant required

for the ramp-down burns are found by Eq. (4.93), the $\ddot{m}$ values are found by Eq. (4.94), and the spacecraft mass is found by Eq. (4.95).

The new spin rate is determined by Eq. (4.96), and the simulation of the manuever follows the description of the Earth departure simulation.

4.4.4   Earth Arrival

The Earth arrival maneuver follows the same procedure as the Mars departure maneuver. The Earth arrival maneuver also uses two engines, and the minimum thrust must be kept above 600 kN with a procedure similar to the Mars arrival maneuver.

4.4.5   Simulation Results

The mass flow rates, the propellant margin, and the controlled burn time for the four maneuvers are given in Table 4.5. The arrival maneuvers have a larger propellant margin than the departure maneuvers since the controlled burn time is fixed and only the propellant margin can be adjusted to achieve the required ΔV_Z. The undesired transverse velocities from the Mars maneuvers are smaller than the Earth maneuvers, so the propellant margin is also smaller for the Mars maneuvers.

Table 4.5. Spacecraft parameters for the maneuvers.

Maneuver	$\dot{m}_{20}$, kg/s	$\dot{m}_{2f}$, kg/s	Prop margin, kg	t_2, s
Earth departure	-412	-453	2.7	71
Mars arrival	-153	-136	0.27	251
Mars departure	-112	-69	0.05	250
Earth arrival	-175	-136	3.5	70
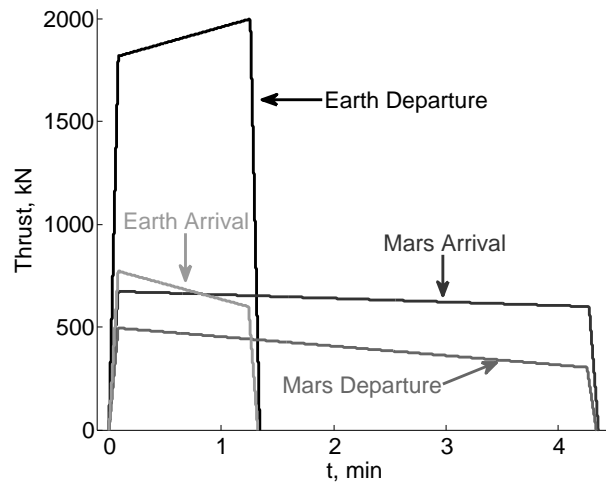
Figure 4.5. Thrust histories for the four maneuvers.

The resulting thrust profiles for the four maneuvers which include the ramp-up and ramp-down portions are shown in Fig. 4.5. As expected from Table 4.3, the largest thrust occurs at Earth departure when the spacecraft is most massive, and the smallest thrust occurs at Mars departure. The final thrust at Earth departure is at maximum thrust so that the corresponding spin rate from Eq. (4.54) can achieve 1 g artificial gravity at the end of the ramp-down burn.

Figure 4.6 shows that the controlled burn tracks ψ (at 45 degrees) when the thrust is at operating at high thrust levels. For this simulation, ψ is the same for each maneuver, but if the spacecraft began a maneuver at a different orientation, ψ must be changed so that Eq. (4.54) holds. The uncontrolled burns (ramp-up and ramp-down) shown by the vertical lines demonstrate the transition from free motion where θ oscillates as the spacecraft spins at an angle to $\hat{\mathbf{z}}$ to controlled flight when θ is constant.

The control angle, η, is shown in Fig. 4.7 which adjusts the thrust direction along the positive $\hat{\mathbf{r}}$ direction. The horizontal sections at the beginning and end of the η curves (most clearly evident at Earth arrival) arise from a constant η during the
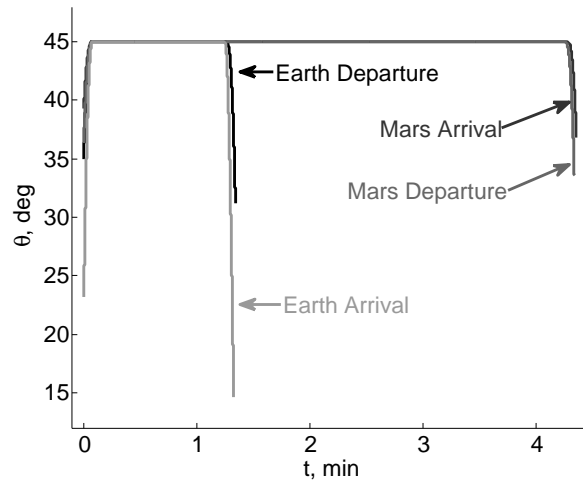
Figure 4.6. θ for the four maneuvers.

ramp-up and ramp-down phases. The Earth maneuver values of η are larger than the Mars maneuvers, but all values for η are less than one degree. Therefore the small angle assumption made to find Eq. (4.33) holds. These small angles are the only adjustment needed to achieve the required spin rate specified in Eq. (4.54) to maintain the desired thrust direction.

The spin rates shown in Fig. 4.8 are below 4 rpm except for the Earth arrival maneuver. During the Earth arrival maneuver, however, the crew has already departed the transfer vehicle to land on Earth, so the high spin rate will not cause crew physiological problems. A large final spin rate at the Earth arrival is necessary since the spin rate will decrease once the propulsion system for the next mission to Mars is added. With the additional mass, the final spin rate of 4.4 rpm will fall to 0.71 rpm following the reduction ratio in Eq. (4.86). Additional propellant must be spent to increase the spin rate from 0.71 rpm to 2.3 rpm, the spin at the beginning of Earth departure. Propellant is also needed for a 0.04 rpm increase in spin rate between the Mars arrival and Mars departure maneuvers.
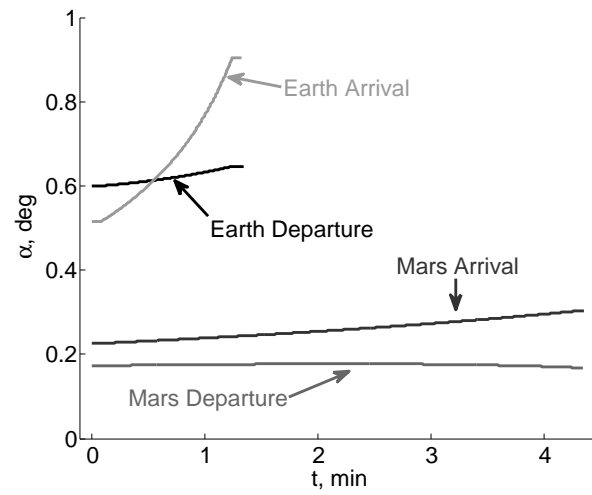
Figure 4.7. Control angle, η, for the four maneuvers.
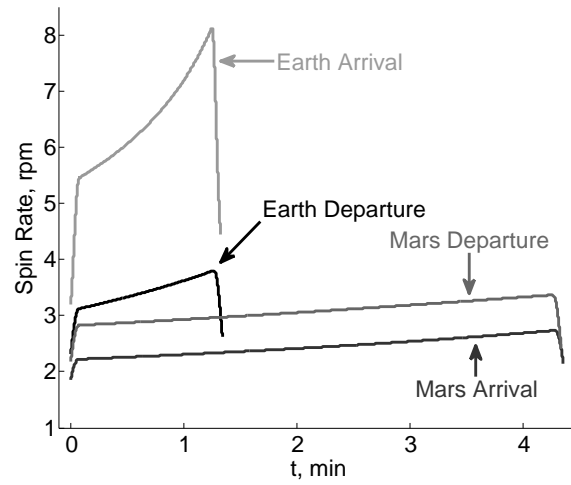
Figure 4.8. Spin rate, $\dot{\gamma}$, for the four maneuvers.
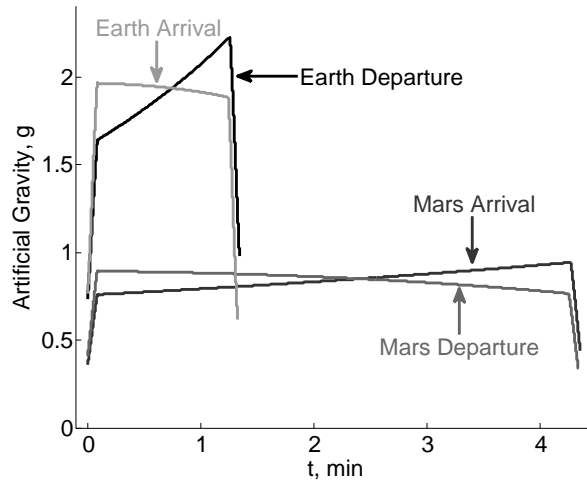
Figure 4.9. Artificial gravity level for the four maneuvers.

The maximum artificial gravity level shown in Fig. 4.9 occurs during Earth departure instead of Earth arrival. Replacing $\dot{\gamma}$ in Eq. (4.83) with the thrust as indicated by Eq. (4.54), the sensed artificial gravity is proportional to T/m. Since the thrust during Earth departure is decreasing faster than the mass, the artificial gravity also decreases. Contrarily, at Mars arrival, the artificial gravity is increasing while the thrust is decreasing, but the change in thrust level over the maneuver is much smaller. If the Earth arrival thrust was less variable, the artificial gravity could increase and, by the end of the controlled burn, become larger than the artificial gravity at Earth departure.

The maximum acceleration at Earth departure exceeds the design limit of 2 g which is expected since the corresponding thrust of 2,000 kN is above the design level of 1,800 kN. The artificial gravity level at the beginning of Mars arrival is at 0.36 g, and the artificial level at the end of Mars departure is 0.34 g which are both slightly below the 0.38 g requirement. The artificial gravity level at the beginning of the Earth arrival maneuver is 0.73, and the artificial gravity level at the end of the Earth departure maneuver is 0.61 g which are also both below the 1 g requirement.

Additional propellant is needed to increase these artificial gravity levels to conform with the requirements listed in Table 4.1.
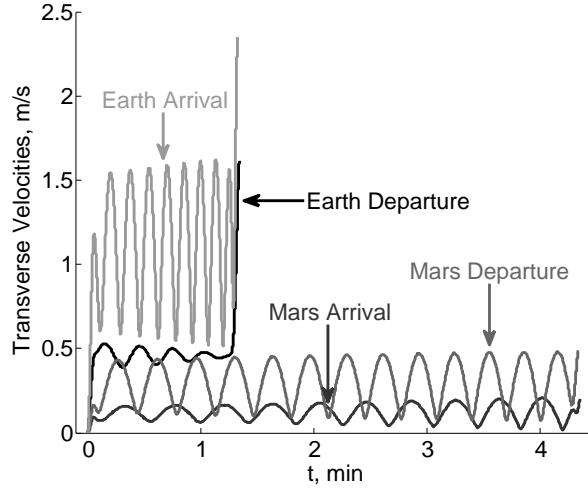
Figure 4.10. Transverse velocities for the four maneuvers.

Figure 4.10 shows the ΔV errors (i.e. undesired transverse velocities) during the maneuvers. The largest errors occur during Earth arrival and Earth departure mainly due to the poor thrust direction during the uncontrolled portions of the burn. The transverse velocity gained by the ramp-down burn at Earth arrival is larger than the Earth departure because the spacecraft is spinning at a higher rate (above 8 rpm at the end of the controlled burn) causing the engine to thrust at a larger misaligned angle. The transverse velocities at Earth arrival have large oscillations since the roll angle, η, is the at its largest, causing the most unwanted velocity. These velocities, however, are very small compared to the final ΔV_Z of 1 km/s or 1.5 km/s.

4.4.6 Mass to Adjust Spin Rate

To compare the scenario examined here with a spacecraft that is not spinning during maneuvers, consider the additional propellant required in Table 4.6. The spacecraft is spun down before the Earth and Mars arrival maneuvers and then spun

Table 4.6. Propellant for single and coupled thruster with and without jet damping.

Spin-Up Maneuver	m_{propSJ}	$m_{propSNJ}$	m_{propCJ}	$m_{propCNJ}$
	kg	kg	kg	kg
Earth departure	1,408	1,396	699	696
Mars arrival	661	658	412	411
Mars departure	353	351	351	351
Earth arrival	194	193	272	271
Sum	2,616	2,598	1,734	1,729

up to the required artificial level after the Earth and Mars departure maneuvers. The propellant for the single thruster with jet damping, m_{propSJ}, is calculated from Eq. (4.66), the propellant for the single thruster without jet damping, $m_{propSNJ}$, is calculated from Eq. (4.67), the propellant for the coupled thruster with jet damping, m_{propCJ}, is calculated from Eq. (4.79), and the propellant for the coupled thruster without jet damping, $m_{propCNJ}$, is calculated from Eq. (4.80). The same specific impulse of 450 seconds is assumed for these calculations. This specific impulse may be high for a control system, but it is used to compare the propellant with the thrusting while spinning case explored earlier.

The difference between including and excluding jet damping is very small as Table 4.6 demonstrates. The coupled thruster require less propellant (almost 1,000 kg less), but the complexities and expense of requiring a thruster far away from the propulsion system may not be worth the mass savings.

The additional propellant needed for the thrusting while spinning case is given in Table 4.7. The propellant to correct the transverse ΔV errors is found by Eq. (4.82). The artificial gravity corrections refer to adjusting the artificial gravity levels to those given in Table 4.1 ranging from the beginning through the ending of the long interplanetary trajectories. The mass for these correction is approximated by Eq. (4.80). The artificial gravity between the Earth and Mars maneuvers does not

Table 4.7. Additional propellant costs associated with maneuvers.

Correction	Manuever	Mass, kg
Transverse ΔV	End of Earth departure	47
	End of Mars arrival	4
	End of Mars departure	6
	End of Earth arrival	24
Artificial Gravity	End of Earth departure	8
	Beginning of Mars arrival	11
	End of Mars departure	68
	Beginning of Earth arrival	55
Spin Rate	End of Earth arrival	377
	End of Mars arrival	33
Propellant margin	(see Table 4.5)	7
	Sum	640

have to be corrected to either 1 g or 0.38 g since the crew is not on board the transfer vehicle. However, the spin rates between the Earth and Mars maneuvers must match requiring a spin rate maintenance maneuver. The spin rate correction is determined by matching the artificial gravity levels between the Earth and Mars maneuvers via Eq. (4.80).

Clearly the spinning while thrusting method requires much less propellant, over 1,000 kg less, than spinning down the spacecraft between burns. The majority of the additional propellant for the spinning and thrusting spacecraft occurs when adjusting the spin rate before the new propulsion stage is added between Earth maneuvers. To reduce the additional propellant, the engine throttle range could be increased and the controlled burn times could be adjusted to better match the artificial gravity levels and spin rates.

4.4.7 Two-Burn Scheme

As mentioned earlier, a two-burn scheme where the burn is momentarily suspended and then re-started could be used to reduce the transverse velocities while spinning up a spacecraft with one thruster [30]. Applied to the initial spin up before the first Earth departure maneuver, Eq. (4.59) is used to find the angular velocities assuming the spacecraft is not initially spinning. The inertial velocities are calculated by integrating Eq. (4.69).

(a) Constant Burn   (b) Two-Burn Scheme
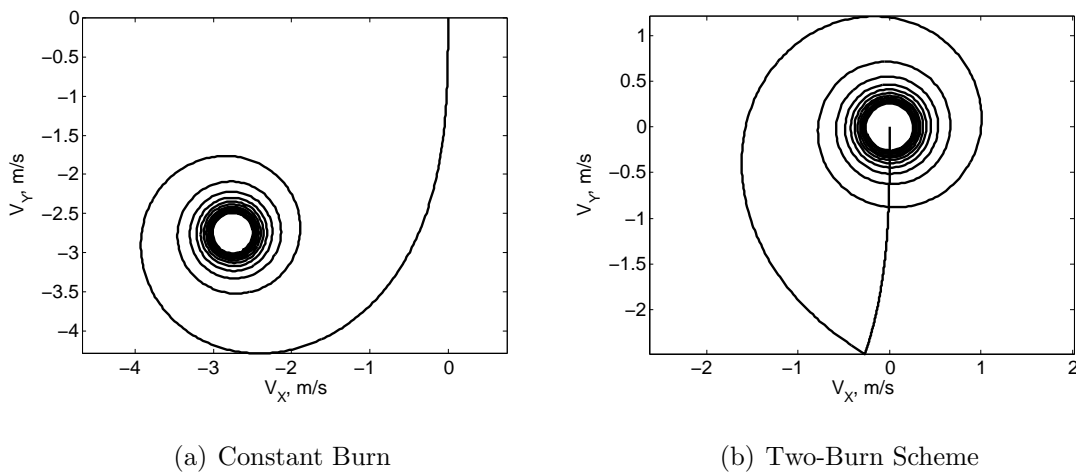
Figure 4.11. Transverse velocities for a one thruster spin up.

The transverse velocity components for a constant, uninterrupted burn are shown in Fig. 4.11(a). The transverse velocities initially grow rapidly, but eventually end up spiraling towards a point with a center at around 4 m/s. The two-burn scheme is applied to move the center of that circle to zero as shown in Fig. 4.11(b). In this case, the burn is interrupted after 39.4 seconds for 107.4 seconds resulting in a transverse velocity of 0.25 m/s. If instead the ending velocity is minimized, the burn should be suspended after 38.4 seconds for 116.8 seconds with an ending veloicty of 1.4 mm/s.

4.5   Summary

A tethered spacecraft with a propulsion system on one end of the tether can perform large transfer maneuvers while spinning by adjusting the thrust magnitude and spin rate. With this control law, artificial gravity is present during the entire mission, and the spacecraft is not required to despin or to change the tether length. Furthermore, the angular momentum vector does not need to be reoriented. Thus the new maneuver reduces spacecraft mass and complexity.

To control the thrust in a desired direction, the thrust can either change magnitude or slightly roll along the tether axis. Since the spacecraft is not despinning between maneuvers, a considerable amount of propellant is saved while artificial gravity is continuously supplied on the spacecraft. Thus a simple spacecraft design provides an attractive alternative to other proposed configurations.

5. Motion of a Self-Excited Rigid Body

5.1 Background

It is well known that the attitude solution for a self-excited rigid body given in Leimanis [1] based on work done by Bödewadt [85] is more limited than presented [23, 86]. Longuski proved that Bödewadt's solution still holds when the spin vector doesn't change but the solution breaks down when a spacecraft has a variable spin rate [86]. It was uncertain if Bödewadt's solution could be used as an approximation for the attitude angles for a spacecraft with a changing spin rate, so this analysis was completed to determine how different the Bödewadt solution is to a numerical integration of the equations of motion.

5.2 Solution Model

To solve for the attitude, the following equation must be solved

$$\dot{\mathbf{A}} = \mathbf{A}\mathbf{W} \tag{5.1}$$

where $\mathbf{A}$ is an Euler rotation matrix and

$$\mathbf{W} = \begin{bmatrix} 0 & -\omega_z & \omega_y \\ \omega_z & 0 & -\omega_x \\ -\omega_y & \omega_x & 0 \end{bmatrix} \tag{5.2}$$

The solution to the differential equation in Eq. (5.1) is found by multiplying by an integration factor

$$\dot{\mathbf{A}}e^{-\mathbf{U}} - \mathbf{A}\mathbf{W}e^{-\mathbf{U}} = 0 \tag{5.3}$$

The matrix $\mathbf{U}$ is defined as

$$\mathbf{U} = \begin{bmatrix} 0 & -\xi & \lambda \\ \xi & 0 & -\zeta \\ -\lambda & \zeta & 0 \end{bmatrix} = \int_{t_0}^{t} \mathbf{W} dt \tag{5.4}$$

where

$$\zeta = \int_{t_0}^{t} \omega_x dt$$

$$\lambda = \int_{t_0}^{t} \omega_y dt \tag{5.5}$$

$$\xi = \int_{t_0}^{t} \omega_z dt$$

The matrix exponential is defined as [87]

$$e^{\mathbf{U}(t)} = \sum_{k=0}^{\infty} \frac{1}{k!} \mathbf{U}(t)^k = \mathbf{I} + \mathbf{U}(t) + \frac{1}{2}\mathbf{U}(t)^2 + \dots \tag{5.6}$$

The derivative of the matrix exponential is

$$\frac{d}{dt}\left[e^{\mathbf{U}(t)}\right] = \sum_{k=}^{\infty} \frac{d\left[\mathbf{U}(t)^k\right]}{dt} = \frac{d\left[\mathbf{U}(t)\right]}{dt} + \frac{1}{2}\frac{d\left[\mathbf{U}(t)^2\right]}{dt} + \dots \tag{5.7}$$

For any value of k, Eq. (5.7) can be expanded into

$$\frac{d\left[\mathbf{U}(t)^k\right]}{dt} = \frac{d\left[\mathbf{U}(t)^{k-1}\right]}{dt}\mathbf{U}(t) + \mathbf{U}(t)^{k-1}\frac{d\left[\mathbf{U}(t)\right]}{dt} \tag{5.8}$$

For $k = 1$, Eq. (5.8) becomes

$$\frac{d\left[\mathbf{U}(t)\right]}{dt} = \frac{d\left(\int \mathbf{W} dt\right)}{dt} = \mathbf{W} \tag{5.9}$$

For $k = 2$, Eq. (5.8) becomes

$$\frac{1}{2}\frac{d\left[\mathbf{U}(t)^2\right]}{dt} = \frac{1}{2}\frac{d\left(\int \mathbf{W} dt\right)}{dt}\mathbf{U} + \frac{1}{2}\mathbf{U}\frac{d\left(\int \mathbf{W} dt\right)}{dt} = \frac{1}{2}\mathbf{W}\mathbf{U} + \frac{1}{2}\mathbf{U}\mathbf{W} \tag{5.10}$$

When $\mathbf{W}$ and $\mathbf{U}$ commute, Eq. (5.10) equals $\mathbf{W}\mathbf{U}$. A similar analysis can be done for the remaining k entries which all require $\mathbf{W}$ and $\mathbf{U}$ to commute in order to equal

the corresponding entry in $\mathbf{W}$ times Eq. (5.6). If commutation holds, Eq. (5.1) can be solved as

$$\mathbf{A} = \mathbf{A}(t_0) e^{\mathbf{U(t)}} = \mathbf{A}(t_0) \left[\mathbf{I} + \mathbf{U}(t) + \frac{1}{2}\mathbf{U}(t)^2 + ... \right] \tag{5.11}$$

which is the solution given by Bödewadt [1]. However, for $\mathbf{W}$ and $\mathbf{U}$ to commute, $\omega \times \mathbf{M} = 0$ which true in only a few cases [86].

5.3 Numerical Simulation of a Spinning, Thrusting Spacecraft

Consider the case of an axisymmetric spacecraft with an offset and misaligned thrust undergoing a constant burn. The offset and misaligned thrust cause a torque in the x-direction where

$$M_x = F(h \sin \alpha + d \cos \alpha) \tag{5.12}$$

where F is the force from the thruster, α is the thrust misalignment, d is the thrust offset, and h is the distance from the center of mass of the spacecraft to the nozzle. These constant variables have values of

$$d = 0.02 \text{ m}, \quad \alpha = 0.25 \text{ deg}, \quad h = 0.8 \text{ m}, \quad F = 76,000 \text{ N} \tag{5.13}$$

The mass properties of the spacecraft are

$$I_x = I_y = 858 \text{ kg m}^2, \quad I_z = 401 \text{ kg m}^2, \quad m = 2500 \text{ kg} \tag{5.14}$$

The spacecraft is initially spinning about the z-axis with ω_z equal to 70 rpm. All other initial conditions are zero.

A highly precise numerical integration is compared against the analytical solution of Bödewadt. For the numerical simulation, Euler's equations of motion are used to find the angular velocities [66] with

$$\begin{aligned}
\dot{\omega}_x(t) &= M_x/I_x - [(I_z - I_y)/I_x]\,\omega_y\omega_z \\
\dot{\omega}_y(t) &= M_y/I_y - [(I_x - I_z)/I_y]\,\omega_z\omega_x \\
\dot{\omega}_z(t) &= M_z/I_z - [(I_y - I_x)/I_z]\,\omega_x\omega_y
\end{aligned} \tag{5.15}$$

The kinematic equations, which describe the orientation of a rigid body with respect to the inertial reference frame, are found using a Type-I, Euler sequence 3-1-2 (ϕ_z, ϕ_x, ϕ_y) given by Wertz [67] where

$$
\begin{aligned}
\dot{\phi}_x &= \omega_x \cos \phi_y + \omega_z \sin \phi_y \\
\dot{\phi}_y &= \omega_y - (\omega_z \cos \phi_y - \omega_x \sin \phi_y) \tan \phi_x \\
\dot{\phi}_z &= (\omega_z \cos \phi_y - \omega_x \sin \phi_y) \sec \phi_x
\end{aligned}
\tag{5.16}
$$

After integrating Eqs. (5.15) and (5.16), the Euler angles are compared against the Euler angles found using Eq. (5.11). The matrix $\mathbf{A}$ is a Type I, 3-1-2 rotation matrix [67] where

$$
\mathbf{A} = \begin{bmatrix}
c\phi_y c\phi_z - s\phi_x s\phi_y s\phi_z & -c\phi_x s\phi_z & s\phi_y c\phi_z + s\phi_x c\phi_y s\phi_z \\
c\phi_y s\phi_z + s\phi_x s\phi_y c\phi_z & c\phi_x c\phi_z & s\phi_y s\phi_z - s\phi_x c\phi_y c\phi_z \\
-c\phi_x s\phi_y & s\phi_x & c\phi_x c\phi_y
\end{bmatrix}
\tag{5.17}
$$

where c and s are abbreviations for cosine and sine functions, respectively.

To find the Bödewadt solution, analytical solutions must first be found for the angular velocities and their integrals. Since the spacecraft is symmetric and there is no torque in the z-direction, the third equation in Eq. (5.15) simplifies to

$$
\dot{\omega}_z(t) = 0
\tag{5.18}
$$

Then clearly ω_z is a constant or

$$
\omega_z = \omega_{z0}
\tag{5.19}
$$

The remaining two other angular velocities are [1]

$$
\begin{aligned}
\omega_x &= \omega_{x0} \cos k\omega_{z0} t + \omega_{y0} \sin k\omega_{z0} t + \frac{M_x}{I_t k \omega_{z0}} \sin k\omega_{z0} t + \frac{M_y}{I_t k \omega_{z0}} (1 - \cos k\omega_{z0} t) \\
\omega_y &= \omega_{y0} \cos k\omega_{z0} t - \omega_{x0} \sin k\omega_{z0} t + \frac{M_y}{I_t k \omega_{z0}} \sin k\omega_{z0} t - \frac{M_x}{I_t k \omega_{z0}} (1 - \cos k\omega_{z0} t)
\end{aligned}
\tag{5.20}
$$

where I_t is $I_x = I_y$ and k is $(I_t - I_z)/I_t$

The integrals of the angular velocities are

$$
\zeta = \frac{M_y t}{I_t k \omega_{z0}} + \left(\frac{\omega_{y0}}{k \omega_{z0}} + \frac{M_x}{I_t k^2 \omega_{z0}^2} \right) (1 - \cos k \omega_{z0} t)
$$
$$
+ \left(\frac{\omega_{y0}}{k \omega_{z0}} - \frac{M_y}{I_t k^2 \omega_{z0}^2} \right) \sin k \omega_{z0} t
$$
$$
\lambda = \frac{M_x t}{I_t k \omega_{z0}} + \left(-\frac{\omega_{x0}}{k \omega_{z0}} + \frac{M_y}{I_t k^2 \omega_{z0}^2} \right) (1 - \cos k \omega_{z0} t) \qquad (5.21)
$$
$$
+ \left(\frac{\omega_{y0}}{k \omega_{z0}} + \frac{M_x}{I_t k^2 \omega_{z0}^2} \right) \sin k \omega_{z0} t
$$
$$
\xi = \omega_{z0} t
$$

The Euler angles are found by Eq. (5.11) where $\mathbf{A}(t_0)$ is Eq. (5.17) evaluated at the initial conditions.

Figure 5.1 shows ϕ_x and ϕ_y for a highly precise numerical integration of Euler's equations of motion and the kinematic equations (black lines) as well as the Bödewadt solution (gray dashed line). The two results are close since the angles are small, but the Bödewadt solution fails to capture the behavior of the actual attitude angles. For this reason, the Bödewadt solution is not a good approximation for the attitude angles.

The Bödewadt solution does capture the ϕ_z behavior as shown in Fig. 5.2 where the solutions differ by an order of 10^{-5} degrees. The solutions match because the constant ω_z dominates the other angular velocities which have maximum values that are three orders of magnitude less than ω_z. However, in this case, ϕ_z is very easy to find analytically, so the Bödewadt solution is not needed.

5.4   Summary

While the Bödewadt solution was previously known to be erroneous [86], a numerical study of the effect has not been shown. This chapter shows that while the Bödewadt solution can predict ϕ_z fairly accurately for a spacecraft with changing spin, it is unable to accurately predict the other attitude angles.

(a) ϕ_x vs. t
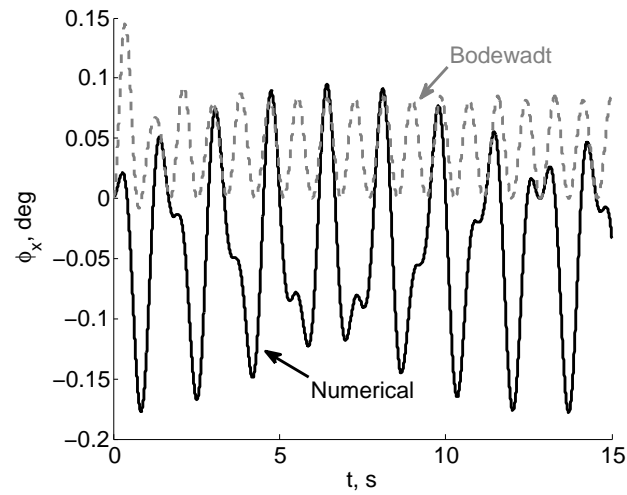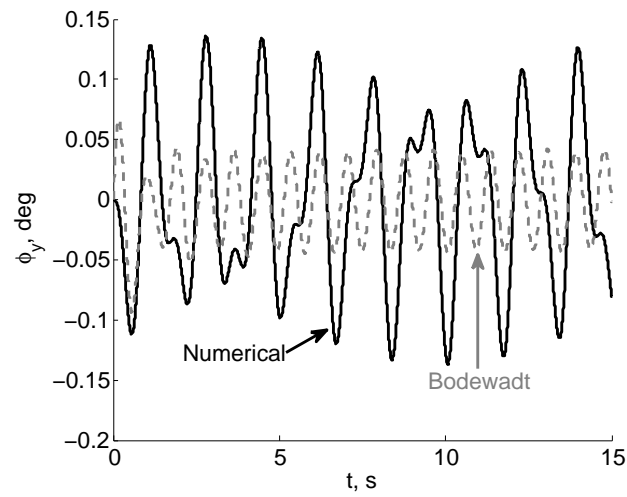
(b) ϕ_y vs. t

Figure 5.1. Euler angles using numerical integration (black line) and the Bödewadt solution (gray dashed line).
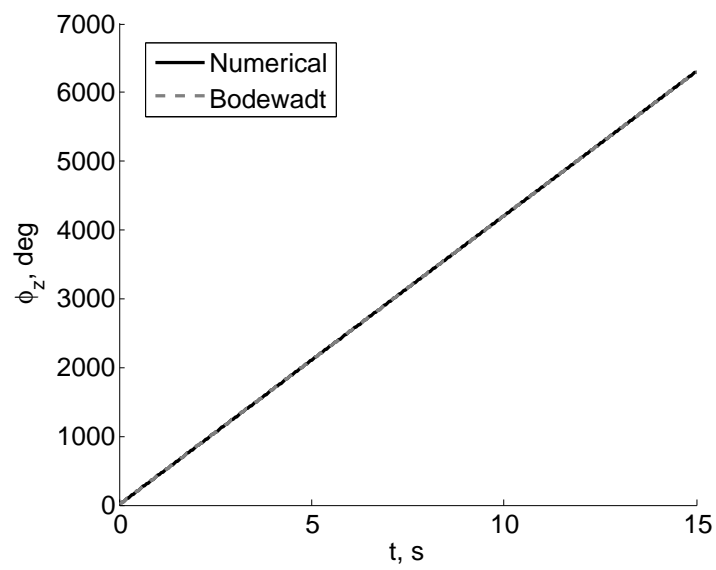
Figure 5.2. The numerical integration (black line) and the Bödewadt solution (gray dashed line) for ϕ_z are almost identical.

6. Conclusion and Future Work

6.1   Summary of Methodology and Results

6.1.1   Spinning Thrusting Spacecraft

Spin-stabilized rockets and assist modules are typically affected by center-of-mass offsets and misalignments of the thrusting engine, causing the intended velocity vector to have undesired pointing errors. Often high spin rates of the order of 70 rpm are required to maintain an acceptable pointing error. A major source of the pointing error is the step-function profile of the thruster history. If instead the thruster has a linear profile beginning at zero and gradually ramping up to maximum thrust, the pointing error may be greatly reduced. Alternatively, the linear profile can significantly reduce the required spin rate to achieve the same acceptable pointing error.

An analytical theory for the ramp-up and ramp-down schemes is developed. After integrating Euler's equations of motion and the kinematic equations, the inertial velocities are found. These inertial velocities are simplified to lead to a compact equation that captures the essential spacecraft behavior. Numerical tests have confirmed the accuracy of the theory. Simulations are provided for a hypothetical case involving a spin-stabilized spacecraft with a Payload Assist Module. The velocity pointing error for the ramp-up case is reduced by an order of magnitude. If the acceptable pointing error is the same as the constant thrust profile, the spin rate could be reduced by around 70% while maintaining the acceptable pointing error.

Implicit optimization could, in principle, be used to solve for the ramp-up profile which minimizes the velocity pointing error, but due to the oscillatory behavior of the velocity pointing error with respect to ramp-up time, no solution has been found. Instead heuristic solutions for ramp-up profiles are found which reduce the velocity pointing error further than the linear ramp-up profile. The tested sine pro-

files produce an order-of-magnitude improvement over a linear ramp-up profile while cosine, parabolic, exponential, logarithmic, and cubic profiles can produce up to two orders-of-magnitude improvement. In addition, these profiles result in more than three orders-of-magnitude improvement over the typical constant burn.

For small engine misalignment and offset, the velocity pointing error for cosine, parabolic, exponential, logarithmic, and cubic profiles is essentially zero. For an unknown thrust offset and misalignment, the cubic profile appears to be the best force profile to use. In the simulation shown here, choosing a ramp-up time around 11 seconds for different engine misalignment and offset results in velocity pointing errors which are either the minimum value or very close to the minimum.

6.1.2 Spinning Tethered Spacecraft

On long duration mission, some artificial gravity may be needed for human spaceflight. Instead of a rigid spacecraft with a large radius (and thus large mass), a tethered spacecraft can produce artificial gravity with the additional cost of a relatively low-mass tether. Instead of requiring the spacecraft to despin or reel in the tether for maneuvers, the spacecraft can have a thrust offset from the center of mass by balancing the magnitude of the thrust and the spin rate of the spacecraft.

Analytical theory has been developed for a spacecraft with constant and time-varying mass as well as for planar and non-planar thrust. These theories lead to similar relationships between the thrust and spin rate. Single and coupled spin-up maneuvers are also considered which find the required propellant to spin up to a specified artificial gravity level. The theory is applied to a round trip mission to Mars which results in a propellant mass reduction of over 1000 kg over the tethered spacecraft that needs to despin to perform the same maneuvers.

6.2   Future Work

6.2.1   High Fidelity Model of a Spinning, Thrusting Rocket

When applying the ramp-up scheme, the spacecraft modeled here is assumed to be a rigid body. A higher fidelity (i.e. more realistic) model of a spacecraft could be investigated to verify (or disprove) the effectiveness of the ramp-up scheme. Methods to increase the spacecraft's complexity include incorporating fuel sloshing into the spacecraft via spherical pendulums or modeling a more flexible spacecraft. To improve the robustness of the ramp-up scheme, the scheme could be applied to these models to determine if the velocity pointing errors will also decrease with a ramp-up profile instead of the typical constant force profile.

6.2.2   Method to Maintain Artificial Gravity for a Higher Fidelity Model of a Tethered Spacecraft

The tethered spacecraft modeled in Chapter 4 consists of two point masses attached by a massless tether. While the control scheme derived here is valid for this simplistic model, a more complex model will require a different control law. To find these control laws, a more complicated tether system could be used such as cylinders for the habitation and propulsion systems instead of point masses. The tether could also have mass and be flexible. These control schemes could also be applied to a system with relatively smaller end masses e.g. two tethered CubeSats.

6.3   Conclusion

An analytical theory is developed for the ramp-up and ramp-down schemes. The theory includes highly accurate, approximate solutions for the angular velocity, Euler angles, inertial velocity, and inertial displacement. The expressions involve secular and circular terms that are functions of the moments of inertia, initial spin rate, torques, forces, and time. Asymptotic solutions are derived from the general the-

ory which leads to compact, simple equations that capture the essential spacecraft behavior. Numerical simulations verify the accuracy of this analytical theory.

Ideally, implicit optimization would be used to solve for the ramp-up profile, but due to the complicated nature of the problem, no solution has been found. Instead heuristic solutions for ramp-up profiles are given here which drive the velocity pointing error to essentially zero. Current technology may not be able to duplicate ramp-up profiles starting at zero, but even with an initial non-zero thrust, ramp-up profiles, especially the cubic profile, decrease the velocity pointing error over the typical constant burn.

Most tethered spacecraft perform maneuvers with the thrust aligned with the center of mass either by despinning the spacecraft or by reeling in the tether. Here an analytical theory is presented which allows a tethered spacecraft with an offset thruster to perform large maneuvers while spinning by balancing the magnitude of the thrust and the spin rate of the spacecraft. Thus this new maneuver reduces mass and spacecraft complexity. The control needed to maintain the desired thrust direction can occur through a specific thrust history or a slight roll along the tether axis. A large amount of propellant mass is saved since the spacecraft spins continuously. Furthermore, this maneuver can lead to simpler spacecraft design since artificial gravity is always present and the spacecraft configuration is fixed during the maneuvers.

Lastly, a numerical study of the Bödewadt solution has shown that while the Bödewadt solution can predict ϕ_z fairly accurately for a spacecraft with changing spin, it is unable (even in the best case) to accurately predict the other attitude angles.

REFERENCES

REFERENCES

[1] E. Leimanis. *The General Problem of the Motion of Coupled Rigid Bodies About a Fixed Point*, chapter 11. Springer-Verlag, New York City, NY, second edition, 1965.

[2] J. B. Rosser, R. R. Newton, and G. L. Gross. *Mathematical Theory of Rocket Flight*, pages 49–262. McGraw-Hill, New York City, NY, 1947.

[3] K. Jarmolow. Dynamics of a spinning rocket with varying inertia and applied moment. *Journal of Applied Physics*, 28(3):308–313, 1957.

[4] Jr. L. Davis, Jr. J. W. Follin, and L. Blitzer. *Exterior Ballistics of Rockets*, chapter 9. D. Van Nostrand Co., Princeton, NJ, 1958.

[5] J. J. Buglia, G. R. Young, J. D. Timmons, and H. S. Brinkworth. Analytical methods of approximating the motion of a spinning vehicle with variable mass and inertia properties acted upon by several disturbing parameters. NASA TR R-110, Langley Research Center, Langley Air Force Base, VA, Jan. 1961.

[6] W. Martz. Method for approximating the vacuum motions of spinning symmetrical bodies with nonconstant spin rates. NASA TR R-115, Langley Research Center, Langley Station, Hampton, VA, Jan. 1961.

[7] K. Tsuchiya. Attitude behavior of a dual-spin spacecraft composed of asymmetric bodies. *Journal of Guidance, Control, and Dynamics*, 2(4):328–333, 1976.

[8] C. D. Hall and R. H. Rand. Spinup dynamics of axial dual-spin spacecraft. *Journal of Guidance, Control, and Dynamics*, 17(1):30–37, 1994.

[9] P. W. Likins. Attitude stability criteria for dual-spin spacecraft. *Journal of Spacecraft and Rockets*, 4(12):1638–1643, 1967.

[10] J. E. Cochran and P. H. Shu. Attitude motion of asymmetric dual-spin spacecraft. *Journal of Guidance, Control, and Dynamics*, 5(1):37–42, 1982.

[11] P. K. Winfree and J. E. Cochran. Nonlinear attitude motion of a dual-spin spacecraft containing spherical dampers. *Journal of Guidance, Control, and Dynamics*, 9(6):681–690, 1986.

[12] V. Larson and P. W. Likins. Closed-form solutions for the state equation for dual-spin and spinning spacecraft. *Journal of the Astronautical Sciences*, 21(5–6):244–251, 1974.

[13] J. M. Longuski, R. S. Campbell, and E. W. Klumpe. Error analysis for pulsed maneuvers of a dual-spin spacecraft. In *AAS/AIAA Astrodynamics Specialist Conference*, AAS Paper 89-396, Stowe, VT, Aug. 7–10 1989.

[14] R. Livneh and B. Wie. New results for an asymmetric rigid body with constant body-fixed torques. *Journal of Guidance, Control, and Dynamics*, 20(2):873–881, 1997.

[15] L. G. Kraige and J. L. Junkins. Perturbation formulations for satellite attitude dynamics. *Celestial Mechanics and Dynamical Astronomy*, 13(1):39–64, 1976.

[16] T. R. Kane and D. A. Levinson. Approximate description of attitude motions of a torque-free nearly axisymmetric rigid body. *Journal of the Astronautical Sciences*, 35(4):435–446, 1987.

[17] R. A. Gick, M. H. Williams, and J. M. Longuski. Floquet approximation for a nearly axisymmetric rigid body with constant transverse torque. *Journal of Guidance, Control, and Dynamics*, 22(5):658–663, 1999.

[18] R. A. Gick, M. H. Williams, and J. M. Longuski. Periodic solutions for a spinning axisymmetric rigid body with constant principal axis torque. *Journal of Guidance, Control, and Dynamics*, 23(5):781–788, 1999.

[19] L. G. Kraige and S. B. Skaar. A variation of parameters approach to the arbitrary torqued, asymmetric rigid body problem. *Journal of the Astronautical Sciences*, 25(3):207–226, 1977.

[20] J. C. van der Ha. Perturbation solution of attitude motion under body-fixed torques. *Acta Astronautica*, 12(10):861–869, 1985.

[21] J. M. Longuski. Real solutions for the attitude motion of a self-excited rigid body. *Acta Astronautica*, 25(3):131–140, 1991.

[22] P. Tsiotras and J. M. Longuski. A complex analytical solution for the attitude motion of a near-symmetric rigid body under body-fixed torques. *Celestial Mechanics and Dynamical Astronomy*, 51(3):281–301, 1991.

[23] M. Romano. Exact analytic solutions for the rotation of an axially symmetric rigid body subjected to a constant torque. *Celestial Mechanics and Dynamical Astronomy*, 101:375–390, 2008.

[24] J. M. Longuski and P. Tsiotras. Analytical solutions for a spinning rigid body subject to time-varying body-fixed torques, part I: Constant axial torque. *Journal of Applied Mechanics, Transactions of ASME*, 60(6):970–975, 1993.

[25] P. Tsiotras and J. M. Longuski. Analytical solutions for a spinning rigid body subject to time-varying body-fixed torques, part II: Time varying axial torque. *Journal of Applied Mechanics, Transactions of ASME*, 60(4):976–981, 1993.

[26] P. Tsiotras and J. M. Longuski. Analytical solution of euler's equations of motion for an asymmetric rigid body. *Journal of Applied Mechanics, Transactions of ASME*, 63(1):149–155, 1996.

[27] M. A. Ayoubi and J. M. Longuski. Analytical solutions for translational motion of spinning-up rigid bodies subject to constant body-fixed moments and forces. *Journal of Applied Mechanics, Transactions of ASME*, 75(1):310–320, 2008.

[28] M. A. Ayoubi and J. M. Longuski. Axial velocity solutions for spinning-up rigid bodies subject to constant forces. *Journal of Guidance, Control, and Dynamics*, 30(6):1610–1619, 2007.

[29] R. A. Beck and J. M. Longuski. Analytical solution for the velocity of a rigid body during spinning-up maneuvers. In *AIAA/AAS Astrodynamics Specialists Conference*, AIAA 94-3713, Scottsdale, AZ, Aug. 1–3 1994.

[30] R. A. Beck and J. M. Longuski. Annihilation of transverse velocity bias during spinning-up maneuvers. *Journal of Guidance, Control, and Dynamics*, 20(3):416–421, 1997.

[31] J. Ventura and M. Romano. Exact analytic solution for the spin-up manuever of an axially symmetric spacecraft. *Acta Astronautica*, 104(1):324–340, 2014.

[32] J. M. Longuski, R. A. Gick, M. A. Ayoubi, , and L. Randall. Analytical solutions for thrusting, spinning spacecraft subject to constant forces. *Journal of Guidance, Control, and Dynamics*, 28(6):1301–1308, 2005.

[33] M. A. Ayoubi, K. M. Martin, and J. M. Longuski. Analytical solution of the motion of spinning thrusting spacecraft with transverse ramp-up torques. *Journal of Guidance, Control, and Dynamics*, 37(4):1272–1282, 2014.

[34] R. S. Armstrong. Errors associated with spinning-up and thrusting symmetric rigid bodies. Technical Report No. 32-644, Jet Propulsion Laboratory, California Institute of Technology, Pasadena, CA, February 1965.

[35] J. M. Longuski, T. Kia, and W. G. Breckenridge. Annihilation of angular momentum bias during spinning-up and thrusting maneuvers. *Journal of the Astronautical Sciences*, 37(4):433–450, 1989.

[36] J. A. Oldenburg and S. G. Tragesser. Minimizing the effect of transverse torques during thrusting for spin-stabilized spacecraft. *Journal of Guidance, Control, and Dynamics*, 25(3):591–595, 2002.

[37] D. Javorsek and J. M. Longuski. Velocity pointing errors associated with spinning thrusting spacecraft. *Journal of Spacecraft and Rockets*, 37(3):359–365, 2000.

[38] R. R. Burton and L. J. Meeker. Physiologic validation of a short-arm centrifuge for space application. *Aviation, Space, and Environmental Medicine*, 63(9):476–481, 1992.

[39] D. D. Cardus. Artificial gravity in space and in medical research. *Journal of Gravitational Physiology*, 1(1):19–22, 1994.

[40] G. Clement and A. Pavy-Le Traon. Centrifugation as a countermeasure during actual and simulated microgravity: A review. *European Journal of Applied Physiology*, 92(3):235–248, 2004.

[41] G. Clement and A. Buckley. *Artificial Gravity*. Microcosm, Hawthorn, CA, 2007.

[42] J. R. Lackner and P. DiZio. Human orientation and movement control in weightless and artificial gravity environments. *Experiemntal Brain Research*, 130(1):2–26, 2000.

[43] L. R. Young. Artificial gravity considerations for a Mars exploration mission. *Annals of the New York Acamdey of Sciences*, 871(1):367–378, 1999.

[44] R. L. Kobric, S. Dara, J. Burley, and S. Gill. A new countermeasure device for long duration spaceflights. *Acta Astronautica*, 58(10):523–536, 2006.

[45] P. H. Diamonds. Countermeasures and artificial gravity. In S. Churchill, editor, *Fundamentals of Space Life Sciences*, volume 1, pages 159–175. Krieger, Melbourne, FL, 1997.

[46] P. DiZio, J. R. Lackener, and J. N. Evanoff. The influence of gravitoinertial force level on oculomotor and perceptual responses to Coriolis, cross-coupling stimulation. *Aviation, Space, and Environmental Medicine*, 58(9):A218–A223, 1987.

[47] J. R. Lackner and A. Graybiel. Elicitation of motion sickness by head movements in the microgravity phase of parabolic flight maneuvers. *Aviation, Space, and Environmental Medicine*, 55(6):513–520, 1984.

[48] J. R. Lackner and A. Graybiel. Head movements in low and high gravitoinertial force environments elicit motion sickness: Implications for the etiology of space motion sickness. *Aviation, Space, and Environmental Medicine*, 58(9):A212–A217, 1987.

[49] E. C. Lorenzini. A three-mass tethered system for micro-g/variable-g applications. *Journal of Guidance, Control, and Dynamics*, 10(3):242–249, 1987.

[50] Y. Ohkami, S. Yoshimura, and O. Okamoto. Evaluation of microgravity level fluctuation due to attitude/orbital motion in a tethered satellite system. *Acta Astronautica*, 35(2):187–191, 1995.

[51] S. Cho and N. H. McClamroch. Attitude control of a tethered satellite. In *Proceedings of the American Control Conference*, pages 1104–1109, Denver, CO, June 4–6 2003.

[52] G. A. Rauwolf, D. G. Pelaccio, S. Patel, and K. Sorensen. Mission performance of emerging in-space propulsion concepts for one-year crewed Mars missions. In *37th AIAA/ASME/SAE/ASEE Joint Propulsion Conference and Exhibit*, AIAA 2001-3374, Salt Lake City, UT, Uly 8–11 2001.

[53] M. P. Cartmell and D. J. McKenzie. A review of space tether research. *Progress in Aerospace Sciences*, 44(1):1–21, 2008.

[54] A. K. Misra and V. J. Modi. A survey of the dynamics and control of tethered satellite systems. In P. M. Bainum, I. Bekey, L. Guerriero, and P. A. Penzo, editors, *Advances in the Astronautical Sciences Series*, volume 62, pages 667–719, Arlington, VA, 1986. AAS, Univelt.

[55] M. L. Cosmo and E. C. Lorenzini, editors. *Tethers in Space Handbook*. NASA Marshall Space Flight Center and the Smithsonian Astrophysical Observatory, Cambridge, MA, third edition, 1997.

[56] M. D. Jokic and J. M. Longuski. Artificial gravity and abort scenarios via tethers for human missions to Mars. *Journal of Spacecraft and Rockets*, 42(5):883–889, 2005.

[57] S. K. Borowski, L. A. Dudzinski, and M. L. McGuire. Artificial gravity vehicle design option for NASA's human Mars mission using bimodal NTR propulsion. In *35th Joint Propulsion Conference*, AIAA Paper 1999-2545, Los Angeles, CA, June 20–24, 1999.

[58] M. L. McGuire, S. K. Borowski, L. M. Mason, and J. Gilland. High power MPD nuclear electric propulsion (NEP) for artificial gravity HOPE missions to Callisto. NASA TM-2003-212349, Washington, D.C., December 2003.

[59] M. G. Benton Sr. Spaceship discovery-vehicle architecture for human exploration of Moon, Mars, and beyond. In *Space 2006*, AIAA Paper 2006-7445, San Jose, CA, Sept. 19–21, 2006.

[60] J. M. Longuski. Galileo maneuver analysis. In *AAS/AIAA Astrodynamics Specialist Conference*, AAS 81-137, Lake Tahoe, Nevada, Aug. 3–5 1981.

[61] G. R. Hintz and J. M. Longuski. Error analysis for the delivery of a spinning probe to jupiter. *Journal of Guidance, Control, and Dynamics*, 8(3):384–390, 1985.

[62] J. M. Longuski and T. Kia. A parametric study of the behavior of the angular momentum vector during spin rate changes of rigid body spacecraft. *Journal of Guidance, Control, and Dynamics*, 7(3):295–300, 1984.

[63] C. C. Ih and E. H. McMahon II. Dynamic modeling and simulation study for galileo spacecraft pulsed-mode spin-up / 400 N main engine burn / spin-down maneuvers. In T.D. Guyenne, editor, *Proceedings of Space Mission Operations and Ground Data Systems*, ESA SP-394, pages 791–798, Munich, Germany, Sept. 16–20 1996. Paris, European Space Agency.

[64] D. F. Landau. Method to maintain artificial gravity during transfer maneuvers for tethered spacecraft. In *AIAA/AAS Astrodynamics Specialist Conference*, AIAA 2008-7499, Honolulu, HI, Aug. 18–21 2008.

[65] M. A. Ayoubi, D. Landau, and J. M. Longuski. Solution of spacecraft attitude via angular momentum in body and inertial frames. In *AAS/AIAA Astrodynamics Specialist Conference*, AAS 11-569, Girdwood, Alaska, July 31–Aug. 4 2011.

[66] D. T. Greenwood. *Principles of Dynamics*, pages 304–306, 390–391. Prentice Hall, Upper Saddle River, NJ, second edition, 1988.

[67] J. R. Wertz, editor. *Spacecraft Attitude Determination and Control*, pages 760–766. D. Reidel Publishing Company, Dordrecht, Holland, 2000.

[68] D. Javorsek and J. M. Longuski. Effect of thrust profile on velocity pointing errors of spinning spacecraft. In J. de Lafontaine, editor, *Advances in the Astronautical Sciences Series*, volume 116, pages 219–239, San Diego, 2003. AAS, Univelt. also AAS Paper 03-516.

[69] W. T. Thomson. *Introduction to Space Dynamics*, pages 223–227. Dover, New York City, NY, second edition, 1986.

[70] J. C. van der Ha and F. L. Jassens. Jet-damping and misalignment effects during solid-rocket motor burn. *Journal of Guidance, Control, and Dynamics*, 28(3):412–420, 2005.

[71] R. J. McCauley and S. R. Fischbach. Controllable solid propulsion combustion and acoustic knowledge base improvements. In *59th Joint Army, Navy, NASA, and Air Force Propulsion Meeting*, Paper 2012-2457, San Antonio, TX, Apr. 30–May 4 2012.

[72] S. A. Whitmore, Z. W. Peterson, and S. D. Eilers. Deep throttle of a nitrous oxide and hydroxyl-terminated polybutadiene hybrid rocket motor. *Journal of Propulsion and Power*, 30(1):78–86, 2014.

[73] M. J. Casiano, J. R. Hulka, and V. Yang. Liquid-propellant rocket engine throttling a comprehensive review. *Journal of Propulsion and Power*, 26(5):897–923, 2010.

[74] G. A. Dressler. Summary of deep throttling rocket engines with emphasis on Apollo LMDE. In *42nd Joint Propulsion Conference*, AIAA Paper 2006-5220, Sacramento, CA, July 9–12 2006.

[75] J. P. Wanhainen, R. J. Antl, N. P. Hannum, and A. H. Mansour. Throttling characteristics of a hydrogen-oxygen, regeneratively cooled, pump-fed rocket engine. NASA TM X-1043, NASA, Washington, D.C., December 1964.

[76] V. S. Rachuk, A. V. Shostak, A. I. Bmitrenko, G. I. Goncharov, R. Hernadex, R. G. Starle, and J. Hulka. Benchmark testing of an enhanced operability LO2/LH2 RD-0120 engine. In *32nd Joint Propulsion Conference*, AIAA Paper 96-26090, Buena Vista, FL, July 1–3 1996.

[77] M. A. Bradley. SSME off-nominal low power level operation. In *33nd Joint Propulsion Conference*, AIAA Paper 1997-2685, Seattle, WA, July 6–9 1997.

[78] J. M. Gromski, A. N. Majamaki, S. G. Chianese, V. D. Weinstock, and T. S. Kim. Northrop grumman TR202 LOX/LH2 deep throttling engine technology project status. In *46th Joint Propulsion Conference*, AIAA Paper 2010-6725, Nashville, TN, July 25–28 2010.

[79] V. J. Giuliano, T. G. Leonard, R. T. Lyda, and T. S. Kim. CECE: Expanding the envelope of deep throttling technology in liquid oxygen/liquid hydrogen rocket engines for NASA exploration missions. In *46th Joint Propulsion Conference*, AIAA Paper 2010-6724, Nashville, TN, July 25–28 2010.

[80] Jr. B. L. Austin, S. D. Heister, E. M. Dambach, S. E. Meyer, and E. J. Wemimont. Variable thrust, multiple start hybrid motor solutions for missile and space applications. In *46th Joint Propulsion Conference*, AIAA Paper 2010-7121, Nashville, TN, July 25–28 2010.

[81] T. C. Tsu. Interplanetary travel by solar sail. *ARS Journal*, 29(6):422–427, 1959.

[82] S. A. Belknap. A general transport rule for variable mass dynamics. *AIAA Journal*, 10(9):1137–1138, 1972.

[83] J. Niehoff, A. Friedlander, and J. McAdams. Earth-Mars transport cycler concepts. In *International Astronautical Congress*, IAF Paper 91-438, Montreal, Canada, Oct. 5–11, 1991.

[84] R. D. Reed and G. R. Coulter. Physiology of spaceflight. In W. J. Larson and L. K. Pranke, editors, *Human Spaceflight Mission Analysis and Design*, chapter 5. McGraw-Hill, New York City, NY, 1999.

[85] U. T. Bödewadt. Der symmetrische kreisel bei zeitfester drehkraft. *Mathematische Zeitschrift*, 55(3):310–320, 1952.

[86] J. M. Longuski. On the attitude motion of a self-excited body. *Journal of the Astronautical Sciences*, 32(4):463–473, 1984.

[87] E. A. Coddington and R. Carlson. *Linear Ordinary Differential Equations*, chapter 3. SIAM, Philadelphia, PA, 1997.

[88] H. J. Kelley. A second variation test for singular extremals. *AIAA Journal*, 2(8):1380–1382, 1964.

APPENDICES

A. Coefficients for Displacement and Velocity Solutions

The coefficients for the velocity and displacement solutions are listed in the following sections. For clarity, the X-axis coefficients all begin with A, the Y-axis coefficients begin with B, and the Z-axis coefficients begin with C. The coefficients starting with f_0 are the constants in the force equations, and the coefficients starting with f_1 are the constants multiplied by t in the force equations. The same is true of the coefficients beginning with c which relate to the torques.

A.1   X-Axis Constants for Inertial Velocity and Displacement Solutions

$$
\begin{aligned}
A_0 =& \frac{c_{0x} f_{0z} \left[I_y k_y + I_x \left(k^2 - 2 \right) \right]}{m I_x I_z \left(k^2 - 1 \right) \omega_{z0}^3} - \frac{c_{1y} f_{0z} \left[I_x k_x + I_y \left(2k^2 - 3 \right) \right]}{m I_y I_z \left(k^2 - 1 \right) \omega_{z0}^4} \\
& - \frac{c_{1x} f_{1z} \left[2 I_y k_y \left(k^2 - 2 \right) + I_x \left(6 - 7k^2 + 3k^4 \right) \right]}{m I_x I_z \left(k^2 - 1 \right)^2 \omega_{z0}^5} \\
& - \frac{c_{0y} f_{1z} \left[I_x k_x \left(k^2 - 3 \right) + I_y \left(3 - 2k^2 + k^4 \right) \right]}{m I_y I_z \left(k^2 - 1 \right)^2 \omega_{z0}^4} \\
& - \frac{f_{1x} + f_{0y} \omega_{z0}}{m \omega_{z0}^2} + \frac{\omega_{x0} f_{1z} \left[I_x - \left(3 I_y - I_z \right) k_y \right]}{m I_z \left(k^2 - 1 \right)^2 \omega_{z0}^3} + \frac{\omega_{y0} f_{0z} \left(I_z - 2 I_y \right)}{m I_z \left(k^2 - 1 \right) \omega_{z0}^2}
\end{aligned}
\tag{A.1}
$$

$$
A_t = -\frac{f_{0z} \left(c_{1x} + c_{0y} \omega_{z0} - I_x \omega_{x0} \omega_{z0}^2 \right)}{m I_z \omega_{z0}^3}, \quad A_{tt} = -\frac{f_{1z} \left(c_{1x} + c_{0y} \omega_{z0} - I_x \omega_{x0} \omega_{z0}^2 \right)}{2 m I_z \omega_{z0}^3}
\tag{A.2}
$$

$$
\begin{aligned}
A_{c0} =& \frac{c_{1y} f_{0z} \left[\left(2 I_z - I_x \right) k_x - I_y \right]}{m I_y I_z k^2 \omega_{z0}^4} - \frac{f_{0z} c_{0x}}{m I_x k_x \omega_{z0}^3} + \frac{f_{1x} + f_{0y} \omega_{z0}}{m \omega_{z0}^2} + \frac{c_{0y} f_{1z}}{m I_y k_y \omega_{z0}^4} \\
& + \frac{c_{1x} f_{1z} \left[\left(3 I_z - I_y \right) k_y - I_x \right]}{m I_x I_z k^2 \omega_{z0}^5}
\end{aligned}
\tag{A.3}
$$

$$
A_{ct} = -\frac{c_{1x} f_{0z} + c_{0x} f_{1z}}{m I_x k_x \omega_{z0}^3} + \frac{c_{1y} f_{1z} \left[\left(3 I_z - I_x \right) k_x - I_y \right]}{m I_y I_z k^2 \omega_{z0}^4} + \frac{f_{1y}}{m \omega_{z0}}
\tag{A.4}
$$

$$
A_{ctt} = -\frac{c_{1x} f_{1z}}{m I_x k_x w_{z0}^3}
\tag{A.5}
$$

$$A_{cc} = \frac{f_{1z}\left(c_{1x}I_y - c_{0y}I_x k_x \omega_{z0} - I_x I_y k^2 \omega_{z0}^2 \omega_{x0}\right)\left[I_x - (3I_y - I_z)\,k_y\right]}{mI_x I_y I_z k^2 \left(k^2 - 1\right)^2 \omega_{z0}^5}$$
$$+ \frac{f_{0z}\left(c_{1y}I_x + c_{0x}I_y k_y \omega_{z0} - I_x I_y k^2 \omega_{z0}^2 \omega_{y0}\right)\left(I_x k_x - I_y\right)}{mI_x I_y I_z k^2 \left(k^2 - 1\right) \omega_{z0}^4} \tag{A.6}$$

$$A_{cct} = \frac{f_{1z}\left(c_{1y}I_x + c_{0x}I_y k_y \omega_{z0} - I_x I_y k^2 \omega_{z0}^2 \omega_{y0}\right)\left(I_x k_x - I_y\right)}{mI_x I_y I_z k^2 \left(k^2 - 1\right) \omega_{z0}^4} \tag{A.7}$$

$$A_{cs} = -\frac{f_{1z}\left(c_{1y}I_x + c_{0x}\omega_{z0}I_y k_y - I_x I_y k^2 \omega_{z0}^2 \omega_{y0}\right)\left[I_x - (3I_y - I_z)\,k_y\right]}{mI_x I_y I_z k k_y \left(k^2 - 1\right)^2 \omega_{z0}^5}$$
$$+ \frac{f_{0z}\left(c_{1x}I_y - c_{0y}I_x k_x \omega_{z0} - I_x I_y k^2 \omega_{z0}^2 \omega_{x0}\right)\left(I_x k_x - I_y\right)}{mI_x I_y I_z k k_x \left(k^2 - 1\right) \omega_{z0}^4} \tag{A.8}$$

$$A_{cst} = \frac{f_{1z}\left(c_{1x}I_y - c_{0y}I_x k_x \omega_{z0} - I_x I_y k^2 \omega_{z0}^2 \omega_{x0}\right)\left(I_x k_x - I_y\right)}{mI_x I_y I_z k k_x \left(k^2 - 1\right) \omega_{z0}^4} \tag{A.9}$$

$$A_{s0} = \frac{c_{1x}f_{0z}\left(2k_y - 1\right)}{mI_x k^2 \omega_{z0}^4} + \frac{f_{1z}c_{0x}}{mI_x k_x \omega_{z0}^4} + \frac{c_{0y}f_{0z}}{mI_y k_y \omega_{z0}^3}$$
$$+ \frac{f_{0x}\omega_{z0} - f_{1y}}{m\omega_{z0}^2} - \frac{c_{1y}f_{1z}\left(3k_x - 1\right)}{mI_y k^2 \omega_{z0}^5} \tag{A.10}$$

$$A_{st} = \frac{c_{1x}f_{1z}\left(3k_y - 1\right)}{mI_x k^2 \omega_{z0}^4} + \frac{c_{0y}f_{1z} + c_{1y}f_{0z}}{mI_y k_y \omega_{z0}^3} + \frac{f_{1x}}{m\omega_{z0}} \tag{A.11}$$

$$A_{stt} = \frac{c_{1y}f_{1z}}{mI_y k_y \omega_{z0}^3} \tag{A.12}$$

$$A_{sc} = \frac{f_{1z}\left(c_{1y}I_x + c_{0x}k_y \omega_{z0} - I_x I_y k^2 \omega_{z0}^2 \omega_{y0}\right)\left[(3I_x - I_z)\,k_x - I_y\right]}{mI_x I_y I_z k^2 \left(k^2 - 1\right)^2 \omega_{z0}^5}$$
$$+ \frac{f_{0z}\left(-c_{1x}I_y + c_{0y}I_x k_x \omega_{z0} + I_x I_y k^2 \omega_{z0}^2 \omega_{x0}\right)\left(I_x - I_y k_y\right)}{mI_x I_y I_z k^2 \left(k^2 - 1\right) \omega_{z0}^4} \tag{A.13}$$

$$A_{sct} = \frac{f_{1z}\left(-c_{1x}I_y + c_{0y}I_x k_x \omega_{z0} + I_x I_y k^2 \omega_{z0}^2 \omega_{x0}\right)\left(I_x - I_y k_y\right)}{mI_x I_y I_z k^2 \left(k^2 - 1\right) \omega_{z0}^4} \tag{A.14}$$

$$A_{ss} = \frac{f_{1z}\left(-c_{1x}I_y + c_{0y}I_x k_x \omega_{z0} + I_x I_y k^2 \omega_{z0}^2 \omega_{x0}\right)\left[I_y - (3I_x - I_z)\,k_x\right]}{mI_x I_y I_z k k_x \left(k^2 - 1\right)^2 \omega_{z0}^5}$$
$$+ \frac{f_{0z}\left(c_{1y}I_x + c_{0x}I_y k_y \omega_{z0} - I_x I_y k^2 \omega_{z0}^2 \omega_{y0}\right)\left(I_x - I_y k_y\right)}{mI_x I_y I_z k k_y \left(k^2 - 1\right) \omega_{z0}^4} \tag{A.15}$$

$$A_{sst} = \frac{f_{1z}\left(c_{1y}I_x + c_{0x}I_y k_y \omega_{z0} - I_x I_y k^2 \omega_{z0}^2 \omega_{y0}\right)\left(I_x - I_y k_y\right)}{mI_x I_y I_z k k_y \left(k^2 - 1\right) \omega_{z0}^4} \tag{A.16}$$

A.2   Y-Axis Constants for Inertial Velocity and Displacement Solutions

$$B_0 = -\frac{c_{1y}f_{1z}\left[2I_x k_x\left(k^2 - 2\right) + I_y\left(6 - 7k^2 + 3k^4\right)\right]}{mI_yI_z\left(k^2 - 1\right)^2\omega_{z0}^5}$$
$$+ \frac{c_{0y}f_{0z}\left[I_x k_x + I_y\left(k^2 - 2\right)\right]}{mI_yI_z\left(k^2 - 1\right)\omega_{z0}^3} + \frac{c_{1x}f_{0z}\left[I_y k_y + I_x\left(2k^2 - 3\right)\right]}{mI_xI_z\left(k^2 - 1\right)\omega_{z0}^4}$$
$$+ \frac{c_{0x}f_{1z}\left[I_y k_y\left(k^2 - 3\right) + I_x\left(3 - 2k^2 + k^4\right)\right]}{mI_xI_z\left(k^2 - 1\right)^2\omega_{z0}^4}$$
$$+ \frac{f_{0x}\omega_{z0} - f_{1y}}{m\omega_{z0}^2} + \frac{\omega_{y0}f_{1z}\left[I_y - \left(3I_x - I_z\right)k_x\right]}{mI_z\left(k^2 - 1\right)^2\omega_{z0}^3} + \frac{\omega_{x0}f_{0z}\left(2I_x - I_z\right)}{mI_z\left(k^2 - 1\right)\omega_{z0}^2} \tag{A.17}$$

$$B_t = -\frac{f_{0z}\left(c_{1y} - c_{0x}\omega_{z0} - I_y\omega_{z0}^2\omega_{y0}\right)}{mI_z\omega_{z0}^3}, \quad B_{tt} = -\frac{f_{1z}\left(c_{1y} - c_{0x}\omega_{z0} - I_y\omega_{z0}^2\omega_{y0}\right)}{2mI_z\omega_{z0}^3} \tag{A.18}$$

$$B_{c0} = -\frac{c_{1x}f_{0z}\left(2k_y - 1\right)}{mI_x k^2\omega_{z0}^4} - \frac{f_{0z}c_{0y}}{mI_y k_y\omega_{z0}^3} + \frac{f_{1y} - f_{0x}\omega_{z0}}{m\omega_{z0}^2} - \frac{c_{0x}f_{1z}}{mI_x k_x\omega_{z0}^4}$$
$$+ \frac{c_{1y}f_{1z}\left(3k_x - 1\right)}{mI_y k^2\omega_{z0}^5} \tag{A.19}$$

$$B_{ct} = -\frac{c_{1y}f_{0z} + c_{0y}f_{1z}}{mI_y k_y\omega_{z0}^3} - \frac{c_{1x}f_{1z}\left(3k_y - 1\right)}{mI_x k^2\omega_{z0}^4} - \frac{f_{1x}}{m\omega_{z0}} \tag{A.20}$$

$$B_{ctt} = -\frac{c_{1y}f_{1z}}{mI_y k_y\omega_{z0}^3} \tag{A.21}$$

$$B_{cc} = \frac{f_{1z}\left(c_{1y}I_x + c_{0x}I_y k_y\omega_{z0} - I_xI_y k^2\omega_{z0}^2\omega_{y0}\right)\left[I_y - \left(3I_x - I_z\right)k_x\right]}{mI_xI_yI_z k^2\left(k^2 - 1\right)^2\omega_{z0}^5}$$
$$+ \frac{f_{0z}\left(c_{1x}I_y - c_{0y}I_x k_x\omega_{z0} - I_xI_y k^2\omega_{z0}^2\omega_{x0}\right)\left(I_x - I_y k_y\right)}{mI_xI_yI_z k^2\left(k^2 - 1\right)\omega_{z0}^4} \tag{A.22}$$

$$B_{cct} = \frac{f_{1z}\left(c_{1x}I_y - c_{0y}I_x k_x\omega_{z0} - I_xI_y k^2\omega_{z0}^2\omega_{x0}\right)\left(I_x - I_y k_y\right)}{mI_xI_yI_z k^2\left(k^2 - 1\right)\omega_{z0}^4} \tag{A.23}$$

$$B_{cs} = \frac{f_{1z}\left(c_{1x}I_y - c_{0y}\omega_{z0}I_x k_x - I_xI_y k^2\omega_{z0}^2\omega_{x0}\right)\left[I_y - \left(3I_x - I_z\right)k_x\right]}{mI_xI_yI_z k k_x\left(k^2 - 1\right)^2\omega_{z0}^5}$$
$$+ \frac{f_{0z}\left(c_{1y}I_x + c_{0x}I_y k_y\omega_{z0} - I_xI_y k^2\omega_{z0}^2\omega_{y0}\right)\left(I_y k_y - I_x\right)}{mI_xI_yI_z k k_y\left(k^2 - 1\right)\omega_{z0}^4} \tag{A.24}$$

$$B_{cst} = \frac{f_{1z}\left(c_{1y}I_x + c_{0x}I_y k_y\omega_{z0} - I_xI_y k^2\omega_{z0}^2\omega_{y0}\right)\left(I_y k_y - I_x\right)}{mI_xI_yI_z k k_y\left(k^2 - 1\right)\omega_{z0}^4} \tag{A.25}$$

$$B_{s0} = \frac{c_{1y}f_{0z}\left(2k_x - 1\right)}{mI_y k^2\omega_{z0}^4} - \frac{f_{0z}c_{0x}}{mI_x k_x\omega_{z0}^3} + \frac{f_{1x} + f_{0y}\omega_{z0}}{m\omega_{z0}^2} + \frac{c_{0y}f_{1z}}{mI_y k_y\omega_{z0}^4}$$
$$+ \frac{c_{1x}f_{1z}\left(3k_y - 1\right)}{mI_xI_z k^2\omega_{z0}^5} \tag{A.26}$$

$$B_{st} = -\frac{c_{1x}f_{0z} + c_{0x}f_{1z}}{mI_x k_x \omega_{z0}^3} + \frac{c_{1y}f_{1z}\left(3k_x - 1\right)}{mI_y k^2 \omega_{z0}^4} + \frac{f_{1y}}{m\omega_{z0}} \tag{A.27}$$

$$B_{stt} = -\frac{c_{1x}f_{1z}}{mI_x k_x \omega_{z0}^3} \tag{A.28}$$

$$B_{sc} = \frac{f_{1z}\left(-c_{1x}I_y + c_{0y}I_x k_x \omega_{z0} + I_x I_y k^2 \omega_{z0}^2 \omega_{x0}\right)\left[\left(3I_y - I_z\right)k_y - I_x\right]}{mI_x I_y I_z k^2 \left(k^2 - 1\right)^2 \omega_{z0}^5}$$
$$+ \frac{f_{0z}\left(c_{1y}I_x + c_{0x}I_y k_y \omega_{z0} - I_x I_y k^2 \omega_{z0}^2 \omega_{y0}\right)\left(I_x k_x - I_y\right)}{mI_x I_y I_z k^2 \left(k^2 - 1\right)\omega_{z0}^4} \tag{A.29}$$

$$B_{sct} = \frac{f_{1z}\left(c_{1y}I_x + c_{0x}I_y k_y \omega_{z0} - I_x I_y k^2 \omega_{z0}^2 \omega_{y0}\right)\left(I_x k_x - I_y\right)}{mI_x I_y I_z k^2 \left(k^2 - 1\right)\omega_{z0}^4} \tag{A.30}$$

$$B_{ss} = \frac{f_{1z}\left(c_{1y}I_x + c_{0x}I_y k_y \omega_{z0} - I_x I_y k^2 \omega_{z0}^2 \omega_{y0}\right)\left[\left(3I_y - I_z\right)k_y - I_x\right]}{mI_x I_y I_z k k_y \left(k^2 - 1\right)^2 \omega_{z0}^5}$$
$$+ \frac{f_{0z}\left(c_{1x}I_y - c_{0y}I_x k_x \omega_{z0} - I_x I_y k^2 \omega_{z0}^2 \omega_{x0}\right)\left(I_x k_x - I_y\right)}{mI_x I_y I_z k k_x \left(k^2 - 1\right)\omega_{z0}^4} \tag{A.31}$$

$$B_{sst} = \frac{f_{1z}\left(c_{1x}I_y - c_{0y}I_x k_x \omega_{z0} - I_x I_y k^2 \omega_{z0}^2 \omega_{x0}\right)\left(I_x k_x - I_y\right)}{mI_x I_y I_z k k_x \left(k^2 - 1\right)\omega_{z0}^4} \tag{A.32}$$

A.3 Z-Axis Constants for Inertial Velocity and Displacement Solutions

$$C_0 = \frac{\left(c_{0x}f_{1y} - c_{1x}f_{0y}\right)\left(I_y + I_x k^2 k_x\right)}{mI_x I_z k^2 k_x \omega_{z0}^4} + \frac{\left(c_{1y}f_{0x} - c_{0y}f_{1x}\right)\left(I_x + I_y k^2 k_y\right)}{mI_y I_z k^2 k_y \omega_{z0}^4}$$
$$- \frac{\left(c_{0x}f_{0x} + c_{0y}f_{0y} - f_{1x}I_x \omega_{x0} - f_{1y}I_y \omega_{y0}\right)\left(k^2 - 1\right)}{mI_z k^2 \omega_{z0}^3}$$
$$- \frac{\left(c_{1x}f_{1x} + c_{1y}f_{1y}\right)\left(k^4 - 1\right)}{mI_z k^4 \omega_{z0}^5} + \frac{f_{0y}k_y \omega_{x0} - f_{0x}k_x \omega_{y0}}{mk^2 \omega_{z0}^2} \tag{A.33}$$

$$C_t = \frac{f_{0z}}{m} - \frac{\left(c_{1x}f_{0x} + c_{1y}f_{0y}\right)\left(k^2 - 1\right)}{mI_z k^2 \omega_{z0}^3} + \frac{c_{0x}f_{0y}}{mI_x k_x \omega_{z0}^2} - \frac{c_{0y}f_{0x}}{mI_y k_y \omega_{z0}^2} \tag{A.34}$$

$$C_{tt} = \frac{f_{1z}}{2m} + \frac{c_{1x}f_{0y} + c_{0x}f_{1y}}{2mI_x k_x \omega_{z0}^2} - \frac{c_{1y}f_{0x} + c_{0y}f_{1x}}{2mI_y k_y \omega_{z0}^2} - \frac{\left(c_{1x}f_{1x} + c_{1y}f_{1y}\right)\left(k^2 - 1\right)}{2mI_z k^2 \omega_{z0}^3} \tag{A.35}$$

$$C_{ttt} = \frac{c_{1x}f_{1y}}{3mI_x k_x \omega_{z0}^2} - \frac{c_{1y}f_{1x}}{3mI_y k_y \omega_{z0}^2} \tag{A.36}$$

$$C_c = \frac{c_{1x}f_{0y} - c_{1y}f_{0x} + \left(c_{0x}f_{0x} + c_{0y}f_{0y}\right)\omega_{z0}}{mI_z \omega_{z0}^4}$$
$$+ \frac{c_{1x}f_{1x} + c_{1y}f_{1y} + \left(c_{0y}f_{1x} - c_{0x}f_{1y}\right)\omega_{z0}}{mI_z \omega_{z0}^5}$$
$$- \frac{f_{1x}I_x \omega_{x0} + f_{1y}I_y \omega_{y0}}{mI_z \omega_{z0}^3} + \frac{f_{0x}I_y \omega_{y0} - f_{0y}I_x \omega_{x0}}{mI_z \omega_{z0}^2} \tag{A.37}$$

$$C_{ct} = \frac{c_{1x}f_{1y} - c_{1y}f_{1x} + (c_{0x}f_{1x} + c_{0y}f_{1y})\,\omega_{z0}}{mI_z\omega_{z0}^4} + \frac{f_{1x}I_y\omega_{y0} - f_{1y}I_x\omega_{x0}}{mI_x\omega_{z0}^2} \qquad (A.38)$$

$$\begin{aligned}
C_{ck} = &- \frac{c_{0x}f_{0x} + c_{0y}f_{0y} - f_{1x}I_x\omega_{x0} - f_{1y}I_y\omega_{y0}}{mI_zk^2\omega_{z0}^3} - \frac{c_{1x}f_{1x} + c_{1y}f_{1y}}{mI_zk^4\omega_{z0}^5} \\
&+ \frac{(c_{1x}f_{0y} - c_{0x}f_{1y})\,I_y}{mI_xI_zk^2k_x\omega_{z0}^4} + \frac{(c_{0y}f_{1x} - c_{1y}f_{0x})\,I_x}{mI_yI_zk^2k_y\omega_{z0}^4} \\
&+ \frac{f_{0x}I_xk_x\omega_{y0} - f_{0y}I_yk_y\omega_{x0}}{mI_zk^2\omega_{z0}^2}
\end{aligned} \qquad (A.39)$$

$$\begin{aligned}
C_{ckt} = &- \frac{c_{0x}f_{1x} + c_{0y}f_{1y}}{mI_zk^2\omega_{z0}^3} + \frac{c_{1x}f_{1y}I_y}{mI_xI_zk^2k_x\omega_{z0}^4} - \frac{c_{1y}f_{1x}I_x}{mI_yI_zk^2k_y\omega_{z0}^4} \\
&+ \frac{f_{1x}I_xk_x\omega_{y0} - f_{1y}I_yk_y\omega_{x0}}{mI_zk^2\omega_{z0}^2}
\end{aligned} \qquad (A.40)$$

$$\begin{aligned}
C_s = &\frac{c_{1x}f_{0x} + c_{1y}f_{0y} + (c_{0y}f_{0x} - c_{0x}f_{0y})\,\omega_{z0}}{mI_z\omega_{z0}^4} - \frac{f_{0x}I_x\omega_{x0} + f_{0y}I_y\omega_{y0}}{mI_z\omega_{z0}^2} \\
&+ \frac{c_{1y}f_{1x} - c_{1x}f_{1y} - (c_{0x}f_{1x} + c_{0y}f_{1y})\,\omega_{z0}}{mI_z\omega_{z0}^5} + \frac{f_{1y}I_x\omega_{x0} - f_{1x}I_y\omega_{y0}}{mI_z\omega_{z0}^3}
\end{aligned} \qquad (A.41)$$

$$C_{st} = \frac{c_{1x}f_{1x} + c_{1y}f_{1y} + (c_{0y}f_{1x} - c_{0x}f_{1y})\,\omega_{z0}}{mI_z\omega_{z0}^4} - \frac{f_{1x}I_x\omega_{x0} + f_{1y}I_y\omega_{y0}}{mI_z\omega_{z0}^2} \qquad (A.42)$$

$$\begin{aligned}
C_{sk} = &\frac{c_{0x}f_{1x} + c_{0y}f_{1y} - c_{1x}f_{0x} - c_{1y}f_{0y}}{mI_zk^3\omega_{z0}^4} - \frac{c_{0x}f_{0y}I_y}{mI_xI_zkk_x\omega_{z0}^3} \\
&+ \frac{c_{0y}f_{0x}I_x}{mI_yI_zkk_y\omega_{z0}^3} - \frac{c_{1x}f_{1y}I_y}{mI_xI_zk^3k_x\omega_{z0}^5} + \frac{c_{1y}f_{1x}I_x}{mI_yI_zk^3k_y\omega_{z0}^5} \\
&+ \frac{f_{1y}I_yk_y\omega_{x0} - f_{1x}I_xk_x\omega_{y0}}{mI_zk^3\omega_{z0}^3} + \frac{f_{0x}I_x\omega_{x0} + f_{0y}I_y\omega_{y0}}{mI_zk\omega_{z0}^2}
\end{aligned} \qquad (A.43)$$

$$\begin{aligned}
C_{skt} = &\frac{c_{1x}f_{1x} + c_{1y}f_{1y}}{mI_zk^3\omega_{z0}^4} - \frac{c_{0x}f_{1y}I_y}{mI_xI_zkk_x\omega_{z0}^3} + \frac{c_{0y}f_{1x}I_x}{mI_yI_zkk_y\omega_{z0}^3} \\
&+ \frac{f_{1x}I_x\omega_{x0} + f_{1y}I_y\omega_{y0}}{mI_zk\omega_{z0}^2}
\end{aligned} \qquad (A.44)$$

B. Two-Point Boundary-Value Problem for Heuristic Ramp-up

To justify using heuristic solutions to minimize the pointing error, a two-point boundary-value problem (TPBVP) is set-up to determine if an implicit solution can be found. To simplify the equations as much as possible, the thruster misalignment, α, is assumed to be zero. Furthermore, the only torque is M_x and the only forces are f_z and f_y similar to the Ulysses simulation in this paper.

B.1   State Equations

To simplify further, a few additional assumptions were made. The spacecraft is axisymmetric so that the third equation in Eq. (2.1) simply becomes ω_z is constant. Also ϕ_x, ϕ_y, and the product $\phi_y\omega_x$ are assumed to be small so that Eq. (3.10) becomes

$$
\begin{aligned}
\dot{\phi}_x &= \omega_x + \omega_{z0}\phi_y \\
\dot{\phi}_y &= \omega_y - \omega_{z0}\phi_x \\
\dot{\phi}_z &= \omega_{z0}
\end{aligned}
\tag{B.1}
$$

Then clearly

$$
\phi_z = \omega_{z0}t
\tag{B.2}
$$

With these assumptions, Eq. (2.13) becomes

$$
{}^{I}\mathbf{R}^{B}_{312} =
\begin{bmatrix}
\cos\omega_{z0}t & -\sin\omega_{z0}t & \phi_y cos\omega_{z0}t + \phi_x cos\phi_{z0}t \\
\sin\omega_{z0}t & \cos\omega_{z0}t & \phi_y sin\omega_{z0}t - \phi_x cos\omega_{z0}t \\
-\phi_y & \phi_x & 1
\end{bmatrix}
\tag{B.3}
$$

The acceleration is then found by

$$
\begin{Bmatrix} \Delta\dot{V}_X \\ \Delta\dot{V}_Y \\ \Delta\dot{V}_Z \end{Bmatrix} = {}^{I}\mathbf{R}^{B}_{312} \begin{Bmatrix} f_x/m \\ f_y/m \\ f_z/m \end{Bmatrix} = {}^{I}\mathbf{R}^{B}_{312} \begin{Bmatrix} 0 \\ 0 \\ F/m \end{Bmatrix}
$$
(B.4)

Since ϕ_z and ω_z are known, the TPBVP has seven states which are

$$
\begin{aligned}
\dot{\omega}_x &= M_x/I_x - k\omega_y\omega_{z0} = Fd/I_x - k\omega_y\omega_{z0} \\
\dot{\omega}_y &= k\omega_{z0}\omega_x \\
\dot{\phi}_x &= \omega_x + \phi_y\omega_{z0} \\
\dot{\phi}_y &= \omega_y - \phi_x\omega_{z0} \\
\Delta\dot{V}_X &= F/m(\phi_y\cos\omega_{z0}t + \phi_x\sin\omega_{z0}t) \\
\Delta\dot{V}_Y &= F/m(\phi_y\sin\omega_{z0}t - \phi_x\cos\omega_{z0}t) \\
\Delta\dot{V}_Z &= F/m
\end{aligned}
$$
(B.5)

where

$$
k = \frac{I_z - I_x}{I_y} = \frac{I_z - I_y}{I_x}
$$
(B.6)

B.2   Cost Function

Ideally, the cost function would be the velocity pointing error at the end of Phase 2, but the state equations only apply to Phase 1. By including the state equations from Phase 2, the costate equation formulation would involve two different Hamiltonians. Usually when faced with two sets of governing differential equations, an analytical solution is found for the second set of equations and substituted into the cost function so that the cost function becomes a function of the final state of the first set of differential equations. In this case, the Phase 2 equations are analytically intractable. Instead, only Phase 1 is considered. To simplify the cost equation, the cost function is the ending velocity pointing error at the end of Phase 1 or

$$
\rho_f = \sqrt{\rho_{Xf}^2 + \rho_{Yf}^2} = \sqrt{\frac{\Delta V_{Xf}^2 + \Delta V_{Yf}^2}{\Delta V_{Zf}^2}}
$$
(B.7)

Since the ending Z-velocity is positive, the Mayer problem can be written as

$$\text{Min } J = \frac{\sqrt{\Delta V_{Xf}^2 + \Delta V_{Yf}^2}}{\Delta V_{Zf}} \tag{B.8}$$

B.3 Hamiltonian

The Hamiltonian is defined as

$$H = L + \lambda^\mathsf{T} \dot{\vec{x}} \tag{B.9}$$

where L is the Lagrangian, λ is the costate vector, and

$$\dot{\vec{x}} = \begin{Bmatrix} \dot{\omega}_x \\ \dot{\omega}_y \\ \dot{\phi}_x \\ \dot{\phi}_y \\ \Delta \dot{V}_X \\ \Delta \dot{V}_Y \\ \Delta \dot{V}_Z \end{Bmatrix} \tag{B.10}$$

In this case, the cost function in Eq. (B.8) has no path cost (i.e. Lagrangian term). Substituting Eq. (B.5) into Eq. (B.9), the Hamiltonian is

$$\begin{aligned} H = &\lambda_1 \left(\frac{Fd}{I_x} - k\omega_y\omega_{z0} \right) + \lambda_2 k\omega_{z0}\omega_x + \lambda_3 \left(\omega_x + \omega_{z0}\phi_y \right) + \lambda_4 \left(\omega_y - \omega_{z0}\phi_x \right) \\ &+ \lambda_5 \frac{F}{m} \left(\phi_y \cos \omega_{z0}t + \phi_x \sin \omega_{z0}t \right) + \lambda_6 \frac{F}{m} \left(\phi_y \sin \omega_{z0} - \phi_x \cos \omega_{z0}t \right) \\ &+ \lambda_7 \frac{F}{m} \end{aligned} \tag{B.11}$$

B.4 Costate Equations

The costate equations are found by differentiating Eq. (B.11), the Hamiltonian, by

$$\dot{\lambda}_i = -\frac{\partial H}{\partial x_i} \tag{B.12}$$

Applying Eq. (B.12) to Eq. (B.11),

$$\dot{\lambda}_1 = \lambda_2 k \omega_{z0} - \lambda_3$$

$$\dot{\lambda}_2 = \lambda_1 k \omega_{z0} - \lambda_4$$

$$\dot{\lambda}_3 = \lambda_4 \omega_{z0} - \lambda_5 \frac{F}{m} \sin \omega_{z0} t + \lambda_6 \frac{F}{m} \cos \omega_{z0} t$$

$$\dot{\lambda}_4 = -\lambda_3 \omega_{z0} - \lambda_5 \frac{F}{m} \cos \omega_{z0} t - \lambda_6 \frac{F}{m} \sin \omega_{z0} t \tag{B.13}$$

$$\dot{\lambda}_5 = 0$$

$$\dot{\lambda}_6 = 0$$

$$\dot{\lambda}_7 = 0$$

From Eq. (B.13) λ_5, λ_6, and λ_7 are constants.

B.5   Transversality

The transversality condition is

$$H_f dt_f - \lambda^{\mathsf{T}} dx_f + dg = 0 \tag{B.14}$$

The final term in the transversality condition is

$$dg = \sum_{i=1}^{7} \frac{\partial g}{\partial x_{if}} dx_{if} + \frac{\partial g}{\partial t_f} dt_f \tag{B.15}$$

For this TPBVP, none of the final conditions are fixed. Substituting Eq. (B.11) into Eq. (B.14), the transversality condition is

$$
\begin{aligned}
0 =& [\lambda_{7f} \left(Fd/I_x - k\omega_{yf}\omega_{z0} \right) + \lambda_{2f} k\omega_{xf}\omega_{z0} + \lambda_{3f} \left(\omega_{xf} + \omega_{z0}\phi_{yf} \right) \\
&+ \lambda_{4f} \left(\omega_{yf} - \phi_{xf}\omega_{z0} \right) \lambda_{5f} \left(\phi_{xf} \cos \omega_{Z0} t + \phi_{xf} \sin \omega_{z0} t \right) F/m \\
&+ \lambda_{6f} \left(\phi_{xf} \sin \omega_{z0} t - \phi_{xf} \cos \omega_{z0} t \right) F/m + \lambda_{7f} F/m] dt_f \\
&- \lambda_{1f} d\omega_{xf} - \lambda_{2f} d\omega_{yf} - \lambda_{3f} d\phi_{xf} - \lambda_{4f} d\phi_{yf} - \lambda_{5f} d\Delta V_{Xf} \\
&- \lambda_{6f} d\Delta V_{Yf} - \lambda_{7f} d\Delta V_{Zf} \\
&+ \Delta V_{Xf} / \left(\Delta V_{Zf} \sqrt{\Delta V_{Xf}^2 + \Delta V_{Yf}^2} \right) d\Delta V_{Xf} \\
&+ \Delta V_{Yf} / \left(\Delta V_{Zf} \sqrt{\Delta V_{Xf}^2 + \Delta V_{Yf}^2} \right) d\Delta V_{Yf} \\
&- \sqrt{\Delta V_{Xf}^2 + \Delta V_{Yf}^2} / \Delta V_{Zf}^2 d\Delta V_{Zf}
\end{aligned}
\tag{B.16}
$$

Comparing similar terms in Eq. (B.16) provides

$$
\begin{aligned}
\lambda_{1f} &= \lambda_{2f} = \lambda_{3f} = \lambda_{4f} = 0 \\
\lambda_{5f} &= \Delta V_{Xf} / \left(\Delta V_{Zf} \sqrt{\Delta V_{Xf}^2 + \Delta \Delta_{Yf}^2} \right) \\
\lambda_{6f} &= \Delta V_{Yf} / \left(\Delta V_{Zf} \sqrt{\Delta V_{Xf}^2 + \Delta V_{Yf}^2} \right) \\
\lambda_{7f} &= - \sqrt{\Delta V_{Xf}^2 + \Delta V_{Yf}^2} / \Delta V_{Zf}^2 \\
0 &= F/m \lambda_{5f} \left(\phi_{yf} \cos \omega_{z0} t + \phi_{xf} \sin \omega_{z0} t \right) \\
&\quad + F/m \lambda_{6f} \left(\phi_{yf} \sin \omega_{z0} t - \phi_{xf} \cos \omega_{z0} t \right) + F/m \lambda_{7f}
\end{aligned}
\tag{B.17}
$$

For this TPBVP, sixteen boundary conditions are needed. Eight are given in Eq. (B.17) and the other eight boundary conditions are the assumed initial conditions

$$
\begin{aligned}
t(0) &= 0 \\
\omega_x(0) &= \omega_y(0) = 0 \\
\phi_x(0) &= \phi_y(0) = 0 \\
\Delta V_x(0) &= \Delta V_y(0) = \Delta V_z(0) = 0
\end{aligned}
\tag{B.18}
$$

B.6   Switching Function

The Hamiltonian in Eq. (B.11) is a switching function of the form

$$
H = H_0(x, \lambda, t) + H_1(x, \lambda, t) u
\tag{B.19}
$$

where u is the control, F, and H_1 is the switching function. From Eq. (B.11), the switching function is

$$
H_1 = \lambda_1 d/I_x + \lambda_7/m + \cos \omega_{z0} t \left(\lambda_5 \phi_y - \lambda_6 \phi_x \right) /m + \sin \omega_{z0} t \left(\lambda_5 \phi_x + \lambda_6 \phi_y \right) /m
\tag{B.20}
$$

When using the minimum principle, the control is

$$
F = \begin{cases} F_{max} & \text{if } H_1 < 0 \\ \text{undetermined} & \text{if } H_1 = 0 \\ -F_{max} & \text{if } H_1 > 0 \end{cases}
\tag{B.21}
$$

Since all of the states oscillate, it is unlikely that the switching function is zero for a long period of time. Then the force will either be negative or positive maximum. Burning at positive F_{max} results in very large pointing errors and is the thrust profile that is being improved. Having a negative force makes little sense.

Instead fix the force at the beginning and the end and assume that the control is not bounded. Realistically, the force is bounded to be above zero and below the maximum force, but to continue the implicit optimization, a control law is necessary. If a parameter optimization is used instead, these bounds could be utilized.

B.7 Control Law

To find the control law, differentiate the switching function with respect to time until the control appears which takes two derivatives in this case. The second time derivative is

$$\frac{d^2}{dt^2}(H_1) = \frac{\partial}{\partial t}\left(\frac{dH_1}{dt}\right) + \frac{\partial}{\partial x}\left(\frac{dH_1}{dt}\right)\dot{x} + \frac{\partial}{\partial \lambda}\left(\frac{dH_1}{dt}\right)\dot{\lambda} + \frac{\partial}{\partial u}\left(\frac{dH_1}{dt}\right)\dot{u} = 0 \quad \text{(B.22)}$$

where

$$\frac{dH_1}{dt} = \frac{\partial H_1}{\partial t} + \frac{\partial H_1}{\partial x}\dot{x} + \frac{\partial H_1}{\partial \lambda}\dot{\lambda} + \frac{\partial H_1}{\partial u}\dot{u} \quad \text{(B.23)}$$

Substituting the switching function into Eq. (B.22), the second time derivative of the switching function is

$$\begin{aligned}
\frac{d^2}{dt^2}(H_1) = & - d\omega_{z0}\left(\lambda_4 - k\lambda_4 + k^2\lambda_1\omega_{z0}\right)/I_x \\
& + I_z\omega_{z0}\cos\omega_{z0}t\left(\omega_x\lambda_5 + \omega_y\lambda_6\right)/\left(I_xm\right) \\
& + I_z\omega_{z0}\sin\omega_{z0}t\left(\omega_x\lambda_6 - \omega_y\lambda_5\right)/\left(I_xm\right) \\
& - 2dF\lambda_6\cos\omega_{z0}t/\left(I_xm\right) + 2dF\lambda_5\sin\omega_{z0}t/\left(I_xm\right)
\end{aligned} \quad \text{(B.24)}$$

By setting Eq. (B.24) to zero and solving for the force, the control law is (from the Kelley condition [88])

$$\begin{aligned}
F = & \frac{I_z\omega_{z0}\left[\left(\omega_x\lambda_5 + \omega_y\lambda_6\right)\cos\omega_{z0}t + \left(\omega_x\lambda_6 - \omega_y\lambda_5\right)\sin\omega_{z0}t\right]}{2d\left(\lambda_6\cos\omega_{z0}t - \lambda_5\sin\omega_{z0}t\right)} \\
& + \frac{m\omega_{z0}\left(\lambda_4 - k\lambda_4 + k^2\lambda_1\omega_{z0}\right)}{2\left(\lambda_6\cos\omega_{z0}t - \lambda_5\sin\omega_{z0}t\right)}
\end{aligned} \quad \text{(B.25)}$$

B.8 Implementation in MATLAB

The MATLAB® TPBVP optimizer, tpb4c, is used to solve the TPBVP. Since the ending time is not fixed, an integration time of one is used and a dummy variable, r, is incorporated into the differential equations where

$$\dot{r} = 0 \tag{B.26}$$

To implement the integral constraint of the total impulse, the total impulse is also used as a state where

$$\dot{\mathfrak{J}} = F \tag{B.27}$$

Now there are 16 states to integrate and only 16 boundary conditions, but when implementing in MATLAB, only one more boundary conditions is needed. The total impulse provides the final boundary condition with

$$\mathfrak{J}(t_f) = \mathfrak{J}_r \tag{B.28}$$

where $\mathfrak{J}_r$ is found in Eq. (3.17).

For better convergence, some of the equations were scaled. Most of the states stay relatively small except for the total impulse and the Z-velocity. Then the total impulse is scaled by $\mathfrak{J}_r$, the Z-velocity is scaled by V the $\Delta V_Z f$ guess, and the time (now τ) is scaled by r. After re-deriving the costate equations and control law, the TPBVP becomes

$$\text{Minimize} J = \frac{\sqrt{\Delta V_{Xf}^2 + \Delta V_{Yf}^2} V}{\Delta V_{Zf}} \tag{B.29}$$

subject to

$$\omega_x' = Fdr/I_x - k\omega_y\omega_{z0}r$$

$$\omega_y' = k\omega_{z0}\omega_x r$$

$$\phi_x' = \omega_x r + \phi_y\omega_{z0}r$$

$$\phi_y' = \omega_y r - \phi_x\omega_{z0}r$$

$$\Delta V_X' = \frac{Fr}{m}(\phi_y \cos\omega_{z0}r\tau + \phi_x \sin\omega_{z0}r\tau)$$

$$\Delta V_Y' = \frac{Fr}{m}(\phi_y \sin\omega_{z0}r\tau - \phi_x \cos\omega_{z0}r\tau)$$

$$\Delta V_Z' = \frac{Fr}{mV}$$

(B.30)

$$\lambda_1' = \lambda_2 k\omega_{z0}r - \lambda_3 r$$

$$\lambda_2' = \lambda_1 k\omega_{z0}r - \lambda_4 r$$

$$\lambda_3' = \lambda_4\omega_{z0}r - \lambda_5 r\frac{Fr}{m}\sin\omega_{z0}r\tau + \lambda_6\frac{Fr}{m}\cos\omega_{z0}r\tau$$

$$\lambda_4' = -\lambda_3\omega_{z0}r - \lambda_5\frac{Fr}{m}\cos\omega_{z0}r\tau - \lambda_6\frac{Fr}{m}\sin\omega_{z0}r\tau$$

$$\lambda_5' = 0$$

$$\lambda_6' = 0$$

(B.31)

$$\lambda_7' = 0$$

$$r' = 0$$

$$\mathfrak{J}' = \frac{Fr}{\mathfrak{J}_r}$$

The control law was used to define the force at each step, and the force was defined to be zero at the beginning and F_{max} at the end.

For an initial guess, the heuristic profiles are used to find the minimum velocity pointing error at the end of Phase 1. The best profile is an exponential profile with a ramp-up time of 11.141 seconds. This guess provides an initial guess for r and V but does not provide an initial guess for any of the costates. The last three costates are constant, and the transversality condition gives guesses for these three states. Using the control law, the initial guess for λ_4 can be found from λ_1. Now only three initial

guesses are needed. A grid search was performed by searching from -10 to 10 by 0.05 (a total of 64 million guesses) over the first three costates but none of these guesses produced converged solutions.

The next approach was to input a different guess into each time step. The same exponential force profile was used to find guesses for the costates by simply propagating the costate differential equations. By changing the initial propagation points from -10 to 10, the costates initially varied, but by the end of Phase 1, they converged. Then using 0 for the first three costates, the exponential force profile was used to find the initial guess for the TPBVP at each time step. The solution did converge, but the force varied from $\pm 4 \times 10^{12}$ which is not a valid solution.

Clearly the TPBVP is not finding the correct force profile. The main problem is that the control (i.e. the force) should be bounded, but in order to use a control law, the force is left to be unbounded. Even when defining the total impulse as the integral of the absolute value of the force, the force varies from $\pm 8 \times 10^8$ which is still not a valid solution. Since the optimization problem is to minimize the velocity pointing error at the end of Phase 2, this implicit optimization approach is relinquished in favor of a parameter optimization.

VITA

VITA

Kaela Martin (nee Rasmussen) was born in 1988, the youngest child of Marilyn and Peter Rasmussen. She graduated summa cum laude from Iowa State University in 2010 with a B.S. in Aerospace Engineering and a B.S. in Mathematics. In December of 2011, Kaela received her Master's in Aeronautical and Astronautical Engineering from Purdue University under the direction of Professor James Longuski. She married Matt Martin in May of 2012. During her graduate studies, Kaela was supported by a National Science Foundation Graduate Research Fellowship and a Purdue Doctoral Fellowship. In her spare time, Kaela enjoys spending time outside whether it is playing ultimate Frisbee, rock climbing, or backpacking in the wilderness.